Theses and Dissertations

Graduate School

2022

Improving the Early Detection of Cardiovascular Toxicity Secondary to Radiotherapy for Lung Cancer via Patient-specific Quantitative Magnetic Resonance Imaging

Alireza Omidi

Virginia Commonwealth University

IMPROVING THE EARLY DETECTION OF CARDIOVASCULAR TOXICITY SECONDARY TO RADIOTHERAPY FOR LUNG CANCER VIA PATIENT-SPECIFIC QUANTITATIVE MAGNETIC RESONANCE IMAGING

A thesis submitted in partial fulfillment of the requirements for the degree of Doctor of Philosophy at Virginia Commonwealth University.

By

ALIREZA OMIDI

MSc. Mechanical Engineering, University of Tehran, 2018

Director: John S. Wilson, M.D., Ph.D.

Assistant Professor, Department of Biomedical Engineering and Pauley Heart Center

Virginia Commonwealth University

Richmond, Virginia

August, 2022

2

ACKNOWLEDGMENT

First, I would like to thank you my caring family for being a constant source of support for me even from thousands of miles away. It has never been easy not being able to seeing you for years but hoping that I am doing the best I can to make you proud and to see the smile on your faces when I meet you again. I miss you and love you more than anything in this world!

In the academic side, I'd like to thank you my primary advisor, Dr. John S. Wilson. It was an absolute pleasure for me to work with such a knowledgeable, helpful, supportive mentor like you in the past three years. I just wanted to take this time to say thank you for everything that you have done for me. You are an incredible advisor and an incredible listener. Your efforts have never gone unappreciated and you have helped me out more than you know. If it wasn't for you, I could never have gotten involved with all these amazing projects and know all these great people in the field.

Next, I would like to Thank you Dr. Mihaela Rosu-Bubulac, I'm pretty sure you already know that you're fantastic, but in case you didn't, I'm telling you now. A wonderful advisor with such a great personality that I cannot describe with words. If I am being honest, you were not just an advisor, you were more like a family to me. No one, not even my friends, would call me late at night to listen to my concerns and help me throughout the ups and downs. It is people like you that continue to inspire students like me each and every day. Thank you for being the best.

Next, I would like to Thank you Dr. Elisabeth Weiss. I'm more than grateful for getting to know one of the best oncologist professors in the field who puts all the efforts she can to make sure everything is being done in the best manner possible. You have directed, guided and encouraged me through a wonderful experience here at VCU. Thank you for being easy to speak with and always available to give guidance.

Next, I would like to Thank you Dr. Jennifer Jordan who has always been my huge help in the past years. I really think without all your help I would not be where I am today. Every time I have a question or need perspective, you've been there to help me learn and understand all the data analysis that I need. Every student in the BME department is fortunate to have someone like you to guide us through our imaging analysis problems. I also had the opportunity of working as your TA for one semester. I don't know if I was a decent TA or not but you were absolutely a wonderful instructor. Thanks for everything.

Next, I would like to Thank you Dr. Carrie Peterson. Even though, you were not directly involved in my projects I had the honor of working with you as your TA for four semesters. I cannot describe how much I enjoyed your class and how honored I am for trusting me for two years of handling your course materials to me. BME students are lucky to have the best statics course instructor they could ask for. Thank you for everything.

Last but not least, I would like to thank you the MRI technicians, Kevin and Chris, MRI suite nurses, Sarah, research coordinator, Laura, and most importantly our volunteered patients who agreed to participate in this IRB approved study. Thank you all!

Alireza

TABLE OF CONTENTS

LIST OF TABLES

LIST OF FIGURES

LIST OF ABBREVIATIONS

AAPM	American association of physicists in medicine
AHA	American heart association
AIP	Average intensity projection
AP	Anterior to posterior
CMR	Cardiac magnetic resonance
CT	Computed tomography
CVD	Cardiovascular disease
CVT	Cardiovascular toxicity
DENSE	Displacement encoding with stimulated echoes
DIBH	Deep inspiration breath hold
DIR	Deformable image registration
DNA	Deoxyribonucleic acid
DVH	Dose volume histogram
ECV	Extracellular volume
ETL	Echo train length
FOV	Field of view
GCS	Global circumferential strain
GLS	Global longitudinal strain
GRE	Gradient echo
GRS	Global radial strain
GTV	Gross tumor volume
Gy	Gray
iGTV	Internal gross target volume
IL	Interleukin
IRB	Institutional review board
ITV	Internal target volume
LGE	Late gadolinium enhancement
LV	Left ventricle
LVEF	Left ventricle ejection fraction
LVM	Left ventricle myocardium
mATA	Mid ascending thoracic aorta
MDA	Mean distance to agreement
mDTA	Mid descending thoracic aorta
MOLLI	Modified Look-Locker inversion recovery
MRI	Magnetic resonance imaging
PSIR	Phase sensitive inversion recovery
PTV	Planning target volume
PWV	Pulse wave velocity
RIR	Rigid image registration
RL	Right to left
ROI	Region of interest
ROS	Reactive oxidative stress
RT	Radiotherapy
SCMR	Society of cardiac magnetic resonance imaging
SD	Standard deviation

SI	Superior to inferior
SSFP	Steady-state free precession
T1-VIBE	T1-Volumetric interpolated breath-hold examination
TE	Echo time
TNF	Tumor necrosis factor
TR	Repetition time
VCU	Virginia Commonwealth University
VMAT	Volumetric modulated arc therapy
WSS	Wall shear stress

ABSTRACT

IMPROVING THE EARLY DETECTION OF CARDIOVASCULAR TOXICITY
SECONDARY TO RADIOTHERAPY FOR LUNG CANCER VIA PATIENT-SPECIFIC
QUANTITATIVE MAGNETIC RESONANCE IMAGING

By

ALIREZA OMIDI, MSc.

A thesis was submitted in partial fulfillment of the requirements for the degree of Doctor of
Philosophy at Virginia Commonwealth University.

Virginia Commonwealth University, 2022.

Major Director: John S. Wilson, M.D., Ph.D.

Assistant Professor, Department of Biomedical Engineering and Pauley Heart Center

Introduction: Radiotherapy (RT) can damage the cardiovascular system regionally and globally. Serial assessment of cardiac and aortic function before and after radiotherapy using novel MRI sequences may identify subclinical early and focal changes before global, and potentially irreversible, damage occurs.

Purpose: To measure non-invasively the spatiotemporal evolution of global and regional cardiac and aortic function before and after RT, investigate the correlation between changes in cardiac and aortic metrics over different follow-ups, evaluate the correlation of cardiac and aortic function with local radiation dose, and investigate the variation in regional quantitative dose due to respiratory and cardiac motion of the left ventricle (LV), left ventricular myocardium (LVM) and across segments of the American Heart Association (AHA) model.

Methods and materials: Eight patients with lung cancer who were scheduled to receive RT with at least 5 Gy of radiation to 10% of the volume of the heart were recruited for this project. Each

patient underwent one 4D-CT scan for treatment planning purposes. MRI evaluation included cine gradient echo (GRE), T1/T2 mapping, cardiac displacement encoding with stimulated echoes (DENSE), late gadolinium enhancement (LGE), and 4D-flow sequences at three time points: baseline (a few days before RT), 3-months post-RT completion, and 6-months post-RT completion. For cardiac evaluation, left ventricle ejection fraction (LVEF) was measured globally while radial/circumferential/longitudinal/ strain, T1/T2 signal, extracellular volume (ECV), and enhanced volume were calculated both regionally (i.e., AHA model) and globally. For aortic evaluation, circumferential strain at mid-ascending/descending aorta and longitudinal strain at ascending aorta were measured globally and WSS at mid-ascending/descending aorta was calculated regionally and globally. LVEF, strain, T1/T2 signal, ECV, and LGE calculations were done using cvi42 software (Version 5.10.1, Circle Cardiovascular Imaging; Calgary, Canada). Strain from DENSE MRI was calculated using a custom MATLAB code and wall shear stress (WSS) was measured using CAAS software (Pie Medical Imaging). Absolute changes of each metric were calculated from subtraction of follow-up values from baseline measurements. Relative changes were calculated from (follow-up value-baseline value)/(baseline value)*100.

To find the correlation between the MRI-based measurements and RT dose, the dosimetry map from the average intensity projection (AIP) (i.e., the average pixel intensities across all the 4D-CT breathing phases) dataset was mapped onto T1-Volumetric interpolated breath-hold examination (VIBE) following image registration (rigid or deformable depending on the degree of deformations) and from there onto other 2D-MR sequences. Maximum and mean radiation dose were calculated on segmented regions following quantification of the dose volume histogram (DVH). Image registration was also used to assess the effects of respiratory motion and cardiac motion on the dose delivered to the LV, LVM and segments of AHA model and to estimate the

cumulative dose over the cardiac cycle. In short, AIP was used to transfer the dose to all 4D-CT breathing phases, T1-VIBE was used to map the dose from CT to MRI, and an average intensity cine MRI (i.e., the average pixel intensities across all the cardiac phases of the cine MRI dataset at expiration) was utilized to move the dose over cardiac phases. The cumulative dose over cardiac phases was also accumulated using deformable image registration. To better compare the doses between various modalities, patients, and processing techniques, all dose values were reported as doses relative to the AIP dose; that is, the relative maximum and mean dose were calculated as ((maximum dose – maximum AIP dose)/(maximum AIP dose))*100 and ((mean dose – mean AIP dose)/(mean AIP dose))*100, respectively.

Results: In evaluation of LV dose variation due to cardiopulmonary motion, a significant increase of mean dose to the LV was noted at expiration for patients with tumors in the upper lobe of the lung (16.5%, P<0.0145). No significant changes were noted in maximum LV dose during respiration (P>0.78) or cardiac motion at breath-hold (P>0.074). During expiration at breath-hold, the highest LV/LVM mean dose occurred during diastolic cardiac phases (25.1%, P=0.037) with significantly higher dose values over anterior regions of the AHA model, where it is closest to the primary tumor (231%, P=0.0117).

In spatiotemporal evaluation of cardiac function, no significant differences were noted in global measurements at 3-months or 6-months post-RT treatment compared to baseline (P>0.06) except for global T2 signal at 3-months post-RT (P=0.048) and enhanced volume from LGE MRI at 6-months follow-up (P=0.0356). All segmental evaluations demonstrated significant changes at 3-months and/or 6-months compared to baseline except for ECV (P>0.33). Regional T1 signal increased in segments 2 (2.2%, P=0.038) and 6 (5.1%, P=0.048) at 3-months post-RT, T2 signal increased in segments 1, 4-7, 12, and 14 at 3-months follow up (P<0.048). Radial strain decreased

in segment 2 at 3-months (-23%, P=0.0176) and segments 1 (-25.5%, P=0.023) and 12 (-32.8%, P=0.035) at 6-months; circumferential strain decreased in segments 2-3 at 3-months (-41.4%, P=0.0156 and -71% P=0.047) and segments 1 and 12 at 6-months (-13.4% P=0.04, -15.5% P=0.0123). Longitudinal strain decreased in segment 9 (-62.4% P=0.0313) and increased in segment 8 at 3-months (31.7% P=0.0313), but decreased in segments 2-3, 9 at 6-months (P<0.047). Late gadolinium-enhanced volume increased in segments 1, 3, and 8 at 3-months (P<0.037) and in segments 1 and 3 at 6-months post-RT completion (P<0.047). Regional strain values did not demonstrate dose-dependent responses at 3- or 6-months follow-up (P>0.063). However, radiobiological measurements, namely regional T1/T2 signal and LGE, demonstrated significant dependence on local quantitative dose. Specifically, T1 signal was significantly higher at regions receiving greater than 50 Gy compared to 0-10 Gy at 3-months (P=0.0219) and all other dose ranges at 6-months (P<0.0142). For T2 signal, significant changes were noted between areas with doses >50 Gy and 0-10 or 10-20 Gy (P<0.0001) and between 40-50 Gy and 10-20 Gy (P=0.0089) at 6-months post-RT. No significant differences were found at 3-months (P=0.7507). Similar results were found for enhanced areas, except that significant differences at 6-months were between >50 Gy regions and both 0-10 and 20-30 Gy (P<0.033). In addition, linear dose-response was noted between T1/T2 signal and dose at both follow-up (T1: P<0.0251, T2: P<0.0081) and between enhanced area and dose at 6-months follow-up (P=0.001). Finally, correlation between different metrics demonstrated a strong correlation between T1 and T2 changes at 6-months post-RT (both P<0.0001).

In spatiotemporal evaluation of aortic function, no significant changes were noted in global circumferential strain at mid-ascending/descending aorta, global longitudinal strain at ascending aorta, and global or regional WSS at mid-ascending/descending aorta at 3-months and 6-months

follow up (P>0.06). No correlation was found between the RT dose and aortic metrics at 3-months and 6-months follow up. Also, no correlation was noted between global aortic metrics at ascending aorta (i.e., circumferential/longitudinal strain and WSS) and global cardiac metrics (T1, T2, radial/circumferential/longitudinal strain, and LGE) at the same or different follow-up points. However, the dose on the ascending aorta was significantly correlated with radial/circumferential strain at segment 2 of AHA model (i.e., basal anteroseptal) at 6-months post-RT (radial strain and dose: P=0.0169, circumferential strain and dose: P=0.0206).

Conclusion: For lung cancer patients with radiation to the upper lobe of the lung, the LV received the lowest dose during inspiration. During expiratory breath-hold, the minimum radiation dose to the LV and LVM occurred during cardiac systole. MRI-derived segmental evaluation of dose demonstrated significantly higher doses in regions in closer proximity to the tumor location compared to the single estimated global LV dose derived from the corresponding breathing phase from the 4D-CT dataset. This finding emphasizes the importance of regional dose quantification for assessment of early focal RT-induced cardiovascular toxicity. Finally, the results suggest that delivery of RT during inspiration and systole may minimize the radiation dose to the LV.

Classic global cardiac and aortic measurements were unable to detect early damages to the cardiovascular system. Regional cardiac metrics demonstrated significant differences at 3-months and/or 6-months follow-up with a dose-dependent response in radiobiological MRI-based metrics (e.g., T1/T2 signal and enhanced volume from LGE). Regions with >50 Gy radiation demonstrated significant changes in biological tissue characterization parameters compared to lower dose regions (e.g., 0-10 Gy). Correlation of T1 and T2 signal at 6-months may imply that the increase of myocardial fibrosis/inflammation might increase the probability of myocardial edema at 6-months following RT completion. Finally, significant correlation between the segmental cardiac

radial/circumferential strain and aortic dose implies that the RT-induced aortic damages to the ascending aorta may indirectly impact the kinematics of the myocardium at regions where the aorta and LV are in mechanical continuity.

1 Introduction

Cardiovascular disease (CVD) and cancer are two of the most significant causes of death worldwide [1] which roughly take 17.9 million and 9.6 million lives each year, respectively [2], [3]. Even though improvements in cancer treatment have increased the cancer survival rates in the past years, the side-effects of cancer-therapies (e.g., radiotherapy, chemotherapy) remain an issue [4]. In radiotherapy (RT) (i.e., eliminating cells with ionized radiation), exposure of healthy tissue to radiation may lead to damage. When this damage involves the cardiovascular system, it is referred to as cardiovascular toxicity (CVT) [4], [5]. It has been shown that up to a third of patients with lung cancer who undergo RT develop cardiac complications afterward, [6] including arrhythmias, heart failure, vulvar dysfunction, and coronary artery disease [5]. Thus, even though RT is necessary to increase primary survival rates following a cancer diagnosis, unintended CVT may secondarily increase the risk of morbidity and mortality due to pre-mature cardiovascular disease [7]. While radiation oncologists strive to minimize the radiation dose to the heart, incidental exposure cannot always be avoided depending on the location of the primary (and potentially other metastatic) lesions. Moreover, management of dose variations to the tumor and the heart due to intrafraction motions (i.e., movement of internal organs due to respiratory and cardiac motion) requires more sophisticated high-resolution techniques to capture the cardiopulmonary motion and account for the actual dose delivered to the tumor and organs at risk [8], [9]. Besides evaluation of radiation exposure to the heart, consequences of radiation exposure to the aorta have received little attention, despite the fact that aortic stiffness can directly affect cardiac function. Hence, it is crucial to investigate the quantitative spatial and temporal relationships between RT and CVT in order to identify early signs of aortic and cardiac damage, to evaluate any correlations between aortic and cardiac toxicity, to appropriately account for

cardiac/respiratory motions when calculating regional radiation dose, and ultimately to optimize patient-specific therapeutic planning and follow-up.

Various imaging modalities are available to monitor cardiovascular dysfunction in the clinic. Echocardiography, as one of the most widely available and generally affordable modalities, can be used to measure the global strain, left ventricular ejection fraction (LVEF), and valvular function [10]; however, its limited acoustic window and poor temporal resolution limit the use of echocardiography for serial assessment of the cardiovascular system, even with advancements in 3D echocardiography and enhanced echo using microbubbles as contrast agents [11]. A more reproducible imaging modality is nuclear scanning, which offers gated-sequences but suffers from poor assessment of valvular morphologies [12] and requires radioactivity, making it less desirable for longitudinal evaluation of CVT. A more widely used imaging modality is computed tomography (CT), which is the gold standard for assessing anatomy [10]. Major advantages of CT are its high spatial resolution and short exam time. Coronary artery assessments and calcified tissue measurements are some of the particular use of cardiac CT in quantification of RT-induced CVT [13]. Unfortunately, the required ionized radiation during CT imaging is a drawback for serial follow-up.

Finally, cardiac magnetic resonance (CMR) imaging, as a non-invasive imaging modality, provides some benefits over the other imaging modalities. For instance, CMR is known as the gold standard for assessment of LV function [12]. Unlike echocardiography, MRI offers great reproducibility and accuracy for longitudinal follow-up studies. In addition, MRI does not require ionizing radiation to produce functional/structural images, unlike CT and nuclear scanning. Even though the primary use of CMR has focused on global evaluation of cardiovascular system (e.g., LVEF and global strain measurements), novel MR sequences (e.g., T1/T2 mapping and late

gadolinium enhancement (LGE)) can evaluate subclinical changes over focal regions with high spatial resolution and excellent tissue contrast [14], [15].

Despite the advantages of regional myocardial assessments via CMR, many of these advanced sequences are still not widely used in clinical settings. In fact, current clinical assessment of myocardial function primarily consists of global metrics such as LVEF, ventricular volumes, and more recently, global circumferential strain (GCS) and global longitudinal strain (GLS). Similarly, current clinical evaluation of aortic health/stiffness is frequently limited to homogenized metrics of aortic stiffness (e.g., via pulse wave velocity (PWV) or circumferential distensibility), which cannot distinguish potential heterogeneities around the circumference of the aorta. As a result, focal and/or subclinical cardiovascular damage (as may be expected by RT) may not acutely affect global metrics due to the ability of the heart to compensate to maintain global function. Similarly, regional aortic vulnerabilities could be missed by global or homogenized metrics of aortic function. In addition to missing potentially heterogeneous changes in the regional kinematics of the soft tissues of the heart and aorta, standard imaging techniques often fail to assess the regional composition of the myocardium or the local flow-induced shear stresses acting on the endothelium of the aortic wall, which are key mechanobiological factors influencing the current and future biomechanical states of the heart and aorta. Thus, there's a critical need to provide a comprehensive regional assessment of cardiovascular biomechanics noninvasively. Recent advancements in quantitative cardiovascular MRI, namely cine MRI, T1/T2 mapping, Displacement Encoding with Stimulated Echoes (DENSE), LGE MRI, and 4D-Flow now offer the potential to meet this need in a single integrated MRI study.

In addition to regional biomechanical assessments of the heart and aorta via novel MRI sequences, registration of quantitative patient-specific radiation dosimetry maps to the regional MRI-derived

metrics could help identify clinically relevant correlations between RT and CVT. Successful development of such an assessment and its application to RT-induced CVT could improve the ability to quantify, predict, and identify CVT at its earliest stages. Unfortunately, accurate and reliable image registration across imaging modalities of clinical dosimetry maps derived from CT planning onto axial, short-axis, and long-axis MR images for advanced assessments of CVT is challenging and prone to errors. Therefore, a reliable and accurate image registration algorithm and workflow must be developed and evaluated to make sure it complies with the American Association of Physicists in Medicine (AAPM) guidelines [16], [17].

Image registration is also important in the evaluation of the variation in radiation dose received by tissues (e.g., heart and its substructures) during cardiopulmonary motion. To elaborate, the RT treatment planning is a non-gated sequence while the internal organs (e.g., heart and its substructures) and the tumor move due to respiratory and cardiac motion continuously; therefore, tissues may actually receive a radiation dose different from what was planned. That is, the clinical dosimetry map is planned and effectively fixed in space using an 'average' position of the heart, lungs, great vessels, and tumor, even though each may be in continuous motion through this fixed radiation field. The difference in actual dose versus estimated dose could be even more significant when the dose is evaluated at regional levels (e.g., American Heart Association (AHA) model, Figure 1.1) rather than globally. To account for the cardiopulmonary motion-induced variation in dose on tissues of interest (e.g., LV), image registration with respiratory- and cardiac-gated sequences with high spatiotemporal resolutions are required to track the cardiopulmonary movement and transfer/transform the dosimetry map from the planning CT onto images at various respiratory phases and cardiac phases and then calculate a cumulative dose over the cardiac cycle via a robust workflow using deformable image registration (DIR).
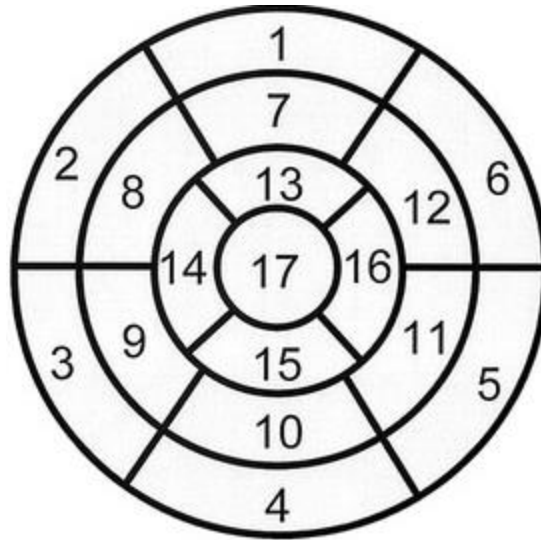
Figure1.1 American Heart Association (AHA) model with corresponding anatomical reference as: segment1: basal anterior, segment2: basal anteroseptal, segment3: basal inferoseptal, segment4: basal inferior, segment5: basal inferolateral, segment6: basal anterolateral, segment7: mid anterior, segment8: mid anteroseptal, segment9: mid inferoseptal, segment10: mid inferior, segment11: mid inferolateral, segment12: mid anterolateral, segment13: apical anterior, segment14: apical septal, segment15: apical inferior, segment16: apical lateral, segment17: apex.

The next few sections will focus on the physiology of radiotherapy-induced cardiotoxicity, and detail some of the novel MR sequences that were used in this study along with descriptions of the algorithms for image registration and the quantification of relevant biomechanical metrics.

1.1. Pathophysiology

Ionized radiation can kill cells via direct (e.g., deoxyribonucleic acid (DNA) double strand break) or indirect (e.g., free radical-induced DNA damage) mechanisms. The type and the degree of damage can be different in various tissues based on extracellular pattern and structure. In the cardiovascular system, RT-induced myocardial injury results from multiple mechanisms that lead to structural and functional damage. RT-induced CVT is associated with the effects of cytokines (e.g., interleukin (IL)-1, IL-6, tumor necrosis factor (TNF)-α)), which are generated by the oxidative stress and the inflammatory response [18], [19]. In addition, a high concentration of free radicals is shown to damage cells through dysregulation of the functions of cardiomyocytes and

24

endothelial cells. Notably, reactive oxidative stress (ROS) has also been shown to significantly affect mitochondrial function and hence cardiac function [19]. In addition, apoptosis and necrosis due to calcium release can be impacted by ROS [19].

RT-induced microvascular and macrovascular damage are a main source for myocardial toxicity and the proinflammatory response [20]. Collagen production, as a result of promotion of smooth muscle cells into myofibroblast, is increased via cytokines and inflammatory cells. In addition, the risk of myocytes injury is increased after RT due to narrowing of capillaries via endothelial injury. Finally, injured myocytes are often replaced by collagenous fibrotic tissue, which leads to increased stiffness of the myocardium, reduction in contractibility, and hence dysregulation of cardiac contraction and function [7], [20], [21].

Some of the most common cardiac complications due to RT are coronary artery disease, pericarditis, cardiomyopathy, arrhythmias, and valvular dysfunction [22], [23]. A few of these complications occur six months post RT (e.g., acute restrictive pericarditis) [24] but the majority of cardiac issues don't manifest themselves until years after RT completion [25]. For instance, LV dysfunction, on average, has been shown to occur 23 years following RT in 22% of the patients with chest irradiation [26]. Similarly, the development of valvular heart diseases has been shown to increase proportional to radiation dose 30 years post-irradiation [27].

Finally, the normal tissue complication probability (NTCP) method (i.e., a model that uses the irradiated volume and the amount of absorbed radiation dose to quantify dosing) has shown that RT-induced cardiac mortality for a dose of 25 Gy to less than 10% of the volume of the heart is 1-2% at 15 years post-RT [1].

In addition to the length of time since RT, several other risk factors have been shown to increase the risk of developing RT-induced CVT [1]. First, pre-existing cardiovascular disease and known cardiovascular risk factors increase CVT risk [28]. Examples include pre-existing coronary artery disease, chronic obstructive pulmonary disease, ischemic heart disease, diabetes, smoking, hypercholesterolemia, and valvular disease [21]. For instance, pre-existing ischemic heart disease in breast cancer patients has been recognized as a higher risk hazard in radiation-related heart disease compared to patients without prior ischemic heart disease diagnosis (1.58 versus 1.08) [29]. The multivariable Cox regression analysis of hypercholesterolemia, smoking, and diabetes mellitus as risk factors in Hodgkin lymphoma (HL) survivors demonstrated an increased ratio of myocardial infraction, angina pectoris, congestive heart failure, and valvular disorders occurrence (1.45 to 4.55) following cancer therapy [30].

Second, evidence suggests that certain demographics may be at higher risk, including a young age at the time of RT, sex, and race/ethnicity. Younger HL patients (<20-year-old) have been shown to be more prone to myocardial infarction, congestive heart failure, and angina pectoris following chemoradiotherapy. This can be partly explained by higher vulnerability of the immature cardiovascular tissue to chemoradiotherapy along with low background incidence rate of cardiovascular complications at younger age [30]. Women have shown a higher chance of radiotherapy-induced cardiovascular events [31], [32] mostly due to lack of cardiovascular protective effect of estrogen as the majority of the women participants were postmenopausal [20]. Finally, black survivors of breast cancer have been shown to be at higher risk of cardiotoxicity compared to white people from the same cohort of patients [33].

Third, the risk of CVT is also linked to radiation dose and technique. Higher radiation doses (to both whole structures like the heart and individual substructures like the LV) and higher doses per

fraction have both been linked to increased risk of CVT. Although complications can be seen at any dose range, in childhood cancer survivors, cardiac exposure radiation of ≥1500 cGy significantly increased the risk of pericardial disease, heart failure, valvar abnormalities, and myocardial infraction by 2-6 fold compared to non-irradiated ones [34]. In HL survivors, the radiation dose increase above 30 Gy and 40 Gy demonstrated a significant increase of valvular heart disease rate by 1.4 and 11.8, respectively, with major effects on the aortic valve and mitral valve [27]. It has been shown that the probability of coronary artery disease increases by 7.4% per gray among breast cancer patients (regardless of cardiac risk factors) with no apparent threshold [31]. In addition, the type of radiation delivery techniques (e.g., conformal RT, patient positioning, breath-holding) may directly affect CVT risk by attempting to minimize radiation to key structures [23]. The improved radiation techniques over time have shown a reduction in ischemic heart disease occurrence in left-sided breast cancer patients following RT from 13.1% in 1973-1979 to 5.8% in 1985-1989 [35].

Finally, the presence of concurrent treatments (e.g., chemotherapy and/or immunotherapy) may also affect the risk of CVT both as an independent additive effect and potentially compounding the effect of RT-induced damage. For instance, in the case of HL survivors, combination of mediastinal RT with anthracycline chemotherapy increases the risk of congestive heart failure and valvular disorders by 2.8- and 2.1-fold, respectively, compared to the RT treatment alone [30]. These combined therapeutic regimens can make it difficult to distinguish individual effects of highly localized RT in the presence of underlying global dysfunction due to systemic therapies without careful evaluation of spatial correlations of quantitative metrics of cardiovascular function and focal radiation dose.

1.2. MR imaging

Cine MRI: cine images (gradient echo (GRE) or steady state free precession (SSFP)) are cardiac-gated sequences, usually at breath-hold, which capture the movement of organs over the cardiac cycle. Cine images are mostly used to evaluate LV volumes (e.g., end systolic, end diastolic, and stroke volumes), LVEF (i.e., the difference between the end-diastolic and end-systolic volumes (i.e., stroke volume) divided by the end diastolic volume), regional and global longitudinal/circumferential/radial strain of the myocardium via tissue-tracking algorithms and global circumferential strain measurement of the aorta over various cross-sections. Regional aortic strain measurements are not possible via tissue tracking due to limited wall thickness of the aortic wall.

The normal range of LVEF has been reported to be approximately 50% to 70% in healthy individuals [36], and a reduction of EF below 50% has been defined as an indication of cardiotoxicity [37]. The pooled mean values of global longitudinal, radial, and circumferential strain measurements among healthy subjects have been reported as -18.6% (-17.6 − -19.5%), 38.7% (30.5 − 46.9%), and -21.0% (-19.6 − -22.4%), respectively [38].

Cardiac DENSE MRI: DENSE is a novel non-invasive method primarily developed for mapping regional cardiac deformation [39]. DENSE MRI can be used to quantify regional heterogeneities in strain around the myocardium at each imaged cross-section by directly encoding the displacement of each voxel into its phase [39], [40]. Compared to prior MRI-based strain mapping techniques like tagged MRI, DENSE MRI allows higher resolution strain measurements [40]. It should be noted that strain measurement is vendor and technique dependent. For instance, it has been shown that the regional LV circumferential strain value range between DENSE and tissue tracking were -13±4% and -10±3% to -16±6%, respectively with the best matching seen on the

tissue tracking measured with Circle Cardiovascular Imaging (-14±4%). Higher variability and poor agreement between strain measurements were mostly noticeable in radial and longitudinal strain. LV regional radial strain in DENSE and tissue tracking ranged between 40±28% and 23±9% to 47±26%, respectively. In longitudinal strain measurement the strain value ranged between -8±3% and -11±3% to -13±5% for DENSE and tissue tracking, respectively [41]. The tissue tracking range is obtained from tissue tracking measurements using different software packages. Hence, it is essential to develop reference standards from each technique and analytical product for clinical use, and to sequentially compare patient data using the same software.

T1/T2 mapping: CMR T1 and T2 mapping are relatively new quantitative non-contrast CMR protocols being explored for multiple research applications, particularly in assessment of myocardial function following chemotherapy. For example, an increase of T1 signal has been reported post-chemotherapy compared to pre-treatment values [42]. The quantification of regional T1 (longitudinal relaxation time and an indication of myocardial fibrosis and inflammation) and T2 (transverse relaxation time and an indication of myocardial edema) values for specific tissues can serve as biomarkers to detect myocardial disease and damage [43]. In addition, extracellular volume (ECV) maps derived from pre-contrast T1 and post-contrast T1 mapping can reflect the volume of myocardium that is not occupied by cells, which correlates with the collagen volume fraction due to myocardial edema [42], [44]. This may reveal damages not noticeable in regular T1 mapping dataset. ECV deviation from normal range may be an indication of different pathologies like myocardial fibrosis, inflammation, and edema [45]. High doses of radiation to the heart following RT are associated with acute and chronic changes, including edema, fibrosis, and other extracellular matrix changes [20]. Thus, exploration of the spatiotemporal correlations of

changes in myocardial T1/T2 signal, MRI-derived strain, LGE volume, and radiation dose could open doors for future prediction of myocardial injuries associated with RT.

At 3T field strength, the normal range of T1 signal in myocardium derived from the modified Look-Locker inversion recovery (MOLLI) method has been reported to be 1052 ± 23 ms [43]. It should be noted that demographics, such as sex and age, and environment settings like temperature may change the normal T1 range [43]. Similar to T1, T2 signal is also affected by various demographics; the normal T2 signal range for the myocardium acquired from a steady-state free precession (SSFP) technique has been found to be 45.1 ms at 3T MRI [43]. Finally, normal myocardial ECV for healthy individuals has been reported to be 0.26 ± 0.04 at 3T [43].

Another factor that impacts T1, T2, and ECV measurements reliability is the temporal variability and how it can differ between patients versus healthy control. Interestingly, it has been shown that for a 1.5T magnetic field, the minimal detected difference for T1 (29 ms), T2 (3.0 ms), and ECV (2.2%) in healthy participants approached the mean temporal changes in patients with cancer-therapeutic-related cardiac dysfunction with the least overlap observed for native T1, suggesting that temporal variability of tissue characterization parameters is still a challenge for their current clinical application in individual patients receiving cancer therapy [46]. Also, it implies that any measured temporal changes close to the minimal detectable difference should be carefully monitored to see if the changes were actually in regards to biological parameters or temporal variability errors.

4D Phase-Contrast (PC) MRI: 4D flow imaging is a technique used to assess cardiac and vascular hemodynamics by directly encoding kinematic information of flowing blood in the phase data of a stack of images in four dimensions (x, y, and z spatial dimensions, and time) to provide time-resolved 3D velocity fields [47]. This method enables global and regional analyses of patient-

specific velocity profiles, streamlines, particle tracings, pressure gradients, and wall shear stress in multiple locations in the heart and vasculature [48].

The normal range of wall shear stress (WSS) has been shown to be different over various region of aorta. In the thoracic aorta, WSS is dominated by axial flow, and the average peak systolic WSS value in the arch and ascending aorta is approximately 1.79 ± 0.71 Pa and 2.23 ± 1.04 Pa, respectively [49]. In other studies, WSS in the suprarenal aorta was reported as 1.04 Pa at the posterior wall and 0.86 Pa at the anterior wall. In the infrarenal aorta, WSS values were 0.47 Pa at the posterior wall and 0.61 Pa at the anterior wall [50].

LGE MRI: As a non-invasive MR sequence, LGE MRI has clinically shown great importance in detection of fibrotic scar tissue in the myocardium [51]. This contrast-enhanced sequence highlights regions with increased proportion of extracellular space to detect ischemic and non-ischemic fibrosis [51]. Notably, this regional biomarker has been shown to be able to detect the cardiotoxicity following radiotherapy in patients receiving radiation doses greater than 30 Gy [52]. In normal healthy individuals, the percentage of enhanced myocardial area is expected to be zero. In patients who have undergone RT, the percentage of LGE and dose were described to be 15% in regions exposed to 40-60 Gy of radiation and 21% in regions with exposed to >60 Gy [44].

1.3. Image registration
In general, image registration is a transformation process in which one image set is mapped onto another image set through translation, rotation, shrinkage, and/or expansion. Image registration can be rigid (i.e., only translation and/or rotation) or non-rigid/deformable (i.e., rigid registration in addition to homogeneous or heterogeneous scaling) based on the degree of deformation. The exact properties of the heterogeneous deformation are accomplished through spatial transformation (i.e., based on dimensions), interpolation (i.e., based on intensity), similarity

measurement (i.e., based on surface features), and optimization [14], [15]. Per AAPM guidelines, the most validated approach to confirm the accuracy of image registration is for the user to check the overlap of the two images and make changes where required [16]. In addition, AAPM Task Group (TG) No. 132 suggests that in an accurate image registration, similarity metrics such as Dice (i.e., degree of overlap of two images with 0 being the least overlap and 1 being perfect overlap) should be greater than 80% (or 0.8) and mean distance to agreement (MDA) (i.e., the average distance from one point of an image to a similar point in the secondary image) should not exceed 3 mm [17].

For all the image registrations involved in this project, MIM software (MIM Software Inc, Cleveland, OH) was used to perform the rigid/deformable registrations, transfer the dose between the planning CT and MR sequences, and correct for the respiratory- and cardiac-motion-induced dose variations. The image registration in MIM software is implemented based on an intensity-based free form algorithm. One image set is always considered as the reference or the primary dataset which is fixed; the secondary image set is deformed based on point-by-point correspondence using a coarse-to-fine multi-resolution approach. First, gross differences are adjusted using a coarse grid, and then resolution is increased and the local changes are improved over a small scale. Finally, the registration is optimized by a gradient descent-based algorithm [53], [54]. To validate the intra- and inter-modality image registration process, the Reg Refine tool in MIM software can be utilized to assess the registration accuracy with high resolution point-by-point evaluation of imaging overlap, in addition to measurement of the image registration similarity mapping metrics (e.g., MDA and Dice) and comparison of the results with the existing guidelines (e.g., AAPM TG 132) [54], [55].

The next chapter (Chapter 2) will focus on the application and workflow of using image registration (rigid and/or non-rigid or deformable) tools to register the dosimetry map between CT and MR modalities and more importantly, to account for the cardiopulmonary-motion-induced dose variation on organs at risk (e.g., LV and LV myocardium (LVM)) via rigid and deformable image registration globally and regionally (i.e., further segmentation of LVM into AHA model) and finally to estimate of the cumulative LV/LVM dose over the cardiac cycle at breath-hold over global and regional segments of the LVM.

Following the image registration chapter, the next two chapters will focus on a longitudinal project regarding quantification of RT-induced CVT in lung cancer patients by comparing cardiovascular metrics between baseline, three months post-RT completion, and six months post-RT completion. Specifically, Chapter 3 includes the details of using multiple MR sequences (cine MRI, DENSE MRI, T1/T2 mapping, and LGE) to monitor the patient-specific evolution of quantitative global and regional cardiac function before and after RT regionally and globally. In Chapter 4, spatiotemporal evolution of global aortic function across the same dataset will be discussed. In addition, the use and correlation of 4D phase-contrast MRI for the quantification of blood flow metrics will be evaluated, and the possibility of correlation between aortic dose and cardiac dysfunction will be evaluated and discussed. For both Chapters 3 and 4, the correlation of the registered RT dosimetry map and changes in MRI-derived metrics will also be quantified regionally and globally over 3-months and 6-months follow-up. Finally, Chapter 5 will provide a summary of all the projects in addition to recommendations for future works.

2 Image registration and accounting for cardiopulmonary motion-induced dose variation

2.1. Introduction

Optimum registration of the local quantitative radiation dose from non-cardiac and non-respiratory gated RT treatment planning to the thoracic anatomy that is continuously moving due to cardiac and respiratory motion is challenging in many ways. First, RT dose calculation is done on CT images while the cardiac functional/structural measurements are derived from MRI-based metrics. In order to find the correlation between the cardiac metrics and RT dose, a proper image registration workflow is required to map the dose from CT images onto MRI datasets. Second, planning CT is a non-cardiac gated and non-respiratory gated sequence while the cardiopulmonary motion can cause variation to the dose delivered to the heart and its substructures. Cardiopulmonary motion-corrections via image registration can improve the reliability of the actual dose received by the heart and its substructures for evaluations of RT-induced CVT.

Few studies have looked at the effects of cardiac and respiratory motion on the dose received by the heart and its substructures [56], [57]. It has been shown that in patients with breast cancer, the deep inspiration breath hold (DIBH) technique will minimize the radiation dose to the chest wall [58]. Despite the manageability of breathing motion, cardiac motion cannot be controlled the same way as breathing motion. In other words, cardiac motion is involuntary, much faster than the respiratory motion, and requires more sophisticated high-resolution techniques to be captured [8], [59], [60]. Even though cardiac motion is faster, it still affects the dose delivered to the heart and its substructures. In fact, studies have shown that the mean and maximum radiation dose to the LV or LVM is significantly different between systolic and diastolic cardiac phases [57], [61]. Though,

the behavior of dose variations during cardiac and respiratory motion depended on the prescribed dose (i.e., location of the tumor).

In order to account for the cardiorespiratory motion-induced dose variation, respiratory- and cardiac-gated sequences are required to assess the dose over various breathing and cardiac phases and calculate the cumulative dose over the cardiac or respiratory cycle via DIR. 4D-CT as a respiratory-gated but non-cardiac-gated sequence, and cine MRI as the cardiac-gated sequence in breath-hold along with a breath-hold volumetric MR dataset (i.e., T1-Volumetric interpolated breath-hold examination (VIBE)) as a bridge between the two modalities provide enough tools to quantify the dose variation on organs at risk (e.g., LV and LVM) over the respiratory and cardiac motion via rigid/deformable image registration techniques (direct image registration between cine MRI and CT images is not possible due to multimodality registration errors, fewer slices in cine images, and limitations in field of view (FOV)). Assessment of cardiac-motion- and respiratory-motion-induced dose variations will provide useful information regarding the magnitude of dose differences over these two motions over the area of interest. Among various heart substructures, LVM dose variation measurements are even more of interest given that LV muscle is responsible for pumping the blood to the circulatory system, and more importantly, the RT-induced cardiac damage will appear on myocardium rather than the blood pool [62]. In addition, further segmentation of LVM into the 16-segment AHA model provides regional dose information which can be used to find possible dose differences at local regions and to compare the values with global LVM and LV dose from MRI and CT datasets. Regional dose assessments are also helpful in evaluation of possible correlations between focal MRI-based metrics and focal radiation dose.

The rest of this chapter will focus on novel workflows created to use 4D-CT, T1-VIBE, and cine MR images to transfer/transform the dose over various breathing and cardiac phases, and estimate

the cumulative dose over the cardiac cycle on the LV, LVM and AHA model via rigid/deformable image registration globally and regionally.

2.2. Method

Patients: This study was approved by the Virginia Commonwealth University Institutional Review Board (IRB). Eight patients with lung cancer who were scheduled to receive radiotherapy and get at least 5 Gy of radiation to 10% of the volume of their heart were recruited for this study. Each patient provided an informed consent prior to enrollment. 4D-CT, T1-VIBE at expiration breath-hold, and cine MR images at expiration breath-hold were acquired for each patient at baseline. Individual patient characteristics are shown in Table2.1

Table 2.1 Individual patient characteristics.

Patient	Gender	Age	Prescribed dose (Gy)	Cancer Stage	Tumor location
1	Female	67	64	III	Left lung (upper lobe), posterior to the heart
2	Male	62	66	III	Right lung (mid lobe), posterior to the heart
3	Female	59	60	III	Right lung (upper lobe), superior to the heart
4	Female	70	66	III	Left lung (upper lobe), superior to the heart
5	Male	62	50	IV	Left lung (upper lobe), superior to the heart
6	Male	62	66	IV	Left lung (upper lobe), superior to the heart
7	Female	77	66	III	Right lung (upper lobe), superior to the heart
8	Female	58	66	III	Right lung (mid lobe), superior to the heart

Treatment planning: Each patient underwent a non-contrast non-cardiac- and non-respiratory-gated 4D-CT scan using a Brilliance Big Bore CT scanner (Philips Healthcare, Cleveland, OH). The scan covered the whole chest area with a slice thickness of 3 mm. A Philips bellows device was used to track the respiratory motion. Following scan completion, ten volumetric CT images were reconstructed to represent 0%-90% breathing phases including 0% as inspiration and 50% as expiration. In addition, an average intensity projection (AIP) dataset was generated by averaging the pixel intensities across all 4D-CT breathing phases. All treatment plans were created based on AIP. Dosimetry map for each patient is provided in the supplement (Figure 6.1).

The 30% breathing phase was chosen to contour the gross tumor volume (GTV). GTV was then propagated through all the phases to create the internal gross target volume (iGTV). The iGTV was expanded by 6-8 mm, and uninvolved organs such as the heart, esophagus, and bone were excluded to generate the internal target volume (ITV). Finally, ITV was expanded by 5 mm to create the planning target volume (PTV). The volumetric modulated arc therapy (VMAT) technique was used to deliver the prescribed dose to PTV using daily treatments Monday through Friday. Treatment planning was performed using ECLIPSE (Varian Medical Systems, Palo Alto, CA, USA).

MR imaging: T1-VIBE MRI scan was acquired for the whole chest area at expiration breath-hold with slice thickness of 2 mm, echo time (TE) 1.33 ms, repetition time (TR) 4.1 ms, echo train length (ETL) 2, flip angle: 9º, and pixel size 1.19x1.19 mm. Following T1-VIBE acquisition, cine images were also obtained at expiratory breath-hold and covered the whole LV from the aortic valve down to the apex of the heart with slice thickness of 1 cm, TE 1.24 ms, TR 42.9 ms, flip angle 40º, ETL 1, and pixel size 1.33x1.33 mm. 8-10 slices were enough to encompass the whole LV. Each cine dataset consisted of 25 cardiac phases including systole and diastole. Both T1-VIBE

and cine MR images were acquired on a 3T MRI platform (MAGNETOM Vida from Siemens Healthineers) scanner.

Contouring: The LV was manually contoured on all 4D-CT breathing phases (0%-90%) including inspiration (0%) and expiration (50%) from the aortic valve down to the apex of the heart following anatomical landmarks and published guidelines [63]. In cine image, the slices of the LV from each cardiac phase (1-25 phases) were grouped together to create a volumetric MR image of the LV. Following the same landmarks and guidelines as LV segmentation on 4D-CT dataset, the LV was contoured on all 25 cardiac phases of cine MR images including systole and diastole. Systole and diastole cardiac phases were chosen per Society of Cardiac Magnetic Resonance (SCMR) Imaging guidelines [64]. The mid-ventricular slice of the LV cine images was chosen and the systolic and diastolic phases were picked based on the smallest and largest blood pool area in short axis view, respectively [65]. Following LV segmentation on cine images, the blood pool was extracted from contoured regions to derive the LVM on short axis slices. Each LVM contour was further manually segmented into the AHA model to calculate the dose on segments 1-16 of the AHA model.

Image registration: To map the radiation dose from the AIP onto MR sequences, T1-VIBE as a volumetric MRI sequence was considered as the primary dataset and AIP was considered as the secondary dataset. The two modalities were either rigidly or non-rigidly (based on the degree of deformation between the primary and secondary datasets) registered using the image registration package within MIM software (MIM Software Inc, Cleveland, OH). The image registration algorithm details were discussed in chapter 1. Following image registration, the dosimetry map was transferred from the AIP dataset onto T1-VIBE and from there onto other MRI sequences (Figure2.1). In Figure2.1, AIP dose can be directly transferred onto T1-VIBE without 50% 4D-CT intervention but direct registration of the dosimetry map from AIP onto 2D MRI sequences is not

possible due to limited FOV in 2D MR images. The workflow shown in Figure 2.1 can be expanded to transfer the dose from AIP to any 2D MRI sequences (e.g., T1 mapping) provided that the appropriate registration (i.e., rigid or deformable based on degree of deformation) with consistent inspection of overlap is done by the user. In order to quantify the dose variation due to cardiac and respiratory motion, a few extra steps including transformation of dosimetry map over all the respiratory and cardiac phases and calculation of the cumulative dose via DIR between multiple cine phases with respect to a reference phase is required. More details are provided below.
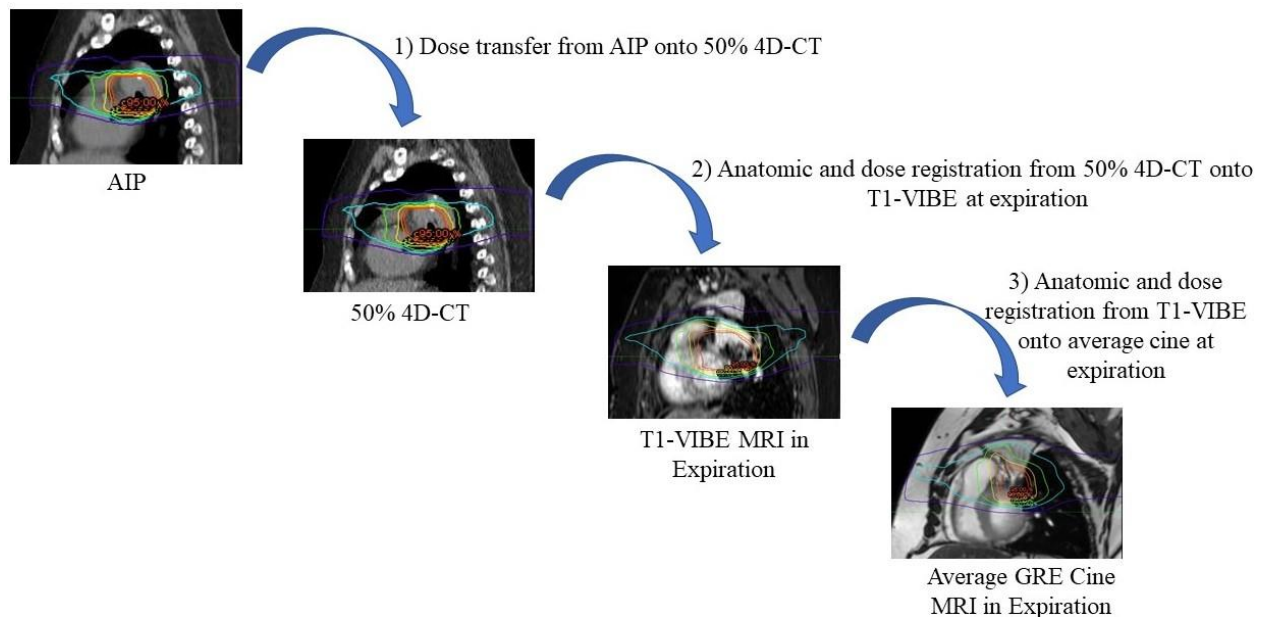
Figure2.1 Workflow of dose transfer from AIP to average cine MRI.

Respiratory-motion-induced dose variation on the LV: in order to evaluate the dose variation on the LV due to respiratory motion (with intrinsic cardiac motion) in 4D-CT dataset, the dosimetry map on AIP dataset was rigidly transferred onto all ten breathing phases including inspiration (0% 4D-CT) and expiration (50% 4D-CT). Dose volume histogram (DVH) was calculated for the

contoured LV area and the mean and maximum doses were calculated based on the acquired DVH. Figure2.2 demonstrates the workflow of dose transfer to various respiratory phases.
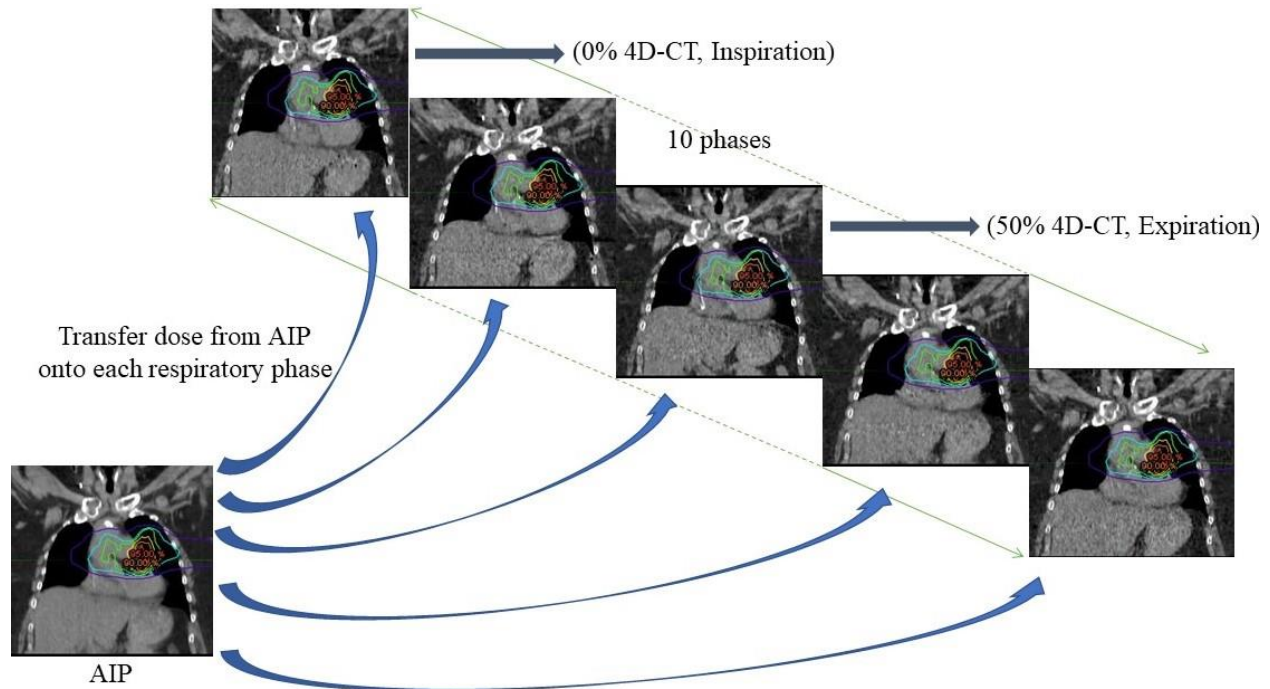
Figure 2.2. Workflow of dose transfer from planning CT (AIP) onto respiratory phases.

Cardiac-motion-induced dose variation on the LV and LVM: To investigate the dose variation due to cardiac motion, the 50% 4D-CT was registered onto T1-VIBE sequences at expiration (rigidly or non-rigidly based on the degree of deformation), and the dosimetry map was transferred onto T1-VIBE MR following the image registration process. The T1-VIBE was further registered onto average cine MRI (i.e., a dataset obtained from averaging pixel intensities across all the cardiac phases (1-25) of cine MRI dataset) at expiration breath-hold. The dosimetry map on average cine MRI was finally transferred onto each cardiac phase to monitor the dose variation over the cardiac cycle including systole and diastole phases. Maximum and mean doses were calculated based on the DVH derived from contoured LV and LVM areas. Figures 2.3 is the work flow of dose transfer from average cine MRI onto multiple cardiac phases.
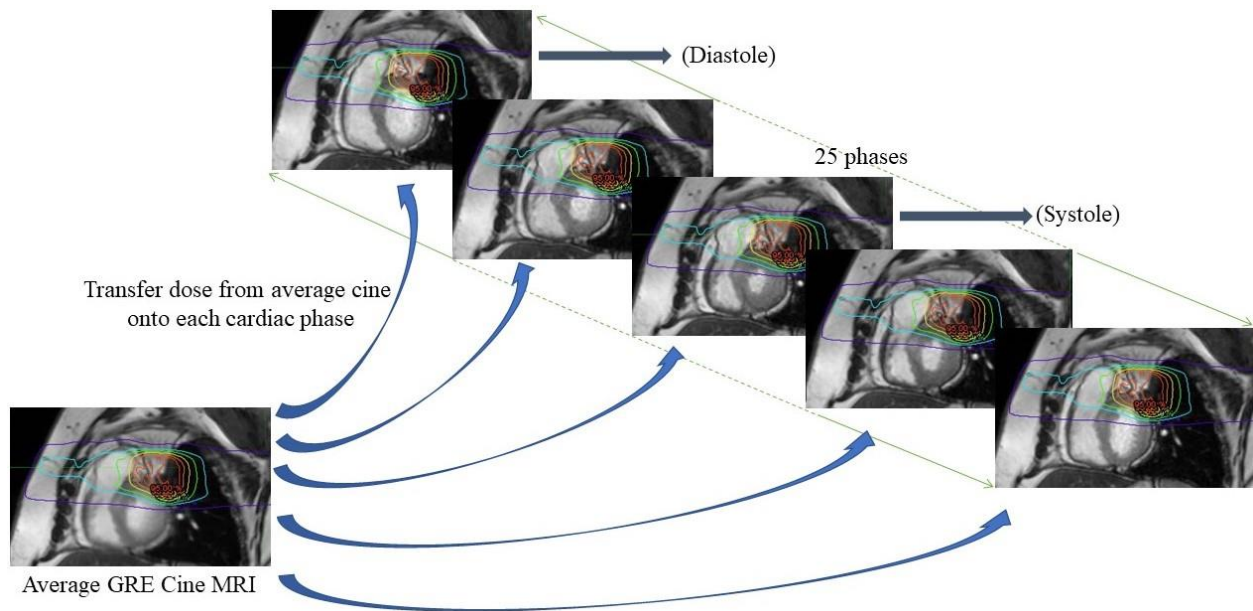
Figure 2.3 Workflow of dose transfer from average cine onto cardiac phases

Cumulative LV and LVM dose over cardiac cycle: To obtain the cumulative dose on the LV and LVM over all cardiac phases, each cardiac phase was deformably registered onto a reference cine phase (e.g., phase 1) and the dosimetry map from each cardiac phase was transformed onto the reference cine phase following the registration process. All 25 transformed doses on the reference cine phase were accumulated and scaled by 1/25 to calculate the cumulative LV and LVM dose over the cardiac cycle. Dose values were determined from the DVH diagram and absolute and relative mean and maximum doses (i.e., relative to AIP as discussed below) were obtained subsequently. Figures 2.4-2.5 demonstrate the workflow for dose transformation from each cardiac phase onto reference cine and accumulation of dose following DIR.
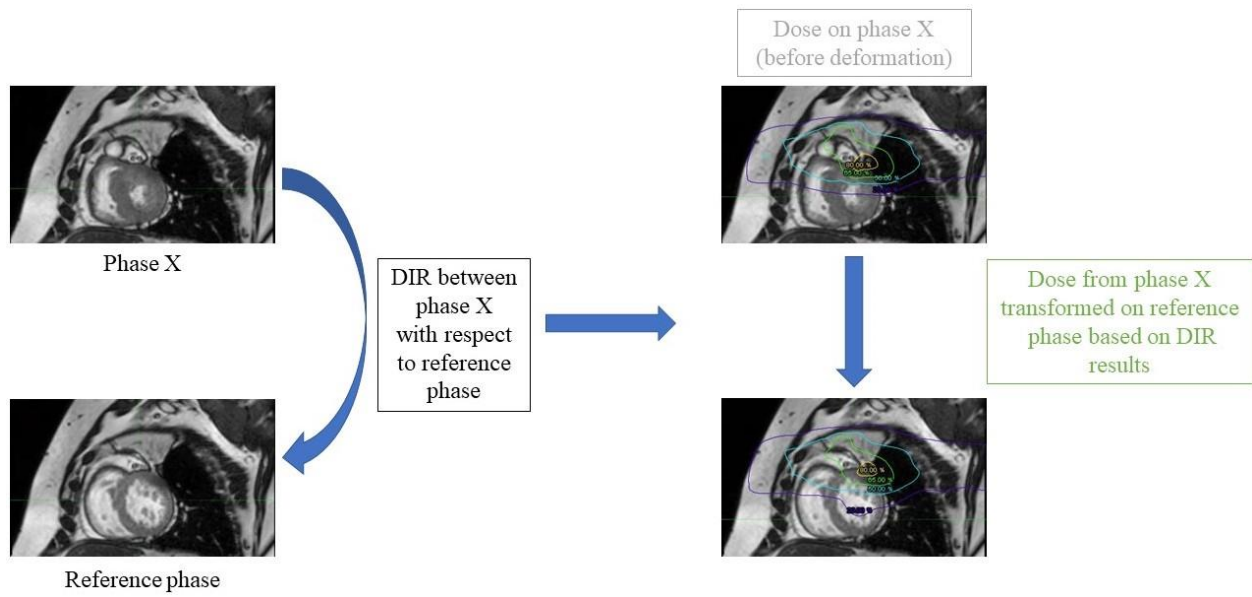
Figure 2.4. Workflow of dose transformation from each cardiac phase onto a reference cine phase.
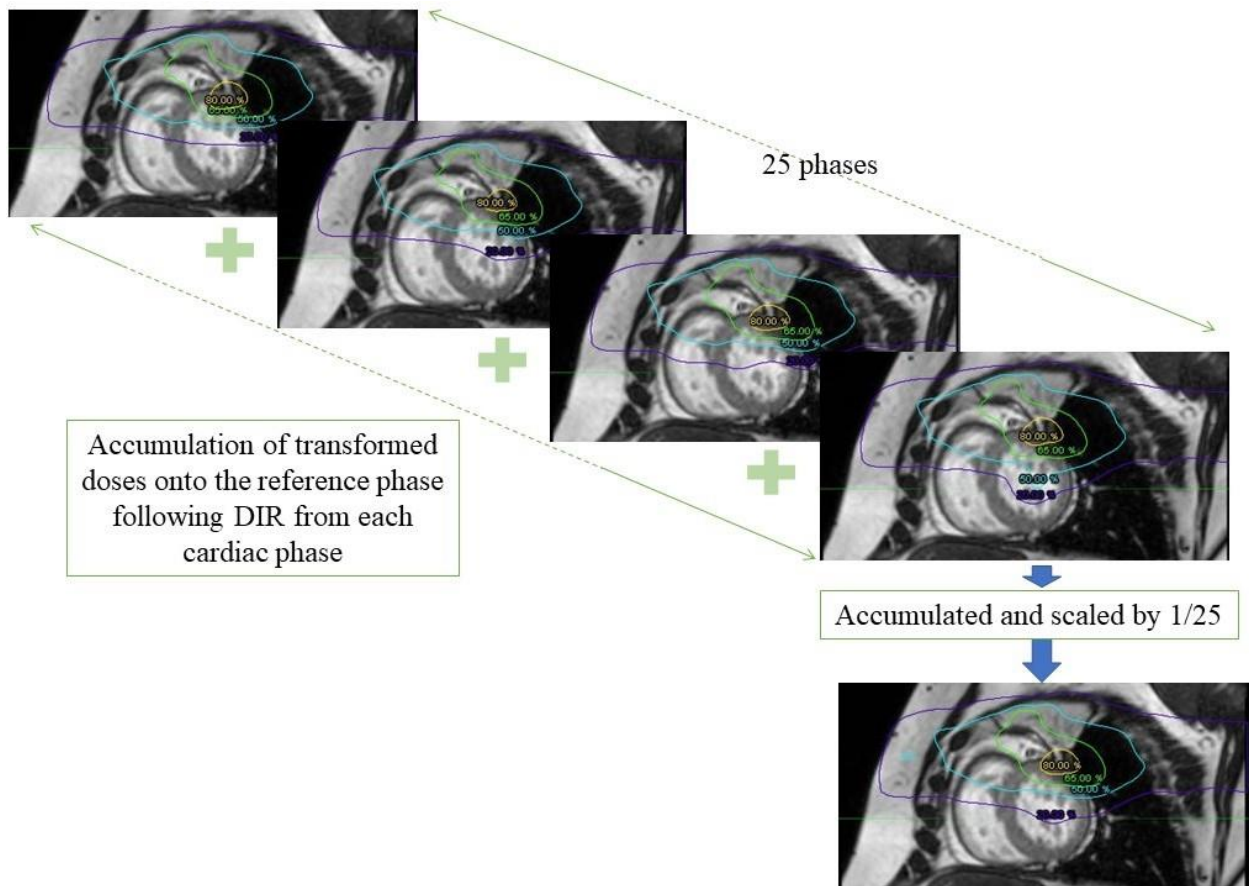
Figure 2.5. Workflow of dose accumulation from all cardiac phases on a reference cine phase.

In addition to dose measurements, the displacement of the LV was measured during respiratory and cardiac motion. The maximum LV displacement during respiration was acquired from the movement of the center of mass of the contoured LV volume between inspiration and expiration phases. During cardiac motion at expiration breath-hold, the maximum LV displacement was measured from the movement of the LV center of mass between systolic and diastolic phases. The displacement was measured in anterior-to-posterior (AP), right-to-left (RL), and superior-to-inferior (SI) directions and the 3D displacement was measured from the square-root of the sum of the squares of each directional displacement.

To better compare the doses between various modalities, patients, and processing techniques, all dose values were reported as doses relative to the AIP dose; that is, the relative maximum and mean dose were calculated as ((maximum dose – maximum AIP dose)/(maximum AIP dose))*100 and ((mean dose – mean AIP dose)/(mean AIP dose))*100, respectively. All reported dose values are for the population average unless specified.

Statistics: Unequal ANOVA test was used to investigate significant differences in relative maximum and mean doses on the LV between various breathing phases. Student's t-test was used to determine potential significant differences between the systolic and diastolic cardiac phases on the LV and LVM, systole and 50% 4D-CT on the LV, diastole and 50% 4D-CT on the LV, cumulative LV dose and 50% 4D-CT LV dose, regional cumulative doses on the LVM and 50% 4D-CT on the LV, and finally between the respiratory-motion-induced LV displacement and cardiac-motion-induced LV displacement. All the statistical analyses were done using JMP software (version Pro 14, SAS Institute Inc., NC, USA) with statistical significance of 0.05.

2.3. Results

Respiratory-motion-induced dose variation on the LV: the absolute maximum, absolute mean, relative maximum and relative mean dose on the LV ranged between 35±24.5–37.8±26 Gy, 6.9±6.7–9.6±8.3 Gy, -4.5±10.7–5.6±31.4%, and -14.2±12.7–16.5±13.1%, respectively. Significant relative mean dose differences were noted between inspiration and expiration breathing phases, namely, between the 0% 4D-CT and 50%-60%70%-80% 4D-CT (P<0.0145) and between 10% 4D-CT and 50%-60%-70%-80% 4D-CT (P<0.0125). No significant relative maximum dose differences were noted between breathing phases including AIP (P>0.78). Maximum LV displacement was 0.4(±0.3) cm, 0.2(±0.1) cm, and 0.3(±0.3) cm, in SI, AP, and RL directions, respectively with a 3D magnitude of 0.6(±0.2) cm. Table 2.2 is the list of relative maximum and mean doses over respiratory phases, and the graphical representation is shown in Figure 2.6. Table 2.3 is the summary of P-values from statistical measurements between breathing phases.

Table 2.2 Relative maximum and mean LV dose over respiratory phases

	Relative Maximum Dose (%)			Relative Mean Dose (%)		
	Average	Range		Average	Range	
AIP	0	0	0	0	0	0
0% 4D-CT	-3.5	-19.1	7.3	-13.9	-26.2	-0.6
10% 4D-CT	-4.5	-21.9	10.7	-14.2	-40.3	-1.3
20% 4D-CT	0.2	-17.3	22.3	-1.6	-8.4	11.2
30% 4D-CT	1.9	-5.3	14.0	4.5	-17.3	27.7
40% 4D-CT	3.9	-10.9	36.0	3.5	-25.9	18.0
50% 4D-CT	2.7	-4	25.9	11.2	-1.6	25.6
60% 4D-CT	5.6	-4.4	31.4	16.5	-1.2	33.2
70% 4D-CT	1.6	-14.2	31.4	9.1	-8.6	30.4
80% 4D-CT	3.3	-3.5	37.4	7.5	0	23.0
90% 4D-CT	2.9	-4.1	31.9	-1.7	-29.2	14.9

Table2.3. summary of P-values from the statistical tests on the relative mean dose differences among various breathing phases.

	0% 4DCT	10% 4D-CT	20% 4D-CT	30% 4D-CT	40% 4D-CT	50% 4D-CT	60% 4D-CT	70% 4D-CT	80% 4D-CT	90% 4D-CT
AIP	0.36	0.33	1	0.99	0.99	0.67	0.15	0.88	0.96	1
0% 4D-CT		1	0.55	0.065	0.1	**0.0017**	**0.0001**	**0.006**	**0.0145**	0.55
10% 4D-CT			0.51	0.057	0.09	**0.0014**	**0.0001**	**0.0051**	**0.0125**	0.52
20% 4D-CT				0.99	0.99	0.48	0.075	0.73	0.88	1
30% 4D-CT					1	0.98	0.59	0.99	1	0.99
40% 4D-CT						0.95	0.47	0.99	0.99	0.99
50% 4D-CT							0.99	1	0.99	0.57
60% 4D-CT								0.97	0.9	0.073
70% 4D-CT									1	0.73
80% 4D-CT										0.88
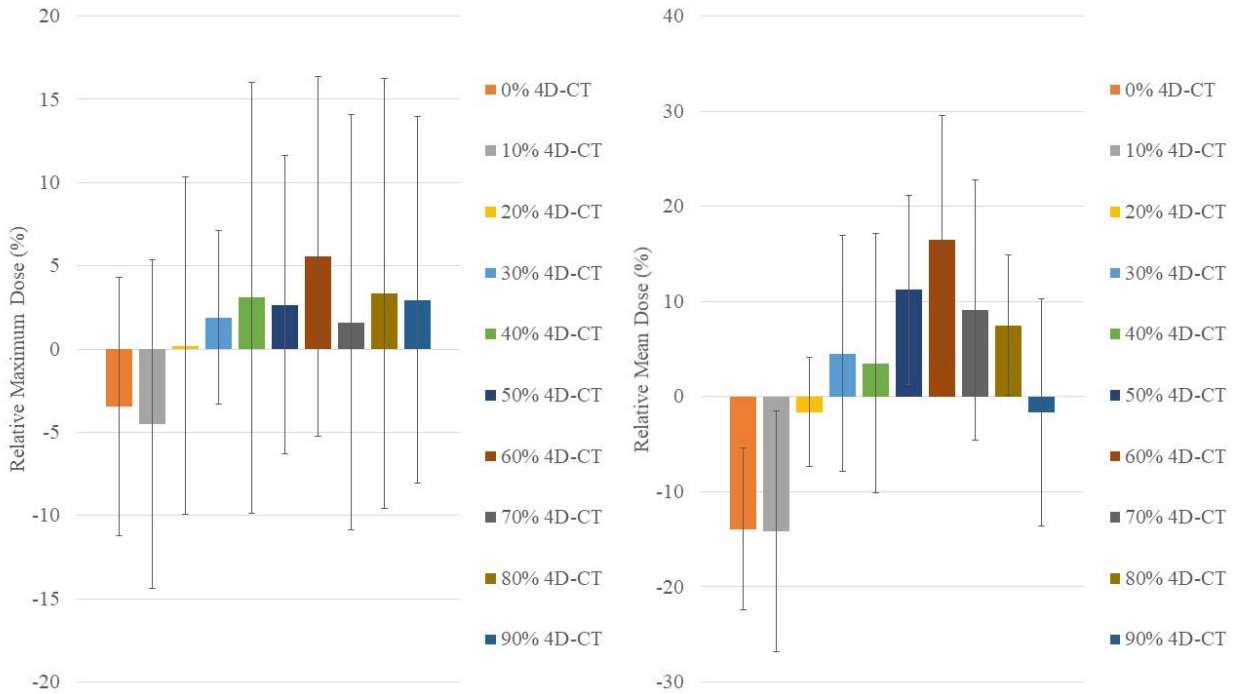
Figure2.6. Relative maximum and mean LV dose over 0%-90% breathing phases (±SD).

Cardiac-motion-induced dose variation on the LV and LVM at expiratory breath-hold: the absolute maximum, absolute mean, relative maximum and relative mean LV dose ranged between 31.4±22.6–36.3±22.6 Gy, 5.8±5.0–7.8±6.5 Gy, 2.1±14.5–67.9±111.1%, and 0.1±11.8–30.1±23.5%, respectively. Significant relative mean LV dose was noted between systole and diastole cardiac phases (diastole 25.1%, systole 2%, P=0.037). No significant differences were noted in the relative maximum LV dose between systole and diastole phases (51.4% vs. 6% P=0.074). Also, no significant relative mean or maximum dose differences were noted between systole or diastole and 50% 4D-CT on the LV (relative mean dose at systole: 2% vs. 11.2%, P=0.14; relative maximum dose at diastole: 51.4% vs 2.7%, P=0.24; relative mean dose at diastole: 25.1% vs. 11.2%, P=0.2).

46

In regards to the LVM, the absolute maximum, absolute mean, relative maximum and relative mean LVM dose ranged between 31.4±22.6–36.3±22.6 Gy, 6.3±5.2–8.7±7.2 Gy, 2.1±14.5–67.9±111.1%, 5.1±10.3–42.5±27.4%, respectively. Similar to LV, significant relative mean doses were found between systolic and diastolic phases (diastole 37.8%, systole 6.8%, P=0.0157). No significant differences were shown in the relative maximum dose on the LVM between systolic and diastolic cardiac phases (6% vs. 51.4% P=0.074).

Table 2.4 provides a summary of relative maximum and mean LV/LVM dose over the cardiac cycle. Figure 2.7 shows the distribution of maximum and mean dose relative to AIP and 50% 4D-CT and figure 2.8 represent the dose value on systolic and diastolic phases.

Table 2.4. Summary of relative maximum and mean LV/LVM dose values over the cardiac cycle.

Cardiac Phases	Relative Maximum Dose (%)			Relative Mean Dose (%)					
	Both LVM and LV			LVM			LV		
	Average	Range		Average	Range		Average	Range	
1	67.9	-2.1	321.3	42.5	-12.4	83.6	30.1	-11.1	59.3
2	59.2	-2.1	244.4	40.5	-13.4	66	29.7	-11.4	56.0
3	54.8	-2.1	194.2	34.1	-14.7	56.8	24.3	-12.4	51.2
4	26.9	-2.1	100	25.5	-16.8	49.8	16.1	-13.2	46.7
5	17.4	-2.1	50.8	19.4	-16.5	47.0	12.8	-12.4	41.8
6	7.6	-3.1	47.1	13.6	-16.5	43.6	4.7	-11.4	36.5
7	4.9	-10.3	48.3	9	-16.3	31.9	2.3	-17.2	31.8
8	2.1	-11.9	34.9	7.7	-17.6	30.4	0.2	-16.7	21.2
9	4.3	-7.2	43.4	7	-17.8	24.3	1.6	-10.9	19.3
10	5.8	-15.1	61.1	5.1	-16.0	21.3	0.1	-18.2	16.5
11	8.1	-13.2	48.1	6.7	-15.0	20.6	0.9	-14.0	16.1
12	12.5	-4.2	48.0	11.6	-14.7	39.5	4.4	-11.9	17.1
13	10.6	-2.2	32.8	16.5	-12.7	56.7	7.2	-10.6	26.2
14	7.8	-2.2	48.3	19.1	-12.9	72.8	8	-11.1	33.6
15	8.7	-2.3	37.2	20.5	-11.6	74.1	8.7	-11.1	37.4
16	8	-2.1	31.7	21.5	-11.6	77.8	9.5	-11.4	41.1
17	13.5	-2.1	43.1	23.1	-11.6	76.9	10	-11.1	40.8
18	13.3	-2.1	44.0	23.3	-13.2	76.0	10.9	-11.6	41.0
19	11.9	-2.1	55.7	24.6	-13.2	75.7	12.1	-11.4	43.6
20	12.6	-2.1	52.2	26.8	-13.2	72.2	16.1	-11.9	45.8
21	19.4	-2.1	69.6	29.6	-13.4	79.1	17.7	-11.6	47.2
22	24.3	-2.1	82.7	30.1	-13.2	68.3	19.2	-11.6	49.6
23	26.3	-2.1	94.8	36.7	-15.0	79.9	25.2	-12.1	54.5
24	37.9	-2.1	120.2	33.7	-14.0	81.1	22.6	-26.0	54.4
25	64.1	-2.1	291.6	41.8	-12.4	85.5	29.7	-11.6	58.7
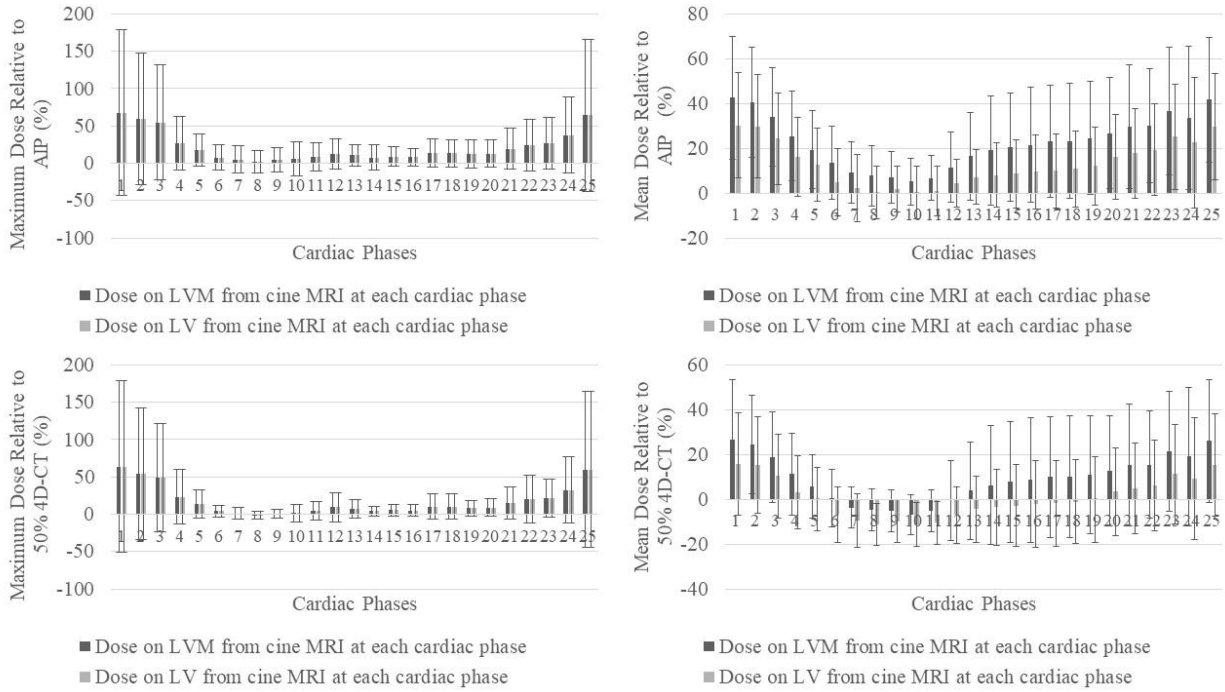
Figure 2.7. LV/LVM maximum and mean doses relative to AIP and 50% 4D-CT over the cardiac cycle.
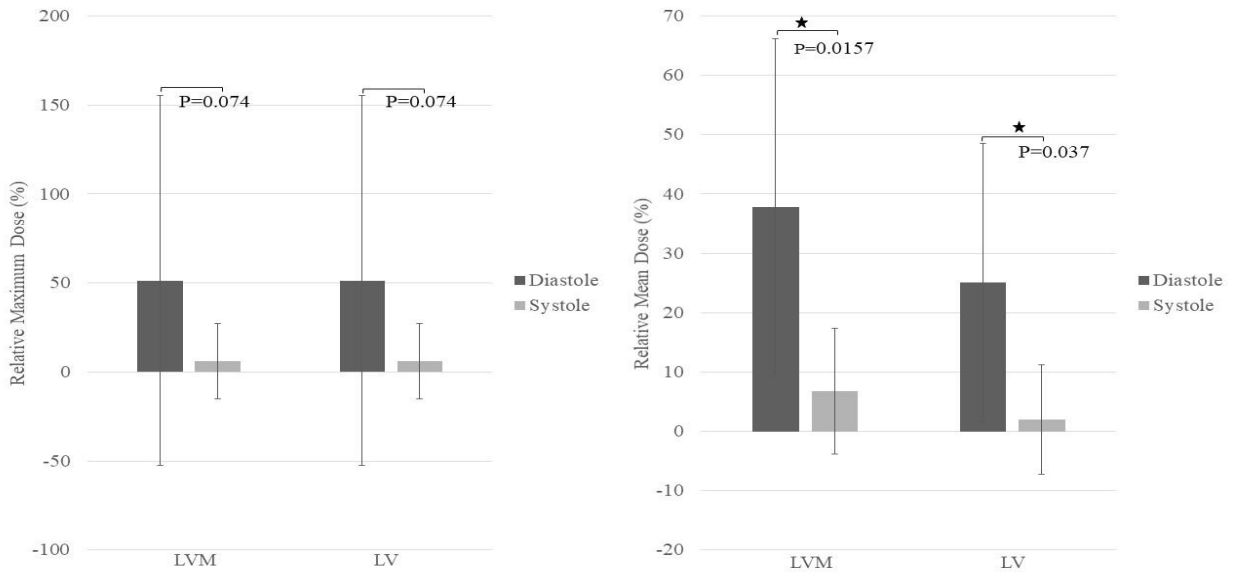
Figure 2.8. Relative maximum and mean LV/LVM dose over systolic and diastolic phases.

The maximum LV displacement during cardiac motion (between systole and diastole) at expiratory breath-hold was 0.4(±0.4) cm, 0.4(±0.4) cm, and 0.2(±0.1) cm in SI, AP, and RL directions, respectively with a 3D displacement magnitude of 0.7(±0.4) cm.

49

Cumulative dose over the cardiac cycle on the LV and LVM: the relative maximum and mean cumulative dose on the LV were 16.4%, and 13%, respectively. No significant differences were found either between the cumulative LV maximum dose and 50% 4D-CT maximum dose (P=0.54) or the cumulative LV mean dose and 50% 4D-CT mean dose (P=0.83).

Though, segmental analysis based on AHA model demonstrated dose variations at various locations in the myocardium. The relative mean cumulative dose on the LVM showed significant differences at regions closer to tumor location (segments 1, 2, 6, 7) compared to global relative mean dose from 50% 4D-CT (P<0.0117). Notably, the amount of mean radiation dose was found to be 2-3 times higher than the reported values from the global LV dose from 50% 4D-CT (~9 Gy vs 28 Gy). Additionally, the majority of the regional maximum LVM doses by cine MRI were significantly less than the estimated maximum LV dose from expiratory 4D-CT. Table 2.5 shows the statistical analysis results for segmental evaluation of relative maximum/mean cumulative dose based on the AHA model and the global dose from 4D-CT (50%). Figure 2.9 represents absolute mean cumulative dose and 50% 4D-CT dose on the AHA model. Figure 2.10 is a comparison between cumulative LV dose, cumulative LVM dose, and dose on 50% 4D-CT with intrinsic cardiac motion.

Table 2.5. Statistical analysis of (1) segmental relative maximum/mean cumulative dose based on AHA model and (2) global 50% 4D-CT dose on the LV.

Sector	Corresponding anatomical position	Relative max dose (%)			Relative mean dose (%)		
		(1)	(2)	P-value	(1)	(2)	P-value
AHA 1	**basal anterior**	-0.9	2.7	0.24	**231.5**	**11.2**	**0.0117**
AHA 2	**basal anteroseptal**	**-17.9**	**2.7**	**0.05**	**139**	**11.2**	**0.0117**
AHA 3	basal inferoseptal	-71.4	2.7	0.0008	-29.2	11.2	0.2
AHA 4	basal inferior	-82.8	2.7	0.0008	-58.9	11.2	0.0008
AHA 5	basal inferolateral	-59.8	2.7	0.0008	-20.5	11.2	0.0117
AHA 6	**basal anterolateral**	**-20.8**	**2.7**	**0.05**	**93.5**	**11.2**	**0.0046**
AHA 7	**mid anterior**	**-31.9**	**2.7**	**0.0011**	**114.1**	**11.2**	**0.0117**
AHA 8	mid anteroseptal	-42.8	2.7	0.0008	28.8	11.2	0.4
AHA 9	mid inferoseptal	-81.7	2.7	0.0008	-50.5	11.2	0.0008
AHA 10	mid inferior	-87.7	2.7	0.0008	-67.9	11.2	0.0008
AHA 11	mid inferolateral	-72.4	2.7	0.0008	-50.1	11.2	0.0008
AHA 12	mid anterolateral	-52.6	2.7	0.0011	14.4	11.2	0.83
AHA 13	apical anterior	-75.8	2.7	0.0008	-33.5	11.2	0.015
AHA 14	apical septal	-82.1	2.7	0.0008	-65.9	11.2	0.0008
AHA 15	apical inferior	-91.5	2.7	0.0008	-77.9	11.2	0.0008
AHA 16	apical lateral	-80.6	2.7	0.0008	-63.5	11.2	0.0008
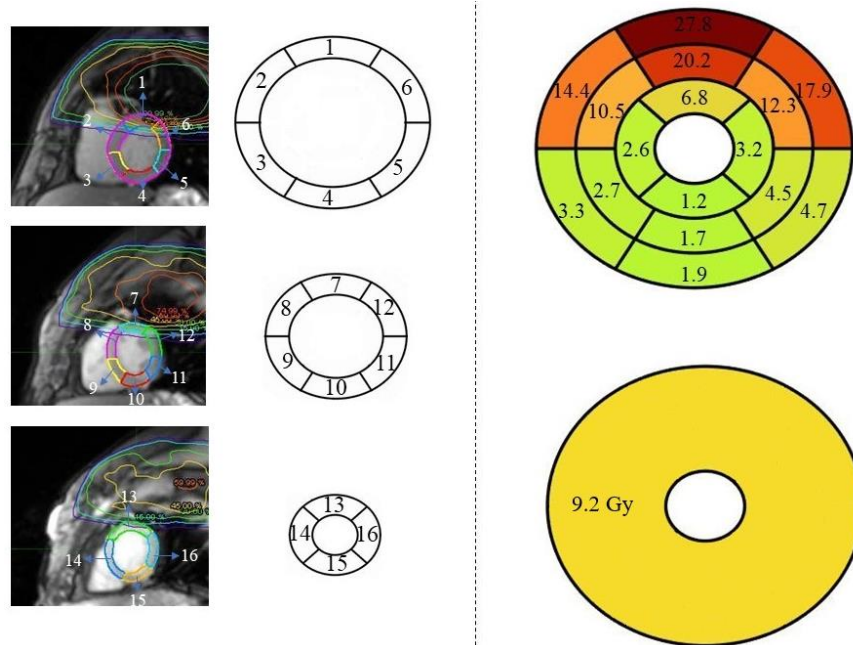
Figure 2.9. Left: a typical AHA model from base, mid and apical slices of the LV. Right: AHA model for the absolute cumulative dose on the LVM (top right) and the global LV dose on 50% 4D-CT (bottom right).

51
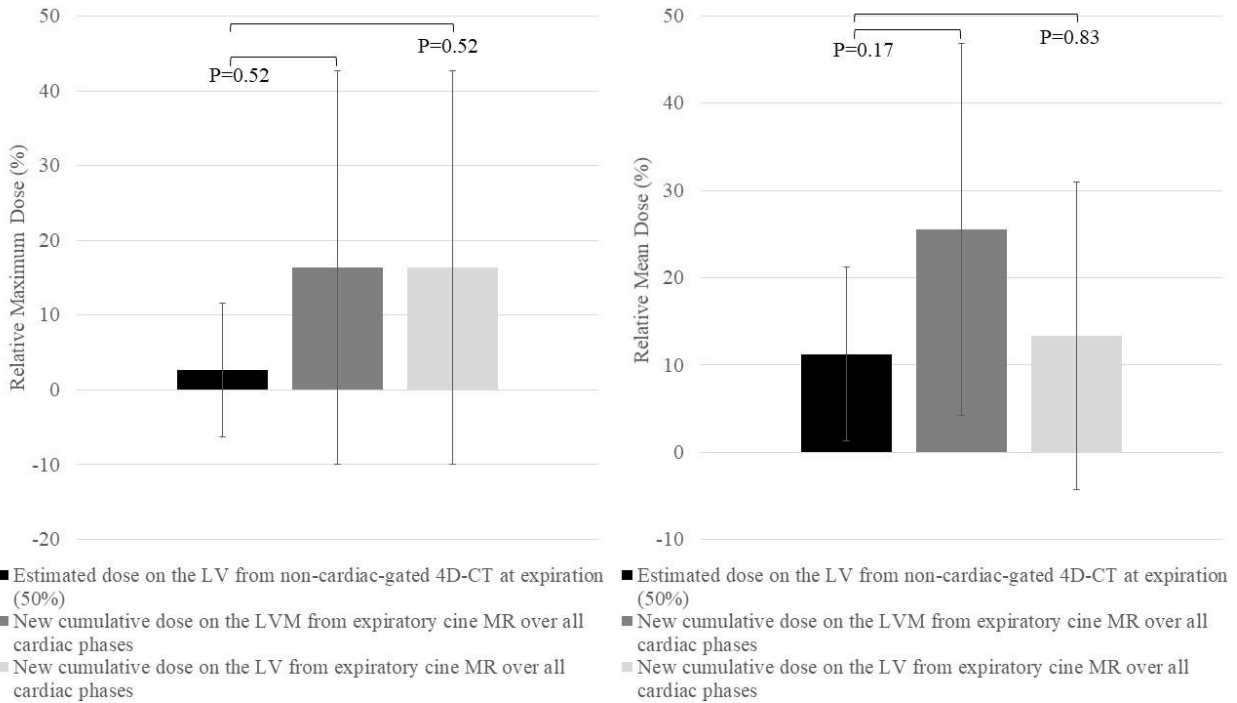
Figure 2.10. Comparison between the LV dose on 50% 4D-CT, cumulative LV dose, and cumulative LVM dose in terms of relative maximum/mean dose.

2.4. Discussion

The similar range of LV displacement due to respiratory 0.6(±0.2) cm and cardiac motion 0.7(±0.4) cm suggests that the LV dose variations may be impacted by both motions similarly. In this study, 6 of 8 patients had their tumor in the upper right or left lobe of the lung; the other two were in the middle lobe of the right lung. Thus, on average, the highest radiation dose was superior to the heart (i.e., closest to the anterior base of the heart). As a result, the ascending motion of the diaphragm (and heart) during expiration significantly increased the estimated mean cardiac dose relative to the inspiratory phase. Similar to the effect of respiratory motion, the close proximity of the tumor and basal/anterior regions of the heart led to elevated estimations of LVM dose during diastole (i.e., during maximum LV volume; cardiac phases 1-2) compared to systole (i.e., minimum LV volume; phases 8-10). That is, in this pilot population, LV contraction generally moved the anterobasal wall away from higher dose regions, but LV filling moved the wall toward the higher

52

doses. No significant changes between the relative maximum dose during respiratory motion and/or cardiac motion implies that at least part of the heart always remained in the high-dose region regardless of the respiratory/cardiac motion. Since the volume of the LV in non-cardiac gated 50% 4D-CT stays between systolic and diastolic cardiac phases, no significant dose variations were noted between systole or diastole and 50% 4D-CT dataset. The cumulative LV/LVM dose over the cardiac cycle did not show any significant differences to the dose from the corresponding breathing phase on the 4D-CT (50%) dataset; however, regional dose evaluation demonstrated significantly higher relative mean dose values in proximity of the tumor (2~3 times higher than 50% 4D-CT relative mean dose) while overestimating the dose at regions further away from the prescribed dose (e.g., apex of the heart).

The magnitude of LV relative maximum dose variation due to respiratory motion was around 10% between extreme breathing phases while the same metric went up to 65% for the cardiac motion. This is mostly due to close proximity of tumor to the LV among a few patients and dislocation of the LV to higher dose regions over the cardiac cycle. For the relative mean dose, both respiratory and cardiac motion showed a magnitude of 30% dose difference between extreme cardiac and respiratory phases. The least relative mean LV dose was noted in inspiration and systole compared to expiration and diastole. Also, the LVM relative mean dose was noted 12% higher than the LV relative mean dose due to smaller volume of the LVM (exclusion of blood pool). No significant differences were observed in the maximum relative mean dose between LV and LVM since the highest iso-dose lines seemed to pass the myocardium at all times.

Finally, there were a few limitations associated with this study including a relatively small sample size, uncertainty in registration errors, and lack of cardiac-gated cine images at inspiration breath-hold.

2.5. Conclusion

In lung cancer patients with tumors in the upper and middle lobes of the lung, cardiopulmonary motion can significantly affect the dose delivered to the LV/LVM (e.g., higher doses at expiration and diastole compared to lower doses at inspiration and systole). Notably, estimations of global cumulative LVM mean dose changed more than maximum dose when accounting for cardiopulmonary motion. Differences in estimated dose using the cine MR method compared to the original 50% 4D-CT were most evident using regional analysis, with those regions closest to the target of radiotherapy demonstrating significantly greater exposure than predicted by 50% 4D-CT. For this study, the highest doses were predicted in the anterobasal and anteroseptal-basal walls during diastole and expiration. We conclude that newer high resolution and cardiorespiratory-gated MR methods capable of quantifying regional cardiac radiation exposure and simultaneously accounting for cardiac and respiratory motion could provide improved insight and risk stratification for future patients undergoing thoracic radiotherapy, thereby improving both clinical care and mechanistic insight into the correlation of focal radiation dose and local physiologic response.

3 Spatiotemporal evolution of cardiac function before and after RT

3.1. Introduction

Myocardial function is clinically assessed using global metrics such as LVEF, and more recently GLS. However, RT-induced focal and/or subclinical cardiac damage may not acutely affect global metrics due to the ability of the heart to compensate for regional damage and to maintain its global function. This is shown by insignificant changes of LVEF and/or GLS at 3-24 months post-RT [66] and significant regional changes of MRI-derived metrics (e.g., segmental strain drop at 6 weeks post-RT) [67]. In addition, RT is a focal treatment and early or subclinical damages associated with local dose may not be captured by global metrics. For example, no relationship was found between the RT dose and LVEF drop in 80 Hodgkin lymphoma (HL) and non-HL (NHL) patients at 20 years following mediastinal RT with/without chemotherapy [68]. Similar studies have shown no relationship between GLS and radiation dose to the heart at 8.3 years following RT in 20 breast cancer patients who were treated by anthracycline-based chemotherapy and 3D conformal RT (3DCRT) [66]. Therefore, we hypothesized that the use of novel MR sequences (e.g., T1/T2 mapping, DENSE MRI, and LGE MRI) with high spatiotemporal resolution may improve the monitoring of possible structural, functional, and biological myocardial changes regionally over short follow ups so appropriate interventions could be applied before cardiovascular damage becomes irreversible [69].

A few studies have found a dose-dependent response between RT dose and MRI-based metrics. For instance, it was shown that RT dose is correlated with enhanced LGE signal in regions receiving greater than 30 Gy of radiation [52]. Similar results were noted for elevated ECV (>27.7%) in segmental regions receiving greater than 24 Gy [44]. In fact, a linear relationship was found between increase of dose (per Gy of radiation) and a 0.136%-point increase of ECV [44].

These findings emphasize the importance of using novel MRI sequences with regional quantification capabilities for future evaluation of RT-induced CVT.

In this study, cine GRE, DENSE, LGE, T1/T2 mapping, and ECV MRI were used to quantify functional, structural, and biological changes of cardiac muscle in patients with lung cancer globally and regionally at 3- and 6-months following RT completion compared to baseline before RT. In addition, the dose-dependency of the change in each metric and their behavior over different dose ranges were evaluated over 3- and 6-months follow-up.

The rest of this chapter will focus on the details of the employed cardiac MR sequences, outcomes of regional and global MRI-derived metrics, and the possible correlations between the RT dose and MRI-derived metrics.

3.2. Method

Patients: This study was approved by the Virginia Commonwealth University Institutional Review Board (IRB). Eight patients with lung cancer who were scheduled to receive RT with at least 5 Gray of radiation to at least 10% of the heart volume were recruited for this study.

MR image acquisition: Each patient provided informed consent prior to enrollment and underwent longitudinal MR imaging to assess the spatiotemporal evolution of regional biomechanical metrics that could indicate the development of CVT. These sessions occurred before the initial RT treatment (baseline), 3 months after completion of RT, and 6 months after completion of RT. All scans were performed on a 3T Siemens Vida scanner in the Pauley Heart Center Cardiovascular Imaging Suite at VCU Medical Center. The details of cardiac MRI sequences are listed below:

1. Cine MRI: LV volumes (left ventricular end systolic volume, left ventricular end diastolic volume, stroke volume, ejection fraction) were measured from GRE cine images from the cardiac

apex to its base (20° flip angle, 6mm slice thickness with 4mm slice gap, 8-10 ms TR, 3-5 ms TE). 25 cardiac phases were captured for each cine sequence including diastolic and systolic phases. The endocardium and epicardium were contoured semi-automatically using cvi42 (Version 5.10.1, Circle Cardiovascular Imaging; Calgary, Canada) software. Each contoured region was then manually refined by the user.

The same short-axis and long-axis cine images were used to track the myocardial tissue from systole to diastole and determine the peak global and regional strain (circumferential, radial, and longitudinal) values throughout a cardiac cycle using the feature-tracking algorithm within the cvi42 software. Regional strain values were reported for the 2D analysis and determined based on the AHA model.

2. T1/T2 mapping: A white blood T2-prepared single-shot balanced SSFP sequence was used to perform T2 mapping of the long axis (4 chamber view) and short axes (basal, mid and apical) at T2 preparation pulses of 0, 24 and 55 ms (70° flip angle, 6mm slice thickness, and acceleration factor of 2). At the same imaging planes, a modified Look Locker inversion recovery sequence (MOLLI) and cvi42 MyoMaps was used to perform T1 mapping (35° flip angle, 8 mm slice thickness, TE 1.1 ms, TR 2.2 ms, and acceleration factor of 2) [42], [43], [70]. A post-contrast T1 mapping sequence was run a few minutes following contrast administration (ProHance) at the same planes as pre-contrast T1 mapping to generate an ECV map. Segmentation of endocardium and epicardium was performed manually in cvi42 with a 10% margin to account for possible contouring errors. A 16-segment AHA model of T1/T2 maps was generated from the base, mid, and apex slices of the LV (by selection of dual right ventricle insertion points) to compare the regional T1/T2 values with other metrics and RT doses. All post-processing and regional quantification of T1 and T2 values were performed on cvi42. The ECV map was generated from

pre- and post-T1 signal of the myocardium along with pre- and post- T1 signal of the blood pool

and a fixed hematocrit level of 40% both globally and for every segment of the AHA model using

equation (1) [43].

$$ECV = (1 - hematocrit) * \frac{\left(\frac{1}{T1_{myo\ post}} - \frac{1}{T1_{myo\ pre}}\right)}{\left(\frac{1}{T1_{blood\ post}} - \frac{1}{T1_{blood\ pre}}\right)} \ (1)$$

3. Cardiac DENSE MRI: 2D spiral cine cardiac DENSE images were acquired throughout the

cardiac cycle at the same long-axis and short-axis slices of the left ventricle as above (TE 1.08 ms,

TR 15 ms, pixel size 1.6x1.6x8 mm, ω=0.10 cyc/mm, 1 signal average) [39], [40]. The magnitude

and phase data from the DENSE acquisition were processed using custom MATLAB code

provided by the Fred Epstein lab at University of Virginia that pioneered cardiac DENSE [40],

[71]. Peak strain values (longitudinal, radial, and circumferential) were calculated for each

segment of the AHA model. Segmentation of myocardium for strain analysis was performed semi-

automatically, followed by further manual refinement by the user, for all images acquired through

the cardiac cycle using a motion-guided segmentation algorithm within the custom MATLAB

code.

4. LGE MRI: LGE imaging was performed ~10 minutes following contrast administration

(ProHance) to allow adequate time for the uptake of the agent by injured tissues. 6-10 short axis

images of the LV were acquired from cardiac apex to its base using a phase-sensitive inversion

recovery (PSIR) GRE sequence with the following parameters: TE: 2.23 msc, TR: 834.4 msc, slice

thickness: 6 mm, ETL: 1, flip angle: 19º. The myocardium, its enhanced areas, and normal cardiac

muscles were manually contoured on cvi42. The percent of the enhanced area were calculated

globally and regionally (based on the 16-segment AHA model) by manual segmentation of enhanced areas using cvi42 package.

Each measured metric was recorded at baseline, 3-month post-RT, and 6-month post-RT completion. The changes of each metric at 3-months and 6-months follow-up were compared to baseline (i.e., the amount of each metric at 3-month and 6-months was subtracted from its baseline value (absolute changes)) globally and regionally. In addition, the percent change of each metric relative to the baseline value were also calculated (e.g., ((T1 at 3-months) – (T1 at baseline))/ (T1 at baseline) *100)) globally and regionally.

Statistics: For each metric including LVEF, T1 signal, T2 signal, longitudinal/circumferential/radial strain, ECV, and enhanced volume from LGE MRI, the absolute and relative global and regional changes at 3-months and 6-months follow-up were compared to baseline using a Student's t-test. Changes of each metric were also evaluated based on 6 different dose ranges, 0-10 Gy, 10-20 Gy, 20-30 Gy, 30-40 Gy, 40-50 Gy, and >50 Gy, to see if the changes are significant among different dose intervals at 3-months and 6-months follow-up using unequal ANOVA along with Tukey HSD test. Correlation of maximum radiation dose and absolute/relative changes of each metric were evaluated at 3-months and 6-months follow-up using Pearson's correlation. Lastly, the correlations between each pair of metrics (e.g., T1 signal and T2 signal) were quantified at 3-months and 6-months follow-up using Pearson's correlation. It should also be noted that the normality of assumption and skewness from the normal quantile plot were evaluated for each dataset to check heteroskedasticity of data. For non-normal data distribution, Kruskal-Wallis test, Wilcoxon Signed-Rank test and Spearman rank correlation tests were done instead of Student's t-test, ANOVA and Pearson's correlation, respectively. All statistical tests were run based on significance level of p≤0.05 using JMP software.

3.3. Results

Acquired data were analyzed based on the above approach. A summary of global and regional

sample sizes obtained from imaging tests at 3-months and 6-months follow-up is shown in Table

3.1.

Table 3.1 Summary of regional and global sample sizes at 3-months and 6-months follow-up.

	Global		Regional	
	3-months	6-months	3-months	6-months
LVEF	8	8	-	-
T1 mapping	7	7	112	112
ECV	2	3	32	48
T2 mapping	7	7	112	112
Radial strain	7	7	112	112
Circumferential strain	7	7	112	112
Longitudinal strain	7	7	112	112
LGE	4	4	64	64

3.3.1 Global metrics

Global measurements including LVEF, global T1, global ECV, and global longitudinal, radial, and

circumferential strain did not show significant differences at either 3-months (P>0.3) or 6-months

(P>0.06) follow-up. However, absolute and relative global T2 changes at 3-months post-RT

(absolute changes: 1.2 ± 1.2 ms P=0.048, relative changes: 2.8 ± 2.8 % P=0.048) and absolute

increase of global enhanced area from LGE MRI at 6-months (5.7 ± 3.7 % vs 10 ± 2.7 %, P=0.0356)

post-RT demonstrated significant changes. No significant changes were noted in global T2

changes at 6-months (P>0.49) or enhanced area increase at 3-months (P>0.3) following RT

completion. Table 3.2 summarizes the absolute and relative global measurements changes over 3-

months and 6-months follow ups (Raw data is provided in the supplement (Table 6.1)). Table 3.3

contains all the P-values from the T-test measurements between different time points. Figure 3.1-

3.4 shows the bar graphs of the global metrics at baseline and each follow-up.

Table 3.2. Summary of absolute and relative global metrics changes at 3-months (t2) and 6-months (t3) compared to baseline (t1).

Global Metrics	t2-t1 (absolute)		t2-t1 % (relative)		t3-t1 (absolute)		t3-t1 % (relative)	
	Mean	SD	Mean	SD	Mean	SD	Mean	SD
LVEF	0.4%	4.3%	1.4	8.1	-0.3%	2.5%	-0.4	4.1
T1	14.3 ms	35.8 ms	1.2	2.9	7.8 ms	82.3 ms	0.7	6.3
T2	1.2 ms	1.2 ms	2.8	2.8	1.3 ms	4.7 ms	3.5	10.6
ECV	0.1	0.2	31.7	57.5	0.0	0.1	1.5	18.4
Radial Strain	0.5	5.3	6.4	20.8	-1.4	4.3	-1.0	12.7
Circumferential Strain	-0.4	2.4	4.6	15.9	0.0	2.0	1.2	11.0
Longitudinal Strain	-0.2	2.5	4.0	16.6	1.7	2.1	-10.0	14.5
Enhanced volume	2.3%	3.1%	31.7	48.4	5.4%	3.7%	5668.4	9686.1

Table 3.3. Summary of p-values from the statistical analysis for evaluation of absolute and relative global measurement changes at 3-months ((t2-t1) and (t2-t1) relative) and 6-months ((t3-t1) and (t3-t1) relative) follow ups.

Global Metrics	t2-t1	t2-t1 (relative)	t3-t1	t3-t1 (relative)
LVEF	0.8	0.68	0.78	0.85
T1	0.375	0.375	1	1
T2	**0.048**	**0.048**	0.55	0.49
ECV	0.67	0.67	0.97	0.91
Radial Strain	0.82	0.48	0.5	0.87
Circumferential Strain	0.71	0.5	0.97	0.81
Longitudinal Strain	0.84	0.57	0.18	0.21
Enhanced volume	0.3	0.33	**0.0356**	0.06
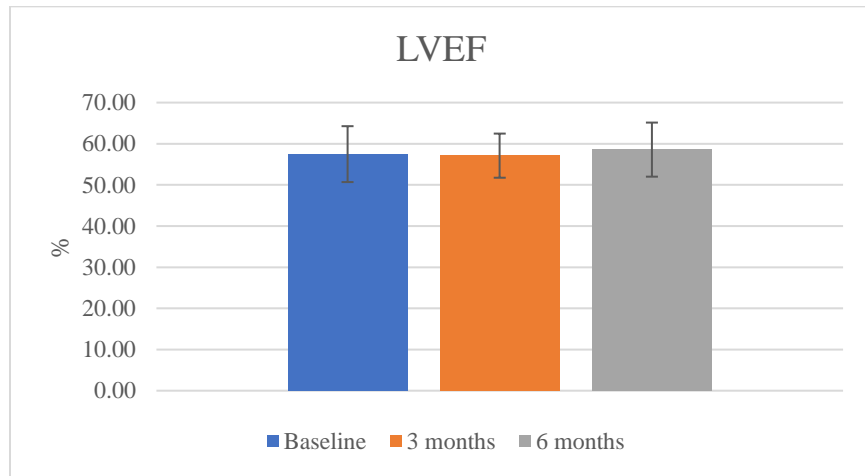
Figure 3.1. LVEF values (±SD) at baseline and 3-months and 6-month follow-up.
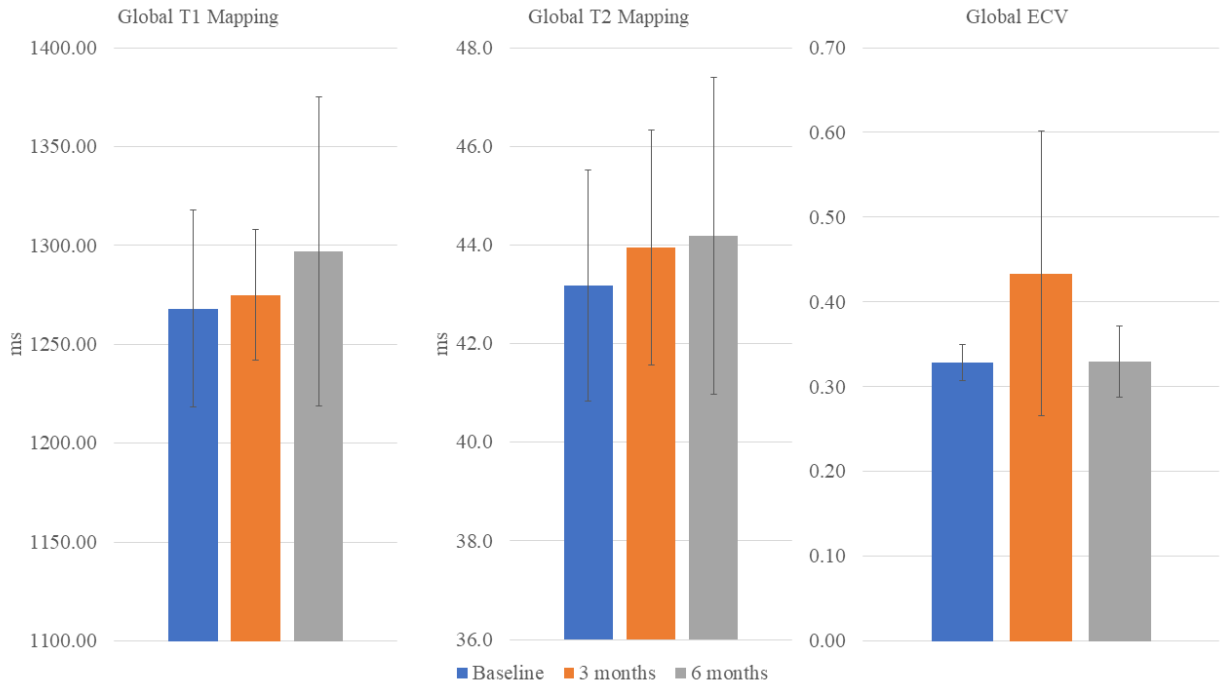
Figure3.2. Global T1, T2, and ECV signal values (±SD) at baseline and 3-months and 6-month follow-up.
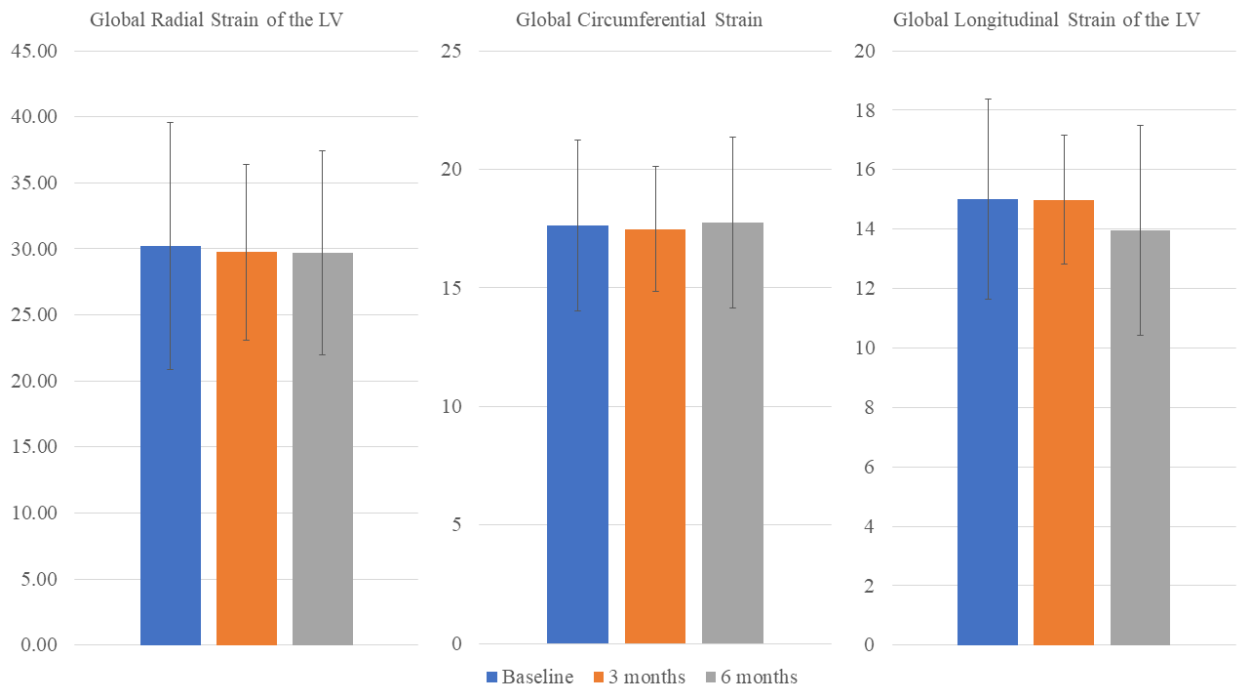
Figure3.3. Global radial, circumferential and longitudinal strain values (±SD) at baseline and 3-months and 6-month follow-up.
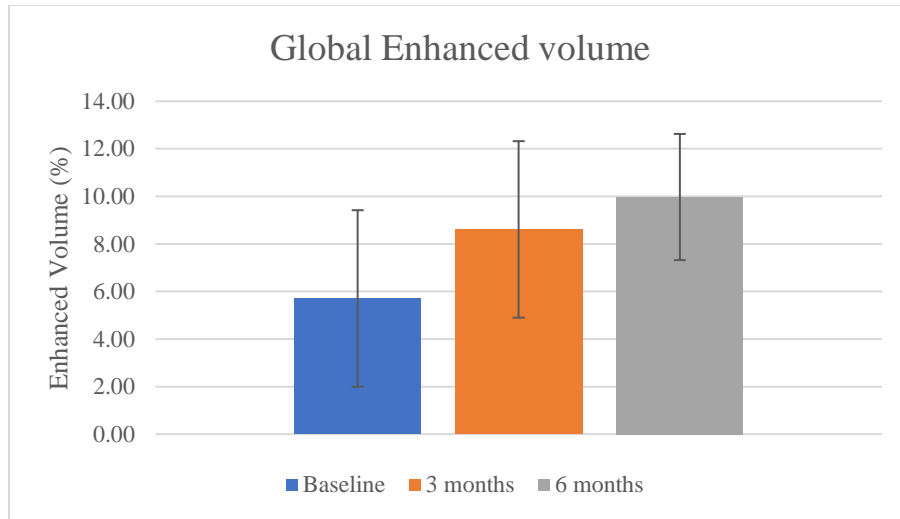
Figure3.4. Global enhanced volume values (±SD) at baseline and 3-months and 6-month follow-up.

3.3.2. Regional metrics

T1 mapping: Unlike global measurements, relative and absolute regional T1 values demonstrated significant differences at 3-months post-RT completion, and the differences were noted at anterior regions of the LV where radiation dose was higher (Segment 2: absolute T1 change of 26.7±30.6 ms (P=0.038) and relative T1 changes of 2.2±2.5 % (P=0.038) and Segment 6: absolute T1 change of 60.4±74.1 ms (P=0.046) and relative T1 changes of 5.1±6.4% (P=0.048)). Increase of T1 signal has been shown to indicate signs of diffuse myocardial fibrosis and inflammation. No significant differences (absolute or relative) were noted at 6-month over all 16 segments of the AHA model (P>0.28). Table 3.4 shows the regional absolute and relative changes of T1 signal based on the AHA model at 3-months and 6-months follow up compared to baseline (raw data is provided in the supplement in Table 6.2). Table 3.5 shows the P-values associated with statistical measurements on regional T1 signal values based on the AHA model. Figures 3.5 shows the absolute and relative regional T1 changes graphically.

64

Table 3.4. Absolute and relative regional T1 signal changes at 3-months (t2) and 6-months (t3) compared to baseline (t1).

AHA segment	t2-t1 ms (absolute)		t2-t1 % (relative)		t3-t1 ms (absolute)		t3-t1 % (relative)	
	Mean	SD	Mean	SD	Mean	SD	Mean	SD
1	50.4	68.3	4.3	5.9	45.0	120.0	3.8	9.8
2	26.7	30.6	2.2	2.5	16.6	75.3	1.3	5.6
3	8.5	27.0	0.7	2.2	-12.0	50.6	-0.8	3.8
4	19.0	48.5	1.6	4.1	-7.4	51.7	-0.5	3.9
5	-6.6	32.5	-0.6	2.6	6.5	44.2	0.5	3.4
6	60.4	74.1	5.1	6.4	25.1	71.4	2.0	5.7
7	23.1	65.7	2.1	5.5	23.1	124.2	2.1	10.2
8	20.9	31.3	1.6	2.4	2.4	59.0	0.2	4.4
9	-1.0	21.5	-0.1	1.7	-28.9	53.5	-2.2	4.1
10	20.7	53.4	1.9	4.7	-10.0	64.8	-0.7	4.9
11	5.6	46.1	0.7	4.1	-20.0	77.3	-1.4	6.0
12	31.5	68.7	2.8	5.8	20.4	125.4	1.9	10.3
13	-9.1	67.9	-0.5	5.3	25.2	92.5	1.8	6.9
14	36.2	107.4	2.7	8.0	-36.4	84.0	-2.6	6.1
15	0.3	67.5	0.2	5.1	-25.5	86.2	-1.7	6.5
16	4.4	118.1	1.0	9.0	-33.4	109.7	-2.2	8.0

Table3.5. P-values associated with statistical analysis on absolute and relative regional T1 signal changes at 3-months (t2) and 6-months (t3) compared to baseline (t1)

AHA segment	t2-t1 (absolute)	t2-t1 (relative)	t3-t1 (absolute)	t3-t1 (relative)
1	0.156	0.156	0.5625	0.5625
2	**0.0381**	**0.038**	0.64	0.63
3	0.46	0.46	0.61	0.63
4	0.46	0.46	0.76	0.78
5	0.68	0.57	0.75	0.77
6	**0.046**	**0.048**	0.46	0.46
7	0.42	0.38	0.69	0.66
8	0.15	0.15	0.93	0.93
9	0.9	0.94	0.28	0.28
10	0.35	0.35	0.74	0.76
11	0.77	0.67	0.58	0.61
12	0.3	0.27	0.73	0.69
13	0.75	0.81	0.56	0.58
14	0.44	0.43	0.37	0.38
15	0.99	0.93	0.58	0.58
16	0.92	0.78	0.52	0.56
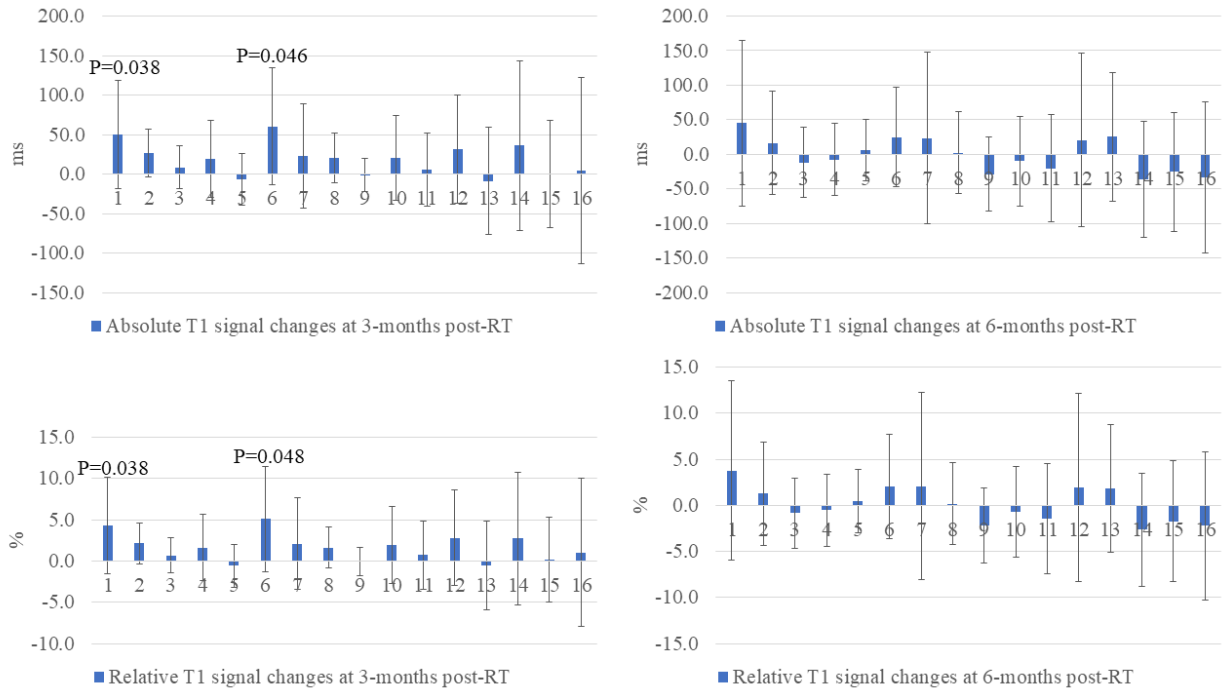
Figure3.5. Absolute and relative T1 signal changes (±SD) at 3-months and 6-months following RT compared to baseline.

Comparison of significant T1 signal changes (both absolute and relative) over various dose ranges demonstrated that changes of T1 signal at regions receiving doses greater than 50 Gy is significantly higher than regions receiving 0-10 Gy at 3-months following RT (absolute: 48.8±47.5 ms vs 10.2±71.3 ms, P= 0.0219; relative: 3.9±3.9% vs 1.0±5.6%, P=0.0277). Similar results were noted at 6-months follow-up except that T1 signal changes (both absolute and relative) were significantly higher between >50 Gy and 0-10, 10-20, 20-30, 30-40, and 40-50 Gy (P<0.0142), and between 40-50 Gy and 0-10 Gy (P<0.0107). Table 3.6 lists the absolute and relative T1 changes over various dose ranges at 3-months and 6-months follow-up. Tables 3.7-3.9 are a summary of P-values from the statistical analysis between absolute/relative changes of T1 signal at 3-months and 6-months follow-up. Figures 3.6 shows the absolute and relative changes of T1 signal over various dose ranges graphically.

Table3.6. Absolute and relative changes of T1 signal over various dose ranges.

Dose range (Gy)	t2-t1 ms (absolute)		t2-t1 % (relative)		t3-t1 ms (absolute)		t3-t1 % (relative)	
	Mean	SD	Mean	SD	Mean	SD	Mean	SD
0-10	10.2	71.3	1.0	5.6	-40.2	65.5	-3.0	4.7
10-20	8.9	53.7	0.9	4.6	-4.2	79.7	-0.4	6.0
20-30	19.7	59.4	1.75	5.1	14.6	51.3	1.2	3.9
30-40	33.7	80.5	2.3	6.9	7.8	42.6	0.6	3.3
40-50	22.9	63.6	2.0	5.5	13.8	41.8	1.2	3.3
>50	48.8	47.5	3.9	3.9	130.1	98.5	10.4	8.2

Table3.7. Summary of statistical analysis between the absolute changes of T1 signal over various dose ranges at 3-months follow-up.

Dose range (Gy)	0-10	10-20	20-30	30-40	40-50
10-20	0.8091				
20-30	0.9918	0.8708			
30-40	0.5406	0.4379	0.9530		
40-50	0.7708	0.6251	0.6514	0.7363	
>50	**0.0219**	0.057	0.2317	0.2193	0.1423

Table3.8. Summary of statistical analysis between the relative changes of T1 signal over various dose ranges at 3-months follow-up.

Dose range (Gy)	0-10	10-20	20-30	30-40	40-50
10-20	0.7850				
20-30	0.9918	0.8708			
30-40	0.5406	0.4379	0.7683		
40-50	0.7439	0.5636	0.6514	0.7363	
>50	**0.0277**	0.057	0.2011	0.2703	0.1423

Table3.9. Summary of statistical analysis between the absolute changes of T1 signal over various dose ranges at 6-months follow-up.

Dose range (Gy)	0-10	10-20	20-30	30-40	40-50
10-20	0.1641				
20-30	0.1015	0.3703			
30-40	0.0625	0.5828	0.8710		
40-50	**0.0107**	0.3311	0.7453	0.6093	
>50	**0.0001**	**0.0026**	**0.0142**	**0.0081**	**0.0065**

Table3.10. Summary of statistical analysis between the relative changes of T1 signal over various dose ranges at 6-months follow up.

Dose range (Gy)	0-10	10-20	20-30	30-40	40-50
10-20	0.1749				
20-30	0.1015	0.3166			
30-40	0.0593	0.5828	1.0		
40-50	**0.0099**	0.3311	0.8710	06093	
>50	**0.0001**	**0.0026**	**0.0142**	**0.0081**	**0.0065**
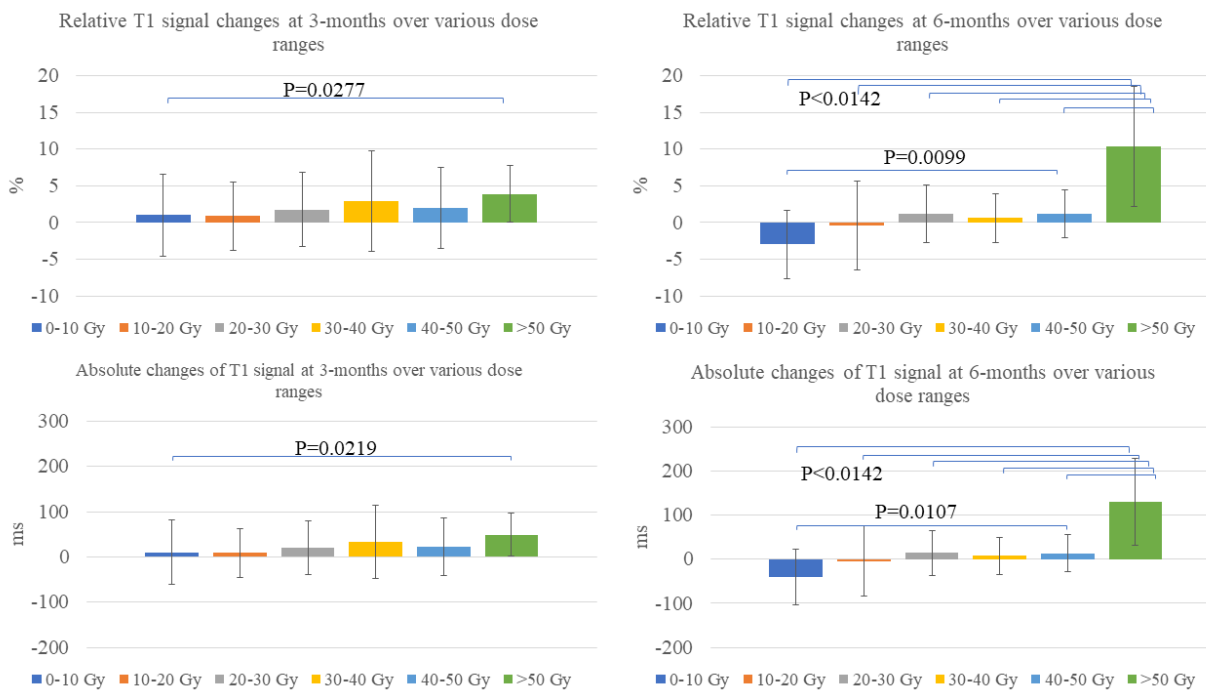
Figure3.6. Absolute and relative changes of T1 signal at 3-months and 6-months post-RT compared to baseline over various dose ranges.

Correlation between T1 signal changes and the radiation dose were noted at both 3-months (absolute: P=0.0109, relative: P=0.0257)) and 6-months (absolute: P=0.0001, relative: P=0.0001) follow-up with a stronger correlation at 6-months follow-up. Figure 3.7 shows the correlation

between the maximum radiation dose and absolute/relative T1 signal changes at 3-months and 6-months follow-up.
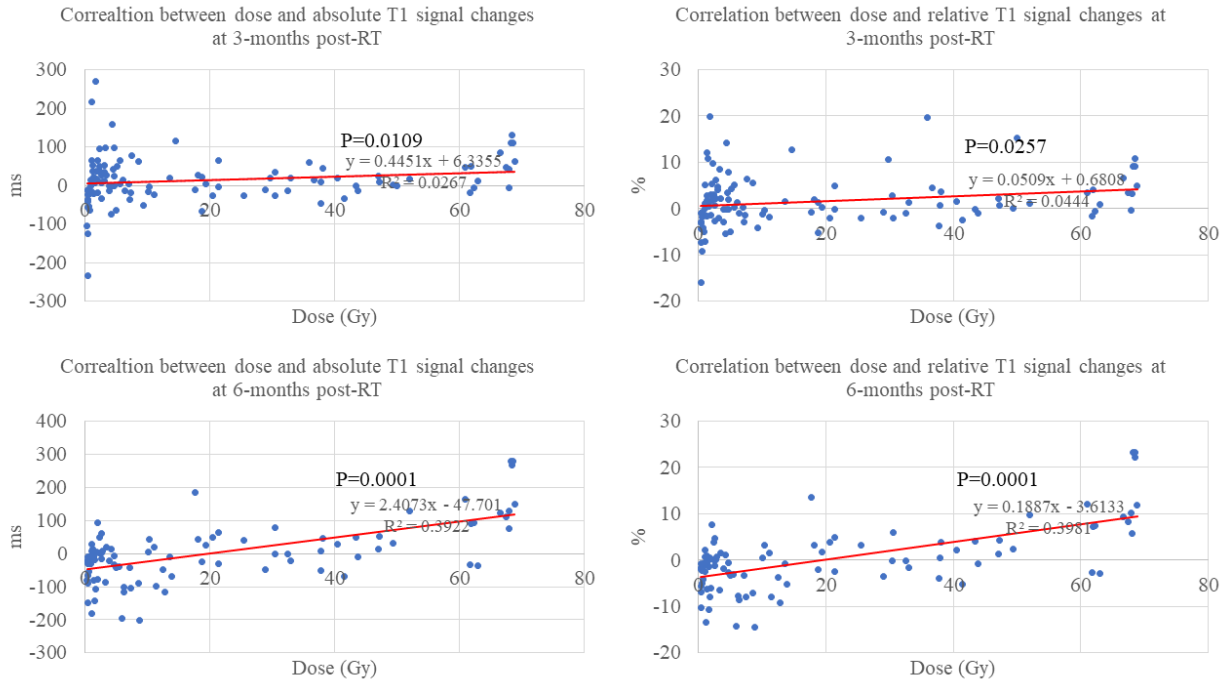
Figure3.7 Correlation between the dose and absolute/relative T1 signal changes at 3-months and 6-months follow up.

ECV: Similar to global ECV measurements, regional ECV values also did not show any significant differences at 3- or 6-months follow-up (P>0.25). Table 3.11 shows the regional absolute and relative changes of ECV based on the AHA model at 3-months and 6-months follow-up compared to baseline (raw data is provided in the supplement in Table 6.3). Table 3.12 shows the P-values associated with statistical measurements on regional ECV changes based on the AHA model. Figures 3.8 shows the evolution of ECV changes over time.

Table3.11. Absolute and relative regional ECV changes (±SD) based on AHA model at 3-months (t2) and 6-months (t3) compared to baseline (t1).

AHA segment	t2-t1 (absolute)		t2-t1 % (relative)		t3-t1 (absolute)		t3-t1 % (relative)	
	Mean	SD	Mean	SD	Mean	SD	Mean	SD
1	0.1	0.2	28.4	53.2	0.04	0.09	13.0	27.8
2	0.1	0.2	26.1	59.4	0.01	0.09	6.0	26.0
3	0.1	0.2	34.8	60.1	-0.01	0.05	-2.5	15.8
4	0.1	0.2	30.7	53.9	-0.02	0.07	-5.0	18.5
5	0.1	0.2	23.8	52.0	-0.03	0.05	-8.1	14.5
6	0.1	0.2	46.3	71.3	0.02	0.07	7.4	20.3
7	0.1	0.2	31.6	55.4	0.02	0.06	5.9	18.4
8	0.1	0.2	32.1	60.8	0.00	0.06	1.6	18.2
9	0.1	0.2	30.0	56.1	-0.01	0.06	-1.4	18.5
10	0.1	0.2	24.3	49.8	-0.03	0.06	-7.1	16.7
11	0.1	0.2	33.8	61.8	-0.03	0.03	-8.8	9.8
12	0.1	0.2	38.1	53.7	0.02	0.04	6.5	11.8
13	0.1	0.2	28.4	50.7	-0.01	0.05	-3.0	13.6
14	0.1	0.2	30.3	56.6	-0.01	0.06	-3.0	16.0
15	0.1	0.2	30.0	62.1	-0.03	0.11	-4.4	30.4
16	0.1	0.2	36.4	61.9	-0.01	0.07	0.2	21.6

Table3.12. P-values associated with statistical analysis on absolute and relative regional ECV changes at 3-months (t2) and 6-months (t3) compared to baseline (t1).

AHA segment	t2-t1	t2-t1 (relative)	t3-t1	t3-t1 (relative)
1	0.72	0.68	0.61	0.57
2	0.73	0.73	0.77	0.77
3	0.67	0.66	0.8	0.84
4	0.71	0.67	0.69	0.74
5	0.76	0.72	0.51	0.51
6	0.66	0.63	0.68	0.65
7	0.68	0.66	0.71	0.69
8	0.71	0.69	0.97	0.91
9	0.69	0.68	0.88	0.92
10	0.73	0.71	0.57	0.6
11	0.68	0.68	0.33	0.33
12	0.61	0.6	0.53	0.51
13	0.67	0.67	0.78	0.75
14	0.68	0.25	0.81	0.81
15	0.76	0.71	0.72	0.85
16	0.66	0.66	0.9	0.98
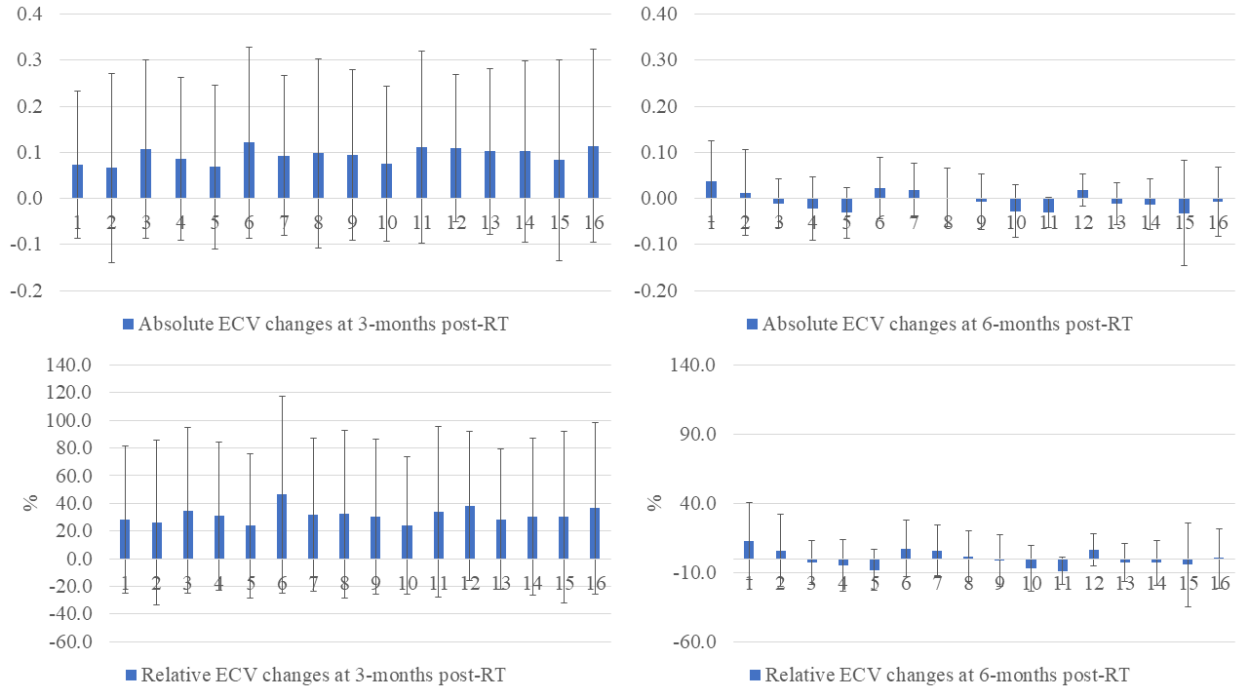
Figure3.8. Absolute and relative ECV changes at 3-months and 6-months following RT compared to baseline.

Due to data limitations on ECV analysis (3 or less samples), we only report the global and regional changes of ECV.

T2 mapping: Regional T2 signal changes demonstrated higher values over 3-months follow-up at multiple segments of AHA model (segment 1, 4, 5, 6, 7, 12, and 14) (P<0.048). It has been shown that T2 increase is related to myocardial edema. No significant changes of T2 signal were noted at 6-months follow up (P>0.067). Table 3.13 shows the absolute and relative regional T2 signal changes at multiple time points (raw data is provided in the supplement (Table 6.4)). Table 3.14 has all the P-values from statistical analysis of T2 signal changes (both absolute and relative) over 3-months and 6-months follow-up. Figure 3.9 shows the evolution of T2 signal changes over time.

Table3.13. Absolute and relative regional T2 signal changes (±SD) based on AHA model at 3-months (t2) and 6-months (t3) compared to baseline (t1).

AHA segment	t2-t1 ms (absolute)		t2-t1 % (relative)		t3-t1 ms (absolute)		t3-t1 % (relative)	
	Mean	SD	Mean	SD	Mean	SD	Mean	SD
1	1.7	2.0	4.4	5.0	4.7	6.1	11.8	14.8
2	0.6	1.8	1.4	4.4	1.0	3.7	2.7	8.8
3	1.0	1.6	2.5	3.8	0.4	3.5	1.3	8.1
4	2.0	1.5	4.9	3.7	1.6	4.3	4.4	10.5
5	1.6	2.0	3.8	4.7	1.7	4.8	4.8	11.7
6	2.0	2.4	5.0	6.0	3.1	5.9	8.2	14.6
7	1.8	1.5	4.2	3.6	1.7	5.6	4.4	13.0
8	0.5	1.6	1.4	3.7	0.7	4.1	2.1	9.2
9	0.6	0.9	1.5	2.1	0.7	3.8	2.1	8.8
10	0.8	2.0	2.0	4.7	1.0	3.0	2.5	7.5
11	1.0	2.2	2.2	4.9	1.8	4.9	4.8	11.5
12	2.5	2.9	6.3	7.7	2.4	7.6	6.7	18.1
13	-0.9	2.6	-1.9	5.3	-0.9	5.0	-1.6	10.7
14	1.3	1.5	3.1	3.3	-1.5	6.1	-2.0	12.6
15	-0.8	3.7	-0.9	7.4	0.4	4.8	1.6	10.6
16	2.6	8.0	6.2	17.8	2.1	7.4	5.4	16.3

Table3.14. P-values associated with statistical analysis on absolute and relative regional T2 signal value changes at 3-months (t2) and 6-months (t3) compared to baseline (t1).

AHA segment	t2-t1 (absolute)	t2-t1 (relative)	t3-t1 (absolute)	t3-t1 (relative)
1	**0.038**	**0.037**	0.073	0.067
2	0.47	0.44	0.57	0.52
3	0.16	0.16	0.79	0.73
4	**0.0185**	**0.0185**	0.22	0.19
5	**0.048**	**0.045**	0.23	0.2
6	**0.046**	**0.042**	0.14	0.13
7	**0.028**	**0.027**	0.27	0.24
8	0.46	0.4	0.72	0.63
9	0.065	0.066	0.34	0.3
10	0.36	0.33	0.51	0.48
11	0.32	0.3	0.44	0.39
12	**0.042**	**0.044**	0.25	0.22
13	0.79	0.79	0.64	0.62
14	**0.045**	**0.031**	0.69	0.63
15	0.69	0.77	0.86	0.74
16	0.61	0.77	0.86	0.74
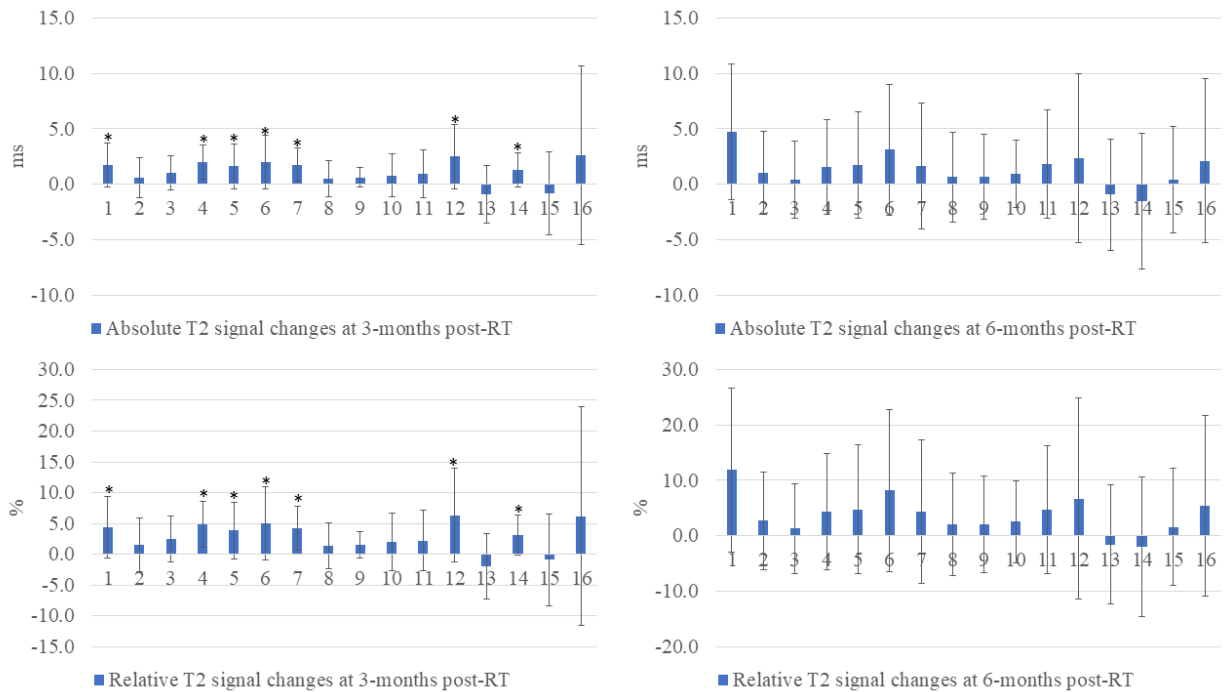
Figure3.9. Absolute and relative T2 signal changes at 3-months and 6-months following RT compared to baseline. Star sign indicates significant differences (P<0.05).

Comparison of T2 signal changes over multiple dose ranges showed significant changes of T2 signal between areas receiving >50 Gy versus 0-10 Gy (P<0.0001), >50 Gy versus 10-20 Gy (P<0.0001), 40-50 Gy versus 0-10 Gy (P<0.0131), and 40-50 Gy versus 10-20 Gy (P<0.0157) at 6-months follow up. However, no significant differences were note between changes of T2 signal over different dose ranges at 3-months follow-up (P>0.7507). Table 3.15 lists the changes of T2 signal over various dose ranges at 3-months and 6-months follow-up. Tables 3.16-3.17 are a summary of P-values from statistical analysis between absolute/relative changes of T2 signal at 6-months follow-up. Figures 3.10 shows the absolute and relative changes of T2 signal over various dose ranges.

Table3.15. Absolute and relative changes of T2 signal over various dose ranges.

Dose range (Gy)	t2-t1 ms (absolute)		t2-t1 % (relative)		t3-t1 ms (absolute)		t3-t1 % (relative)	
	Mean	SD	Mean	SD	Mean	SD	Mean	SD
0-10	1.1	3.4	2.7	7.4	-0.6	5.1	-0.6	11.6
10-20	0.3	2.5	1.0	5.3	-1.6	4.4	-3.4	9.8
20-30	1.3	2.6	3.2	6.0	2.1	0.5	4.9	1.3
30-40	1.7	3.4	4.4	8.4	3.4	1.7	8.5	4.4
40-50	1.6	1.2	4.2	3.1	5.5	2.9	14.1	7.8
>50	1.2	3.0	3.3	7.1	7.4	4.4	17.5	10.9

Table3.16. Summary of statistical analysis between the absolute changes of T2 signal over various dose ranges at 6-months follow up.

Dose range (Gy)	0-10	10-20	20-30	30-40	40-50
10-20	0.6483				
20-30	0.7988	0.6483			
30-40	0.2302	0.1845	0.9951		
40-50	**0.0131**	**0.0157**	0.777	0.9540	
>50	**0.0001**	**0.0001**	0.2249	0.4254	0.9515

Table3.17. Summary of statistical analysis between the relative changes of T2 signal over various dose ranges at 6-months follow up.

Dose range (Gy)	0-10	10-20	20-30	30-40	40-50
10-20	0.9657				
20-30	0.8681	0.6780			
30-40	0.2653	0.1754	0.9918		
40-50	**0.0091**	**0.0089**	0.6606	0.9136	
>50	**0.0001**	**0.0001**	0.2002	0.4328	0.9820
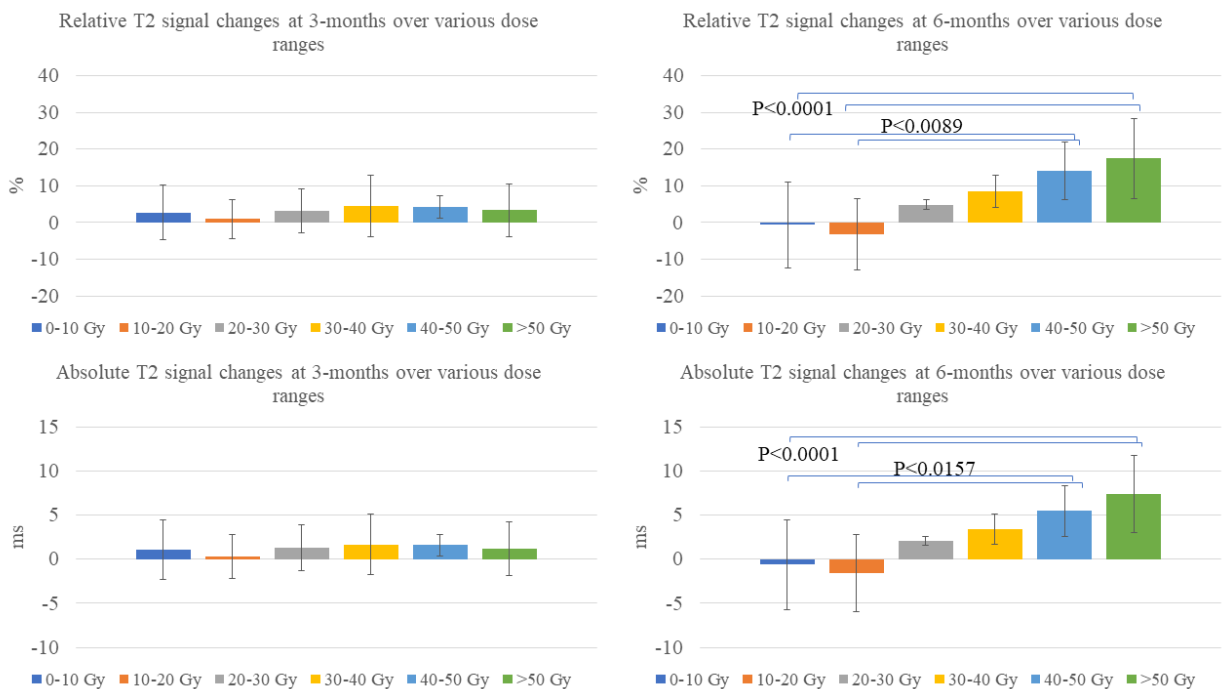
Figure3.10. Absolute and relative changes of T2 at 3-months and 6-months post-RT compared to baseline over various dose ranges.

As shown in figures 3.11, positive correlation of T2 changes and maximum dose was noted at both 3-months and 6-months follow up with stronger correlation at 6-months.
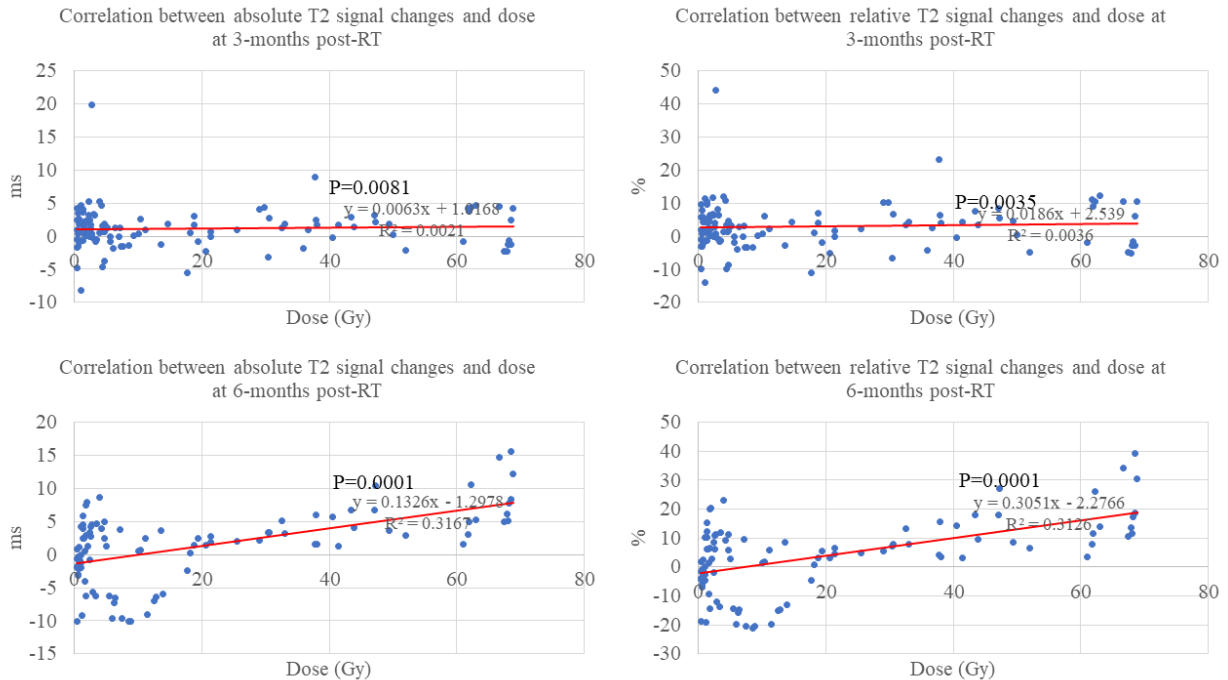
Figure3.11. Correlation between the dose and absolute/relative T2 signal changes at 3-months and 6-months follow up.

Radial strain: Absolute and relative regional changes of radial strain were noted at segment 2 (absolute: -4.5±4.9 P=0.032, relative: -23.0±20.8 % P=0.0176) at 3-months and segments 1 (absolute: -11.2±7.9 % P=0.026, relative: -25.5±17.6 P=0.023) and 12 (absolute: -13.7±21.7 P=0.0084, relative: -32.8±32.1 % P=0.035) at 6-month follow-up. Notably, segments 1, 2, and 12 are all anterior regions of the LV where radiation doses were higher. Reduction in strain demonstrates decrease of the contractibility function. Table 3.18 shows the absolute and relative regional radial strain changes at 3-months and 6-months (raw data is provided in the supplement in Table 6.5). Table 3.19 has all the P-values from statistical analysis of regional radial strain

changes (both absolute and relative) over 3-months and 6-months follow up. Figures 3.12 shows the evolution of regional radial strain changes over time.

Table3.18. Absolute and relative regional radial strain changes (±SD) based on AHA model at 3-months (t2) and 6-months (t3) compared to baseline (t1).

AHA segment	t2-t1		t2-t1 % (relative)		t3-t1		t3-t1 % (relative)	
	Mean	SD	Mean	SD	Mean	SD	Mean	SD
1	-3.3	17.5	14.9	60.2	-11.2	7.9	-25.5	17.6
2	-4.5	4.9	-23.0	20.8	-3.7	9.3	-1.2	42.4
3	-1.9	3.9	-8.5	13.1	-1.4	8.2	6.6	37.6
4	-5.2	7.2	-12.5	23.8	2.1	18.5	1.2	54.8
5	3.1	12.6	46.3	87.2	5.3	14.5	36.7	55.4
6	4.9	21.3	33.7	58.1	8.4	21.4	37.5	55.6
7	0.6	9.9	1.0	24.2	-3.1	23.3	-8.7	50.0
8	5.0	12.1	14.8	33.1	2.6	11.9	12.0	37.0
9	1.2	6.4	9.6	29.7	-7.2	10.5	-9.5	37.1
10	-1.7	7.0	4.5	40.1	-4.0	10.1	3.6	61.0
11	2.5	11.4	29.3	66.9	-0.4	8.2	8.2	30.2
12	-1.8	14.1	3.7	41.2	-13.7	21.7	-32.8	32.1
13	9.9	14.1	26.0	30.4	-7.9	11.9	-9.1	33.4
14	8.2	11.2	19.0	24.8	-8.0	12.5	-8.7	32.1
15	5.9	15.8	20.9	30.9	-16.1	28.7	-17.5	34.4
16	3.7	16.1	18.7	53.2	-20.7	27.6	-27.6	38.5

Table3.19. P-values associated with statistical analysis on absolute and relative regional radial strain value changes at 3-months (t2) and 6-months (t3) compared to baseline (t1).

AHA segment	t2-t1	t2-t1 (relative)	t3-t1	t3-t1 (relative)
1	0.66	0.56	**0.026**	**0.023**
2	**0.032**	**0.0176**	0.21	0.47
3	0.28	0.16	0.72	0.7
4	0.12	0.24	0.25	0.96
5	0.56	0.24	0.45	0.19
6	0.59	0.2	0.41	0.19
7	0.88	0.92	0.77	0.71
8	0.34	0.31	0.5	0.5
9	0.66	0.46	0.18	0.59
10	0.58	0.79	0.41	0.9
11	0.61	0.32	0.92	0.57
12	0.76	0.83	**0.0084**	**0.035**
13	0.13	0.055	0.14	0.56
14	0.06	0.055	0.1	0.28
15	0.39	0.149	0.13	0.15
16	0.29	0.42	0.15	0.17
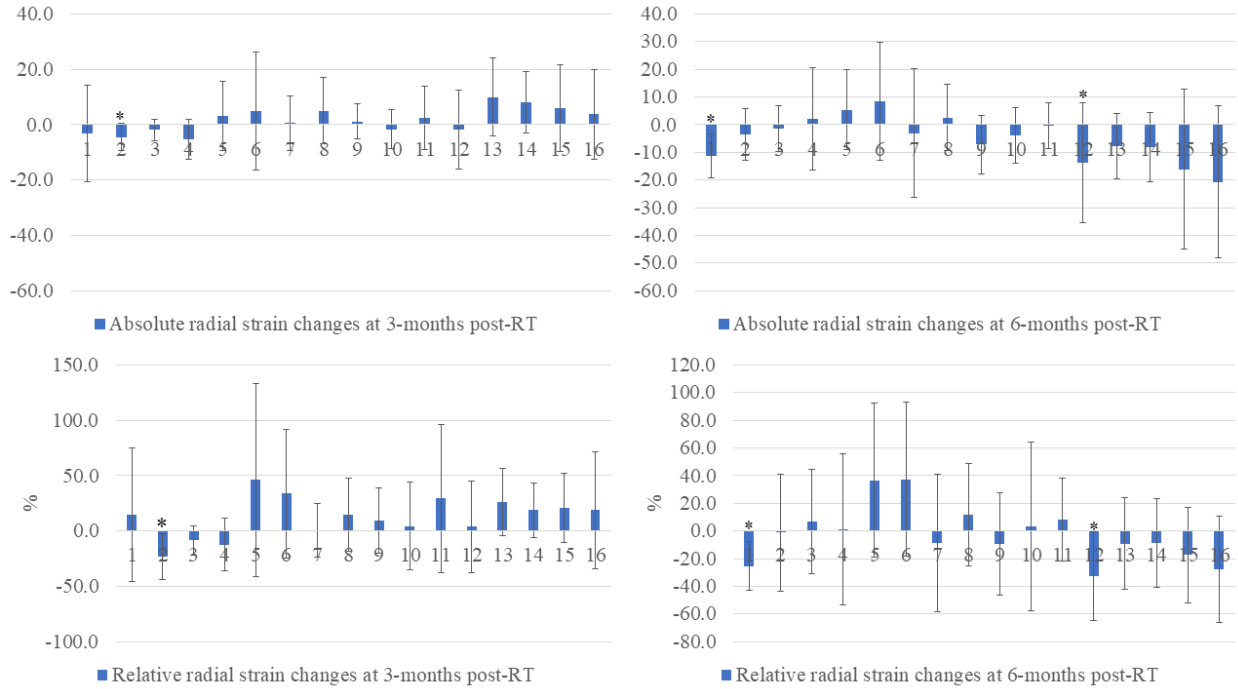
Figure3.12. Absolute and relative radial strain changes at 3-months and 6-months following RT compared to baseline. Star sign indicates significant differences (P<0.05).

Comparison of radial strain changes over various doses did not show any significant differences at 3-months (P>0.11) or 6-months post-RT (P>0.15). Also, no correlation was found between radial strain at 3-months (P>0.88) or 6-months (P>0.73) follow-up and the radiation dose. Figure 3.13 shows the radials strain changes over various dose ranges at 3-months and 6-months. Figure 3.14 shows the correlation between radial strain changes and dose at 3-months and 6-months follow-up.
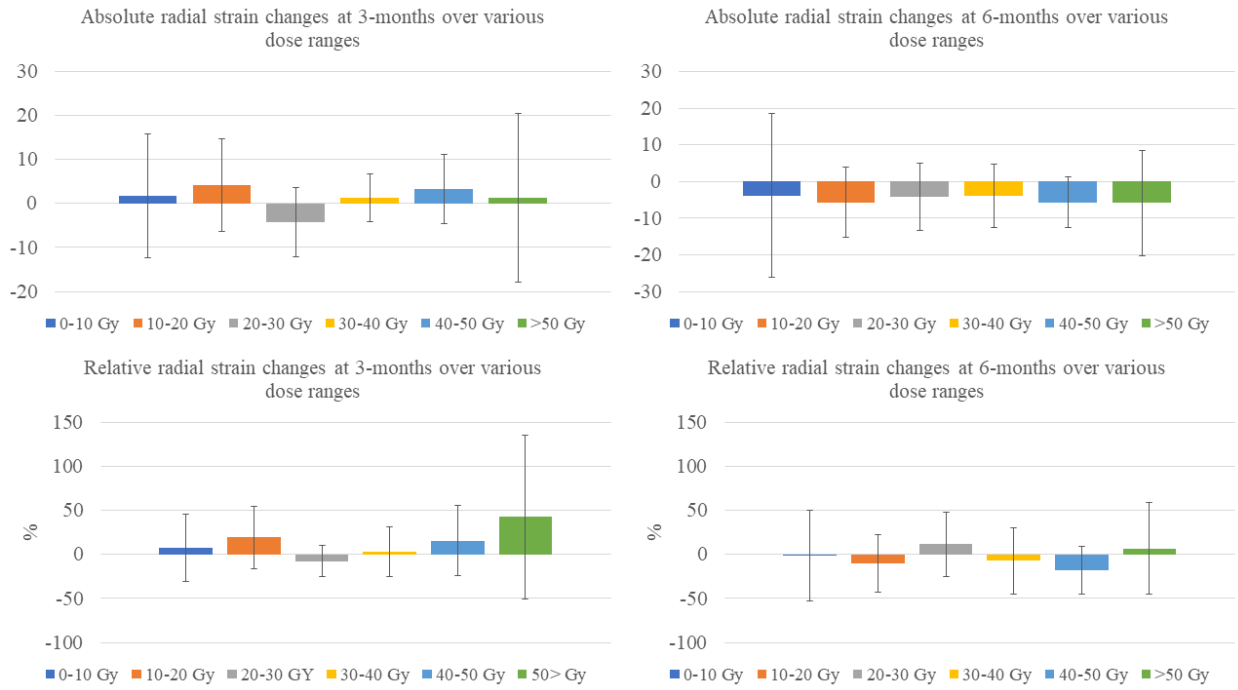
Figure3.13. Absolute and relative changes of radial strain at 3-months and 6-months post-RT compared to baseline over various dose ranges.
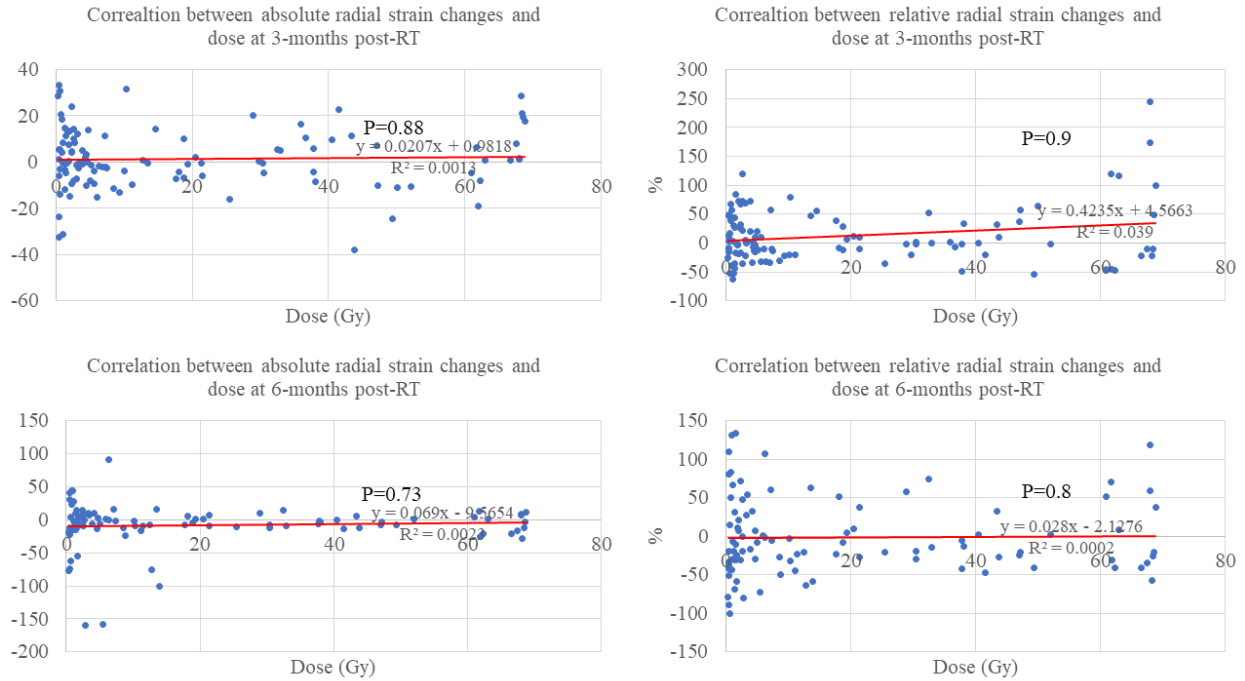
Figure3.14. Correlation between the dose and absolute/relative radial strain changes at 3-months and 6-months follow up.

Circumferential strain: Similar to radial strain, significant changes of circumferential strain values were noted at 3-months (segment 2 (absolute: 3.9±4.4 P=0.0156, relative: -41.4±62.6 % P=0.0156) and segment 3 (absolute: 7.7±10 P=0.0391, relative: -70.1±96.5 % P=0.0469)) and 6-months (segment 1 (absolute: 2.8±3.0 P=0.046, relative: -13.4±13.8 % P= 0.04) and segment 12 (absolute: 2.5±1 P=0.0024, relative: -15.5±9.1 % P=0.0123) follow-up. Table 3.20 shows the absolute and relative regional circumferential strain changes at 3-months and 6-months follow up (raw data is provided in the supplement in Table 6.6). Table 3.21 has all the P-values from statistical analysis of regional circumferential strain changes (both absolute and relative) over 3-months and 6-months follow-up. Figures 3.15 shows the evolution of regional circumferential strain changes over time.

Table3.20. Absolute and relative regional circumferential strain changes (±SD) based on AHA model at 3-months (t2) and 6-months (t3) compared to baseline (t1).

AHA segment	t2-t1 (absolute)		t2-t1 % (relative)		t3-t1 (absolute)		t3-t1 % (relative)	
	Mean	SD	Mean	SD	Mean	SD	Mean	SD
1	0.5	6.4	7.2	36.4	2.8	3.0	-13.4	13.8
2	3.9	4.4	-41.4	62.6	0.2	3.7	5.1	31.0
3	7.7	10.0	-71.0	96.5	0.6	3.7	5.2	31.8
4	2.1	3.1	-9.6	18.0	1.9	3.6	-11.5	24.0
5	-3.7	8.2	-45.0	129.6	-4.0	7.5	-40.6	113.3
6	-2.1	5.6	15.9	30.4	-2.9	5.2	18.5	26.8
7	0.3	2.6	-1.0	14.2	3.6	4.7	-15.3	23.6
8	-1.2	3.4	7.2	18.8	-0.6	3.4	5.2	20.4
9	-0.5	2.9	6.1	20.9	1.5	4.0	-2.4	24.4
10	0.5	3.7	3.4	29.0	0.5	4.1	6.3	40.2
11	-1.4	5.1	18.4	44.2	-1.5	1.5	12.4	16.3
12	2.3	7.9	-16.7	64.2	2.5	1.0	-15.5	9.1
13	-2.7	3.4	14.4	17.1	0.4	3.2	0.0	17.2
14	-2.0	2.2	9.7	11.9	1.1	3.5	-2.5	17.1
15	-2.0	3.3	10.7	14.7	1.4	2.9	-4.3	12.7
16	-1.1	4.8	7.8	27.0	2.3	3.9	-8.8	17.5

Table3.21. P-values associated with statistical analysis on absolute and relative regional circumferential strain value changes at 3-months (t2) and 6-months (t3) compared to baseline (t1).

AHA segment	t2-t1 (absolute)	t2-t1 (relative)	t3-t1 (absolute)	t3-t1 (relative)
1	0.2	0.64	**0.046**	**0.04**
2	**0.0156**	**0.0156**	0.4	0.4
3	**0.0391**	**0.0469**	0.9	0.84
4	0.14	0.24	0.29	0.33
5	0.31	0.42	0.28	0.45
6	0.4	0.24	0.27	0.18
7	0.78	0.87	0.07	0.2
8	0.4	0.38	0.59	0.59
9	0.67	0.49	0.44	0.83
10	0.76	0.78	0.73	0.73
11	0.51	0.34	0.078	0.057
12	0.5	0.54	**0.0024**	**0.0123**
13	0.1	0.078	0.88	0.99
14	0.055	0.055	0.15	0.43
15	0.18	0.12	0.34	0.48
16	0.58	0.5	0.24	0.31
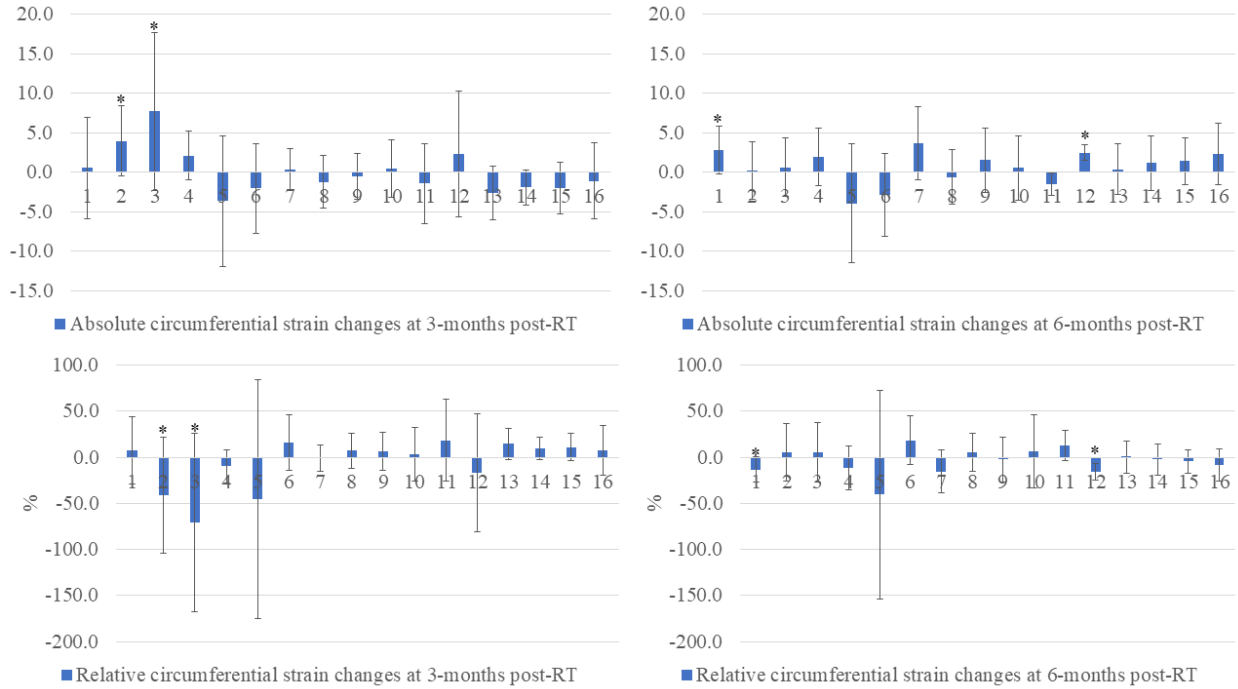
Figure 3.15. Absolute and relative circumferential strain changes at 3-months and 6-months following RT compared to baseline. Star sign indicates significant differences (P<0.05).

No significant changes of circumferential strain values were noted among different dose ranges at 3-months (P>0.19) and 6-months (P>0.063) follow-up. In addition, no correlation was noted between the radiotherapy doses and circumferential strain changes at 3- or 6-months follow-up (P>0.83). Figure 3.16 shows the circumferential strain changes over various dose ranges at 3-months and 6-months post-RT. Figure 3.17 shows the correlation between circumferential strain and dose.
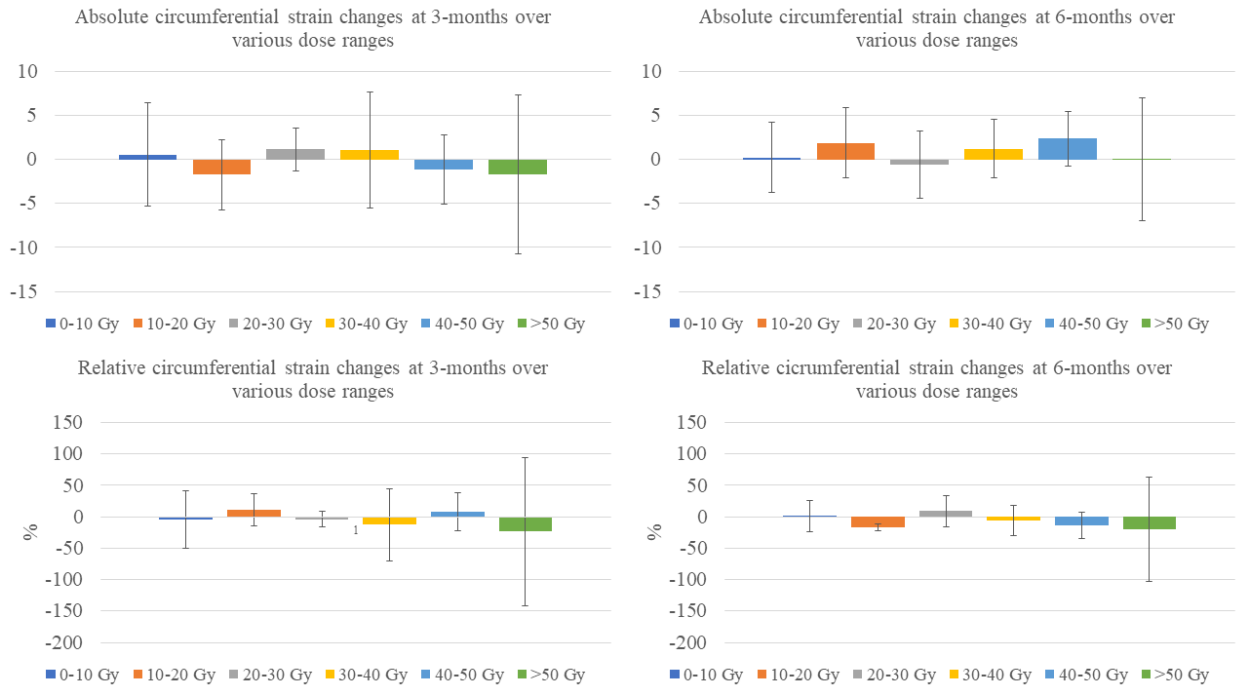
Figure3.16. Absolute and relative changes of circumferential strain at 3-months and 6-months post-RT compared to baseline over various dose ranges
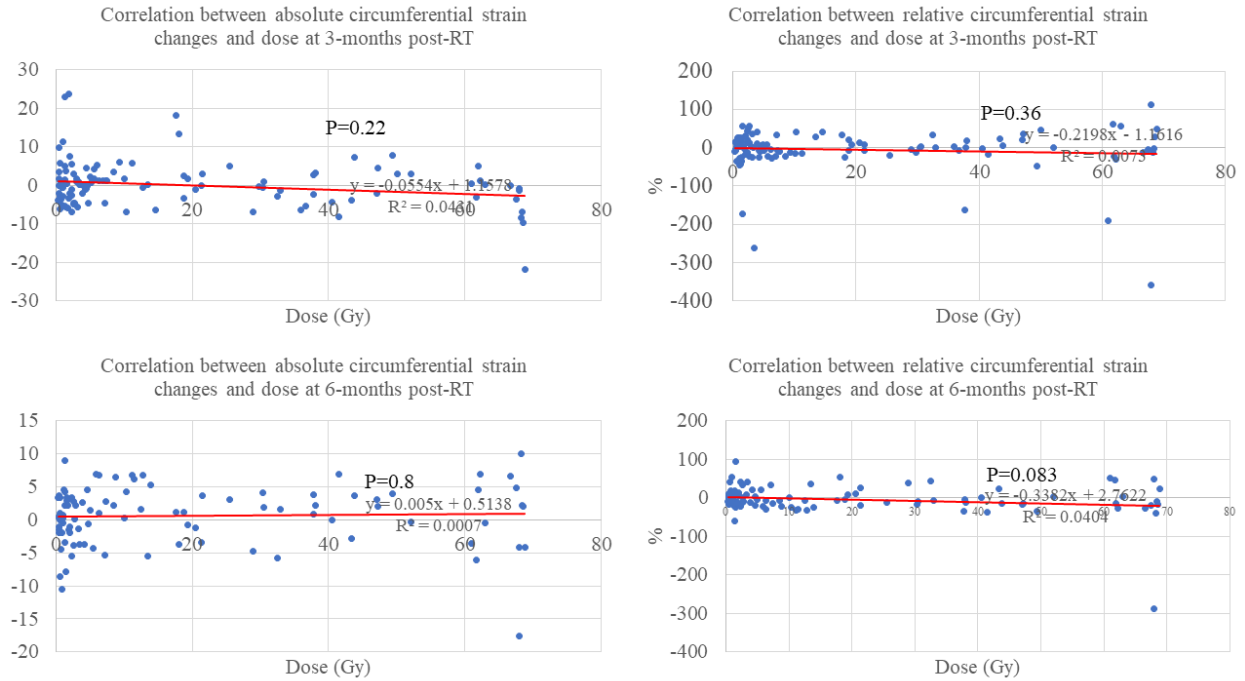
Figure3.17. Correlation between the dose and absolute/relative circumferential strain changes at 3-months and 6-months follow up

Longitudinal strain: Significant decrease of regional longitudinal strain values were found in segment 9 at 3-months follow-up (relative: -62.4±73.3% P=0.0313) and segment 2 (relative: -88.6±105.9 % P=0.0469), segment 3 (absolute: 10.4±11.5 P=0.0313, relative: -85.7±111.7 % P=0.0313), and segment 9 (absolute: 3.4±6.9 P=0.0313, relative: -50.5±22.8 % P=0.0313) at 6-months follow-up. Interestingly, a significant increase of longitudinal strain was noted at segment 8 (absolute: -4.5±3.2 P=0.0313, relative: 31.7±22.0 % P=0.0313) at 3-months post-RT completion. Table 3.22 shows the absolute and relative regional longitudinal strain changes at 3-months and 6-months follow up (raw data is provided in the supplement in Table 6.7). Table 3.23 has all the P-values from statistical analysis of regional longitudinal strain changes (both absolute and relative) over 3-months and 6-months follow-up. Figures 3.18 shows the evolution of regional longitudinal strain changes.

Table3.22. Absolute and relative regional longitudinal strain changes (±SD) based on AHA model at 3-months (t2) and 6-months (t3) compared to baseline (t1).

AHA segment	t2-t1 (absolute)		t2-t1 % (relative)		t3-t1 (absolute)		t3-t1 % (relative)	
	Value	SD	Value	SD	Value	SD	Value	SD
1	-3.9	12.4	-63.2	205.2	1.8	6.4	-0.3	47.5
2	3.8	16.3	-57.2	93.5	3.0	11.0	-88.6	105.9
3	-1.2	8.8	-6.5	22.9	10.4	11.5	-85.7	111.7
4	-1.6	5.5	13.9	36.5	1.3	4.5	-3.6	28.0
5	0.8	2.5	-2.8	12.2	1.2	3.6	-6.6	19.7
6	1.0	16.3	-16.5	76.5	5.9	11.9	-19.9	65.6
7	-3.2	4.8	34.0	40.3	-0.8	6.3	11.7	48.9
8	-4.5	3.2	31.7	22.0	1.4	6.2	-5.3	32.8
9	-2.4	13.4	-62.4	73.3	3.4	6.9	-50.5	22.8
10	-2.1	3.9	10.8	53.1	-4.8	12.6	-18.2	84.1
11	3.0	9.5	-11.3	116.1	0.4	9.4	-52.3	149.2
12	-4.1	14.8	-10.0	57.3	19.2	17.8	-92.7	90.9
13	0.1	2.2	0.8	13.3	0.8	3.7	-4.7	21.4
14	0.6	4.8	1.0	34.9	-0.3	3.2	2.3	16.5
15	0.8	3.2	-6.9	24.2	0.8	5.5	7.5	46.6
16	3.8	14.7	15.3	201.4	-1.8	13.3	-128.2	259.4

Table3.23. P-values associated with statistical analysis on absolute and relative regional longitudinal strain value changes at 3-months (t2) and 6-months (t3) compared to baseline (t1).

AHA segment	t2-t1 (absolute)	t2-t1 (relative)	t3-t1 (absolute)	t3-t1 (relative)
1	0.46	0.47	0.99	0.99
2	0.58	0.18	0.56	**0.0469**
3	0.55	0.22	**0.0313**	**0.0313**
4	0.51	0.38	0.53	0.78
5	0.47	0.59	0.49	0.48
6	0.58	0.65	0.63	0.52
7	0.14	0.078	0.61	0.68
8	**0.0313**	**0.0313**	0.68	0.84
9	0.21	**0.0313**	**0.0313**	**0.0313**
10	0.23	0.81	0.43	1
11	0.46	0.81	0.92	0.46
12	0.62	0.78	0.24	0.34
13	0.93	0.88	0.64	0.56
14	0.77	0.94	0.84	0.68
15	0.54	0.51	0.84	0.84
16	0.54	0.85	0.78	0.31
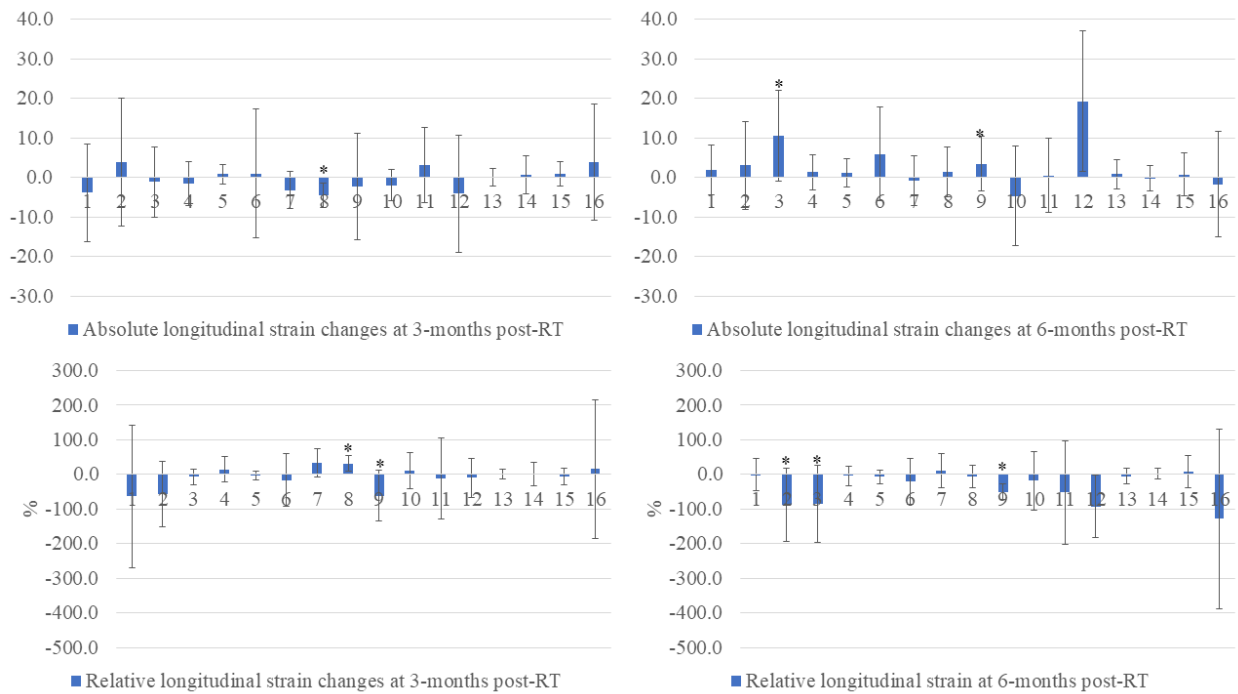
Figure3.18. Absolute and relative longitudinal strain changes at 3-months and 6-months following RT compared to baseline. Star sign indicates significant differences (P<0.05).

Similar to radial and circumferential strain, no dose-dependency (P>0.15) or correlation (P>0.23) with dose were observed between regional longitudinal strain and the maximum radiation doses at 3- or 6-months follow ups. Figure 3.19 shows the longitudinal strain changes over various dose ranges at 3-months and 6-months post-RT completion. Figure 3.20 shows the correlation between longitudinal strain and dose at 3-months and 6-months.

In regards to DENSE MRI analysis, since it was our first run of DENSE acquisition, the acquired images were unfortunately noisy and incapable of further analysis; therefore, we decided to only report strain analysis measured by tissue tracking which was much less noisy. A summary of DENSE analysis from a few available data is provided in the supplement, though (Tables 6.8-6.9).
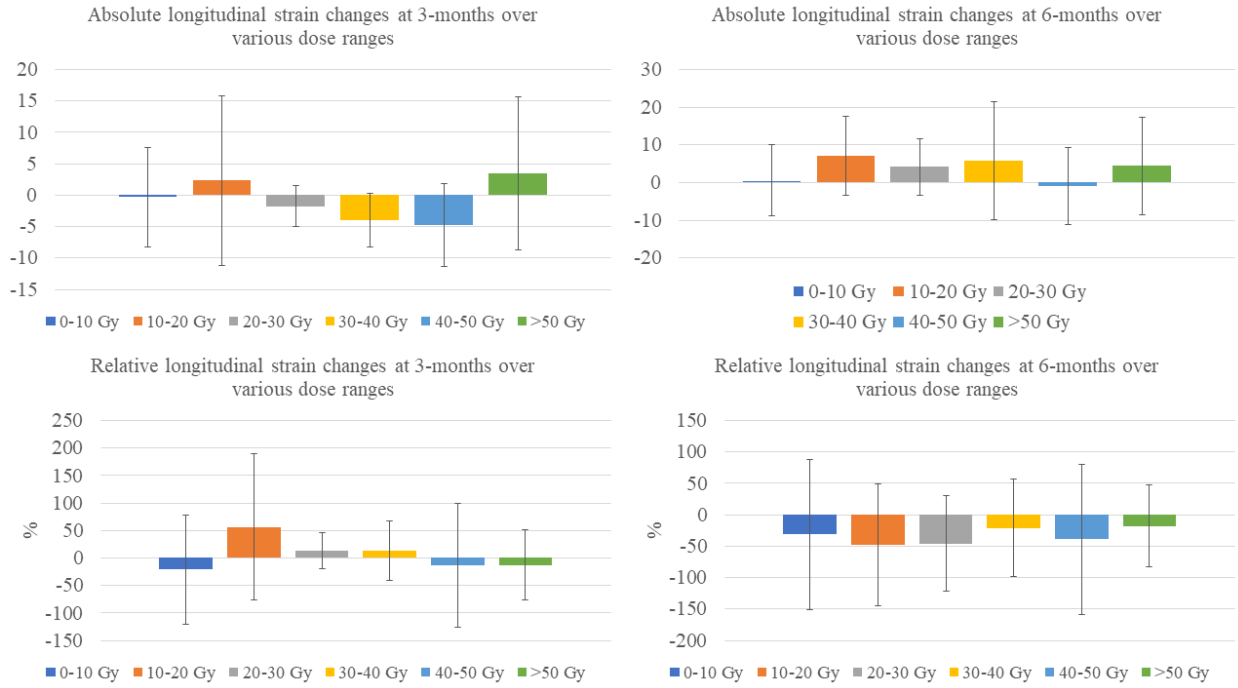
Figure3.19. Absolute and relative changes of longitudinal strain at 3-months and 6-months post-RT compared to baseline over various dose ranges
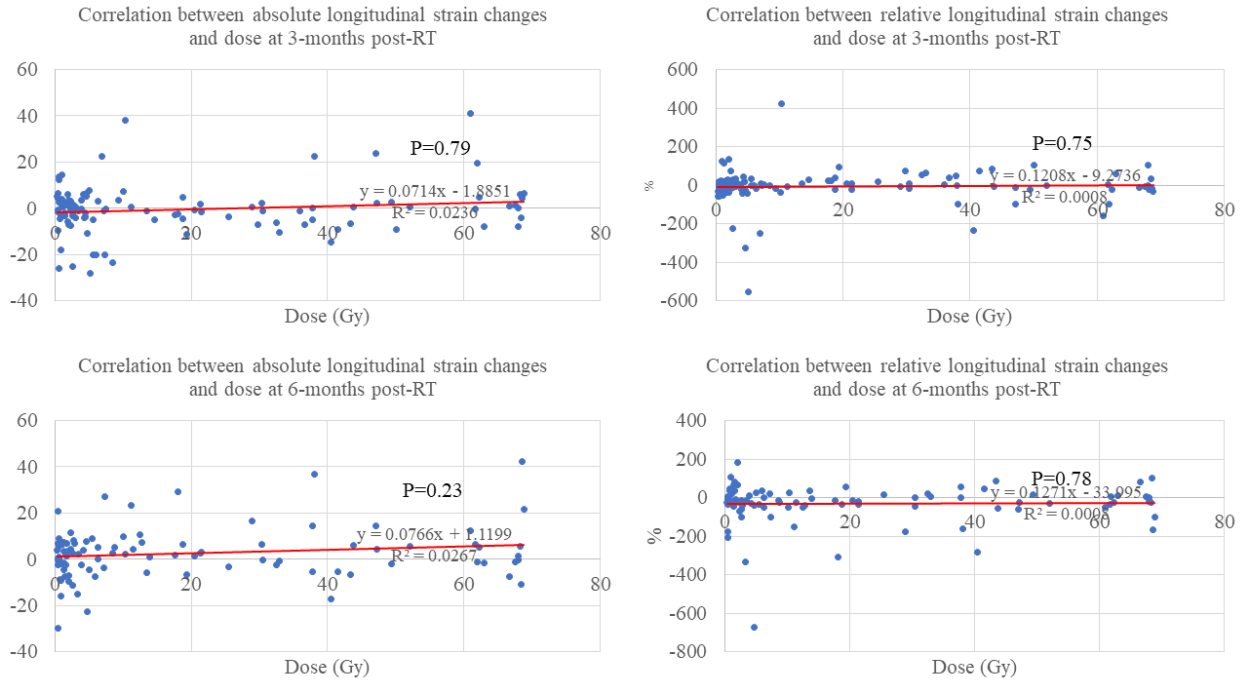
Figure3.20. Correlation between the dose and absolute/relative longitudinal strain changes at 3-months and 6-months follow up

LGE: Regional enhanced volume changes were noted at both 3-months (segment 1 (absolute: 9.1±5.8 % P=0.036), segment 3 (absolute: 18.9±8.9 % P=0.034), segment 8 (absolute: 2.6±1.6 % P=0.037)) and 6-months (segment 1 (absolute: 11.4±8 % P=0.0458), segment 3 (absolute: 8.8±4.3 P=0.037)) follow-up. Increased enhanced volume is a representation of fibrosis scar tissue in myocardium. Table 3.24 shows the absolute regional enhanced area changes at 3-months and 6-months follow up (raw data is provided in the supplement in Table 6.10). Table 3.25 has all the P-values from statistical analysis of regional enhanced area changes over 3-months and 6-months follow-up. Figure 3.21 shows the evolution of changes in regional enhanced area.

95

Table3.24. Absolute and relative regional enhanced area changes (±SD) based on AHA model at 3-months (t2) and 6-months (t3) compared to baseline (t1).

AHA segment	t2-t1% (absolute)		t3-t1% (absolute)	
	Mean	SD	Mean	SD
1	9.1	5.8	11.3	8.0
2	13.6	14.2	10.9	9.4
3	18.9	8.9	8.8	4.3
4	17.2	19.9	10.3	23.2
5	15.1	26.4	18.1	21.5
6	8.6	10.0	14.6	13.5
7	1.2	5.1	4.4	6.9
8	2.6	1.6	5.8	6.0
9	-8.2	5.2	-5.2	8.8
10	-0.4	11.0	-4.6	7.1
11	3.6	9.1	0.6	6.2
12	7.6	8.0	5.6	6.4
13	-0.1	3.2	-1.7	2.0
14	-1.5	1.6	-5.6	5.2
15	0.0	0.0	3.1	3.5
16	1.5	2.0	1.2	1.6

Table3.25. P-values associated with statistical analysis on absolute and relative regional enhanced area changes at 3-months (t2) and 6-months (t3) compared to baseline (t1).

AHA segment	t2-t1 (absolute)	t3-t1 (absolute)
1	**0.036**	**0.0458**
2	0.19	0.137
3	**0.034**	**0.037**
4	0.23	0.5
5	0.39	0.24
6	0.23	0.15
7	0.7	0.35
8	**0.037**	0.19
9	0.07	0.67
10	0.95	0.34
11	0.54	0.86
12	0.198	0.22
13	0.98	0.24
14	0.19	0.16
15	0.39	0.22
16	0.26	0.27
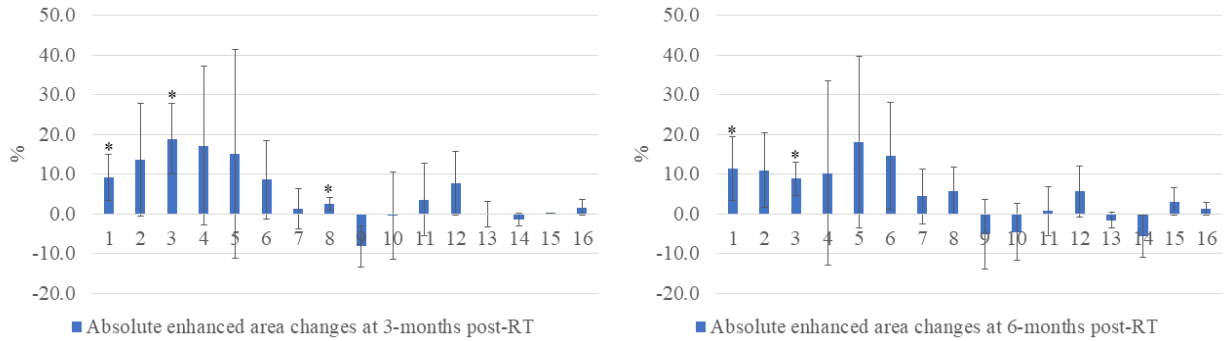
Figure3.21. Absolute enhanced area changes at 3-months and 6-months following RT compared to baseline. Star sign indicates significant differences (P<0.05).

Changes of enhanced volumes over various dose ranges were significantly higher between doses >50 Gy and 0-10 Gy (absolute: 14±16.3% vs 1.2±8.3% P= 0.0097) and >50 Gy and 20-30 Gy (absolute: 14±16.3% vs -4.1±9.3% P=0.0331) at 6-months follow-up. No significant differences were noted at 3-months follow-up between the changes of enhanced areas and radiation doses (P>0.19). Table 3.26 lists the changes of enhanced area over various dose ranges at 3-months and 6-months follow-up. Table 3.27 are a summary of P-values from the statistical analysis between absolute changes of enhanced area at 6-months follow-up. Figure 3.22 shows the absolute changes of enhanced area over various dose ranges.

Table 3.26. Absolute changes of enhanced area over various dose ranges.

Dose range (Gy)	t2-t1% (absolute)		t3-t1% (absolute)	
	Mean	SD	Mean	SD
0-10	3.9	10.6	1.2	8.3
10-20	21.8	19.4	8.7	15.4
20-30	-3.3	11.5	-4.1	9.3
30-40	-0.4	3.0	0.2	4.5
40-50	2.1	-	12.4	10.7
>50	11.7	17.7	14.0	16.3

Table3.27. Summary of statistical analysis between the absolute changes of enhanced area over various dose ranges at 6-months follow-up.

Dose range (Gy)	0-10	10-20	20-30	30-40	40-50
10-20	0.3397				
20-30	0.3101	0.2385			
30-40	0.7059	0.4085	0.6761		
40-50	0.0741	0.2397	0.099	0.136	
>50	**0.0097**	0.3479	**0.0331**	0.0577	0.5
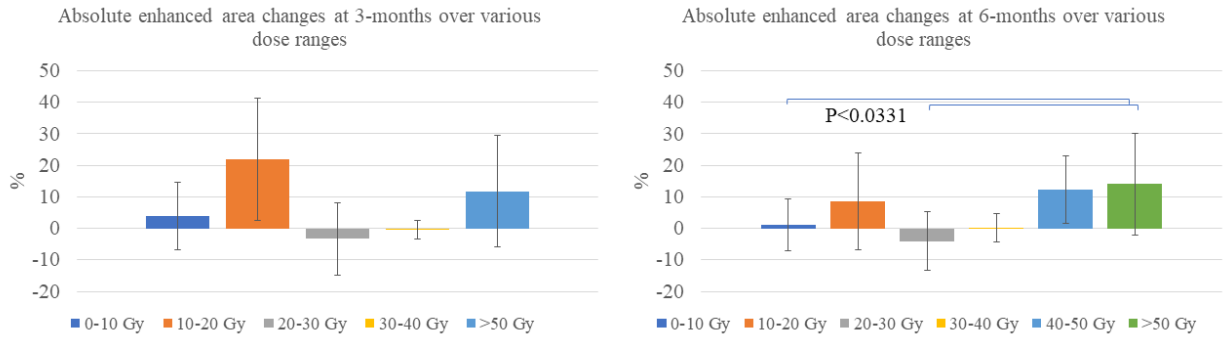
Figure3.22. Absolute changes of enhanced area at 3-months and 6-months post-RT compared to baseline over various dose ranges.

Correlation of enhanced volume changes and the radiation dose was also noted at 6-months follow-up (P<0.001). No correlation was noted at 3-months following RT (P>0.053). Figure 3.23 shows the correlations between radiotherapy dose and enhanced volume changes at 3-months and 6-months post-RT.
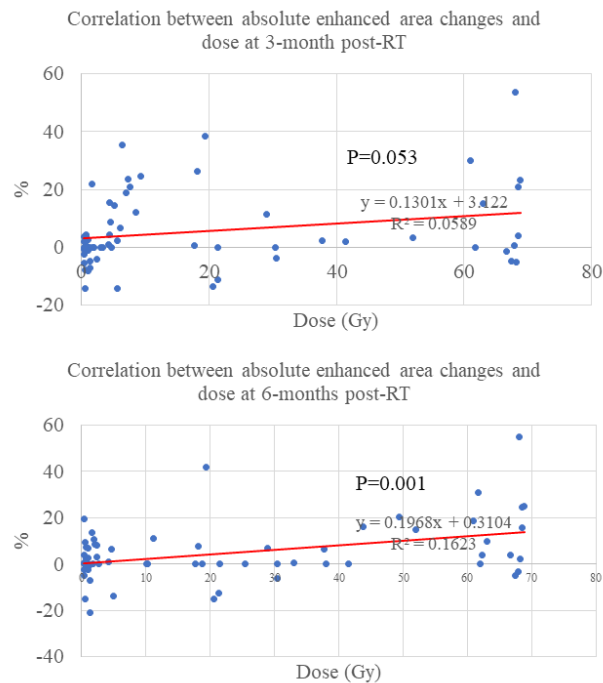
Figure3.23. Correlation between the dose and absolute enhanced area changes at 3-months and 6-months follow up.

In addition to evaluating correlation with dose, correlations of MRI metrics with one another were also calculated. Among all the MRI-derived metrics, only T1 signal changes were significantly correlated with T2 signal changes at 6-months follow-up (P<0.0001). Figure 3.24 shows T1 and T2 signal correlations at 6-months post-RT. No other correlations were noted between T1, ECV, circumferential/radial/longitudinal strain, enhanced volume from LGE MRI, and T2 at either 3-months or 6-months follow-up. Tables 3.28-3.31 are the summary of P-values obtained from correlation analysis between different metrics.
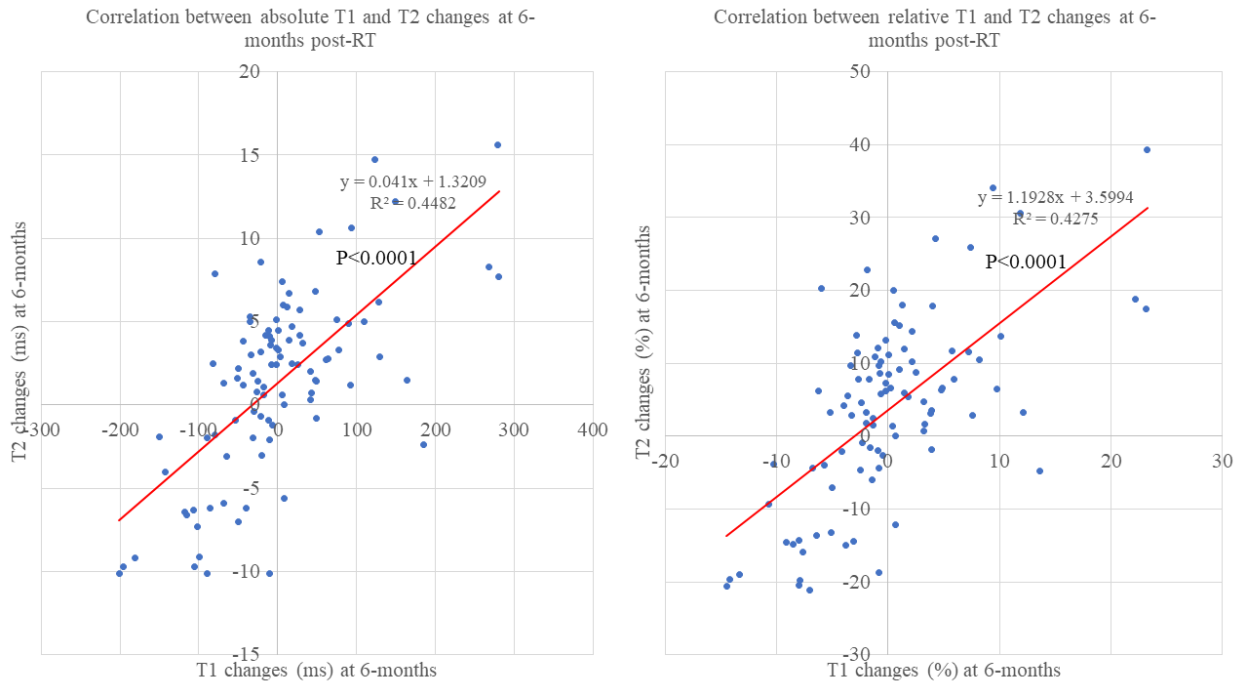
Figure3.24. Correlation between T1 and T2 signal changes at 6-months follow up.

Table3.28. Summary of statistical analysis for correlation between absolute changes of MRI-based metrics between baseline and 3-months follow up (t2-t1).

MRI-based Metrics	T1	T2	ECV	LGE
T2	0.5807			
ECV	0.3145			
LGE	0.5548	0.6449		
Radial strain	0.8867	0.4216	0.7859	0.7512
Circumferential strain	0.4593	0.8863	0.7745	0.5525
Longitudinal strain	0.5273	0.9363	0.6524	0.5442

Table3.29. Summary of statistical analysis for correlation between relative changes of MRI-based metrics between baseline and 3-months follow up (t2-t1 relative).

MRI-based metrics	T1	T2	ECV
T2	0.8184		
ECV	0.4563	0.5963	
Radial strain	0.6666	0.4069	0.3025
Circumferential strain	0.7644	0.6192	0.5487
Longitudinal strain	0.7337	0.3598	0.5962

Table3.30. Summary of statistical analysis for correlation between absolute changes of MRI-based metrics between baseline and 6-months follow up (t3-t1).

MRI-based metrics	T1	T2	ECV	LGE
T2	**<0.0001**			
ECV	0.7695	0.5789		
LGE	0.6453	0.0557	0.1024	
Radial strain	0.1909	0.1918	0.3652	0.1425
Circumferential strain	0.4487	0.2404	0.2984	0.1065
Longitudinal strain	0.7103	0.9640	0.6874	0.9805

Table3.31. Summary of statistical analysis for correlation between relative changes of MRI-based metrics between baseline and 6-months follow up (t3-t1 relative).

MRI-based metrics	T1	T2	ECV
T2	**<0.0001**		
ECV	0.4765	0.2685	
Radial strain	0.3684	0.2023	0.6985
Circumferential strain	0.8198	0.8948	0.4795
Longitudinal strain	0.5723	0.7655	0.5596

3.4. Discussion

The lack of significant changes in global metrics (e.g., LVEF) suggests that the heart may maintain its global function at 3-months and 6-months post-RT completion even though regional changes or damages may occur. The only global metrics that showed a significant difference were T2 signal at 3-months and enhanced volume from LGE at 6-months follow up. This implies that if one is interested in monitoring cardiac function following RT via global metrics, radiobiological

measurements (e.g., T2 mapping and LGE MRI) may be more effective than global functional/structural measurements (e.g., strain) since the heart as a whole may compensate for regional mechanical damage.

In contrast to global metrics, various regional metrics manifested significant changes at one or both of the follow-ups. T1 signal, T2 signal, enhanced volume from LGE MRI, radial, circumferential, and longitudinal strain values showed significant differences as early as 3 months post-RT completion at regional AHA segments. Significant regional T1 signal changes (50 ms) were higher than the temporal variability detectable difference (29 ms) [46] while the significant largest regional T2 signal changes (2.5 ms) were closely in overlap with the temporal variability reported in the literature (3.0 ms) suggesting a careful consideration of T2 signal changes is needed for future evaluation of cardiotoxicity. Though, it should be noted that the reported minimal tissue characterization parameters changes were obtained from a 1.5T scanner while the images for this study were acquired from a 3T scanner which may alter the temporal variability differences and raises the need for assessment of minimal T1/T2 detectable difference for magnetic fields with different strengths in the future.

For a few metrics, namely, T1 signal, LGE, and radial strain, the significant changes occurred at anterior regions of the LV where radiation doses were higher. Interestingly, one of the AHA segments (#8) demonstrated a relative increase in longitudinal strain at 3 months following RT. The reason behind these unexpected changes may be due to error or focal damages at some other parts of the heart and the ability of the heart to compensate its global function by exerting extra strain at other focal spots (e.g., segment number 8 of the AHA model at 3-months). Similar to 3-months follow-up, regional metrics also showed significant changes at 6-months follow-up except for T1 and T2 signal. Even though the trend of T1/T2 signal changes seemed to increase at 6

months post-RT, the changes did not reach statistical significance, likely due to small sample size and variabilities in the patient population. The only regional metric that did not show any significant global or regional changes was ECV, which was limited in the number of patients due to a lack of post-contrast T1 in multiple patients.

In regards to correlation of MRI-derived metrics with radiation dose, biological changes (e.g., T1/T2 signal and enhanced volume from LGE MRI) demonstrated a dose-dependent response at one or both follow-ups. Specifically, changes in T1 signal, T2 signal, and enhanced area signal after 6 months were significantly elevated in regions exposed to higher doses (e.g., >50 Gy and 40-50 Gy) than lower doses (e.g., 0-10 Gy and 10-20 Gy). Notably. T1 signal changes were greater for higher doses at both 3- and 6-months follow-up, suggesting it may be an earlier indicator of RT-induced cardiac damage (i.e., myocardial fibrosis) compared to other metrics at 3 months. Strain measurements did not indicate any dose-dependent changes at 3- or 6-months follow-up, suggesting that early contractibility changes may not be directly associated with local radiation dose, though could be affected by indirect changes from damages to other sites of the myocardium.

Besides significant changes of biological-based metrics, the linear correlation between the radiotherapy dose and T1 and T2 signal changes were found at both 3- and 6-months follow-up, with stronger correlations at 6-months post-RT completion. Enhanced volume of LGE also demonstrated linear correlation with radiotherapy dose at 6-months follow-up. This means that higher radiation doses may lead to higher T1 (i.e., indicator of fibrosis and inflammation) and T2 (i.e., indicator of edema) signals starting at 3 months post-RT, and the probability of these effects significantly increases with dose at 6-months. This is supported by the strong correlation of LGE signal (i.e., indicator of scar tissue) and dose at 6-months following RT completion.

Correlation of MRI metrics with one another at 3-months and 6-months follow-up also demonstrated interesting results. The only correlation between changes in metrics was found between T1 and T2 signal. Specifically, a positive correlation was measured between the increase of T1 signal changes and the increase of T2 signal changes at 6-months following RT completion. This may imply that the increase of myocardial fibrosis/inflammation might increase the probability of myocardial edema at 6-months following RT completion.

There were a few limitations associated with this study including small sample size, variability in patient population (e.g., age, gender, tumor stage, prescribed dose), missing data in a few imaging acquisitions (e.g., patient did not show up for one of the follow-up scans and/or patient's allergy reaction to contrast agent and hence elimination of LGE and post-contrastT1 imaging during MRI scanning), variability in slice selection/location during different follow-ups, and intra/inter-observer variability in data analysis. In addition, the correlations were measured without consideration of the variabilities among patients with regards to using multiple data points (i.e., AHA segment measurements) per person; a more comprehensive correlation comparison would require accounting for both within-patient and across-patient variability. As an advanced statistical test, a generalized linear mixed model has been shown to be a useful technique when the data have more than one source of random variability. Thus, for future work when larger data sets are available, it is recommended to do the related dose-correlations with consideration of patient-specific variables using a generalized linear mixed model. Lastly, lower signal to noise ratio in GRE cine MR images may have affected the LV volume measurements, and it is recommended to use steady state free precession cine imaging for evaluation of the LV mass/volume to provide higher signal to noise ratio compared to GRE in evaluation of cardiac function [72].

3.5. Conclusion

Global metrics are unable to detect early myocardial damages/changes at 3- or 6-months following RT (except for radiobiological-based metrics such as T2 mapping and LGE MRI) while regional metrics can not only detect focal changes but also have shown a dose-dependent response. Higher focal radiation doses (e.g., >50 Gy) are associated with elevations in radiobiological changes (e.g., T1/T2/Enhanced signal) compared to lower doses (e.g., 0-10 Gy). This suggests that direct radiobiological changes may precede mechanical changes at 3- and 6-months following RT completion. In addition, T1 and T2 signal changes showed a linear correlation at 6-months which may indicate that the probability of fibrosis or inflammation may increase myocardial edema at local regions of the myocardium at 6-months post-RT. Finally, due to the ability of regional MR to detect early changes, as well as correlating many changes to local radiation dose, we conclude that regional evaluation of the myocardium is superior; therefore, clinicians may find future benefit in using regional MRI metrics as early indicators of CVT to improve the selection and timing of mitigations/interventions before CVT becomes irreversible. Future studies with a larger sample size are needed to fully examine the benefits of regional MRI-based evaluation of the heart over longer follow-ups.

4 Spatiotemporal evolution of aortic function before and after RT

4.1. Introduction

Similar to the effects of RT on the heart and its substructures, the ionizing radiation may damage the aortic wall as well. In current clinical practice, the aortic health/stiffness is measured by pulse wave velocity (PWV) which is the pulse transit time (PTT) over a known distance of the aortic trunk [73]. Even though PWV can measure the arterial stiffness, the mechanical changes along the length of the aorta may be missed depending on where the pulse wave is measured. Therefore, it is important to use other global metrics (e.g., global circumferential strain) to measure the aortic changes at multiple cross-sections. In addition to great importance of global measurements, regional measurements are also valuable in evaluation of aortic function since the regional aortic vulnerabilities and local flow-induced shear stresses acting on the endothelium of the aortic wall could be missed by global or homogenized metrics of aortic function [74]. This is important because of the mechanobiological response of the endothelial cells to local flow-induced shear stress acting on the luminal surface of the aorta that may lead to regional remodeling/changes in the aortic wall [74]. Therefore, the use of non-invasive MRI sequences, such as 4D-flow MRI, could provide additional clinically relevant information by quantifying patient-specific aortic properties such as flow-induced shear stress acting on the luminal wall by the blood flow.

Aortic measurements are not only important in assessment of aortic health, but also may play an important role in evaluation of cardiac health. Heart and aortic functions are dependent on one another to maintain optimal systemic circulation. In other words, cardiac dysfunction may induce aortic dysfunction and vice versa. For example, subclinical damages to regions of the aorta (e.g., increased stiffness in the ascending aorta) may increase afterload on the heart (and change wave

reflections) which can alter cardiac mechanics and the energy required to maintain cardiac output. Thus, it is important to assess both global and regional function of the heart and aorta as biological/biomechanical dysfunction in one may proceed the other (i.e., MRI-derived metrics of one structure may predict morphological changes in the other organ). That is, quantification of either heart or aortic performance may predict possible future damages in either and provide relevant information for planning mitigations/interventions.

For this study, changes in aortic function at 3-month and 6-month follow-up were evaluated using GRE cine MRI to measure global aortic wall strain at different axial positions along the aorta and 4D-flow PC-MRI to assess regional/global flow-induced shear stress. The primary regions of interests were the whole ascending aorta, mid-ascending aorta, and mid descending aorta. Mean circumferential strain was obtained at the mid-ascending/descending aorta, and longitudinal strain was calculated over the ascending aorta from the aortic valve to the origin of the innominate artery. The flow-induced shear stress was measured at the level of mid-ascending/descending aorta at equivalent locations to the cross-sectional cine imaging. Potential correlations were evaluated between the RT dose and the MR-derived aortic metrics, and between the cardiac measurements and aortic metrics at ascending aorta (where the LV is directly attached to the aorta) over different time-points. Finally, changes in regional cardiac strain at the septum were compared with RT dose at the ascending aorta to evaluate whether aortic dose affects the regional cardiac function, particularly at the septal regions at basal and mid-ventricle levels where the greater curvature of the aorta is attached to the LV.

4.2. Methods

Data: Following the same IRB-approved protocol as Chapter 2&3, including patients, treatment plan, and timelines, the following scans were acquired to assess aortic function before and after RT.

MR imaging

GRE cine MRI: cine MRI (20° flip angle, 5 mm slice thickness, TE: 3 to 5 ms, TR: 8 to 10 ms) was performed at the mid-ascending aorta and mid-descending thoracic aorta at planes perpendicular to the aortic centerline to assess aortic morphology and quantify the mean circumferential strain by manual measurement of aortic wall diameter at systolic and diastolic phases using cvi42 software (Figure 4.1). A longitudinal cross-section of the ascending aorta was also acquired using the 'three-point tool' on the Siemens MRI interface using GRE cine MRI to estimate the mean longitudinal strain between the aortic valve and the innominate artery (Figure 4.2). A semi-automatic algorithm was implemented in MATLAB to track the boundary of the greater curvature and calculate the peak linearized strain (equation 1).

$$Linearized\ strain = \frac{Change\ in\ length}{initial\ length}\ (1)$$
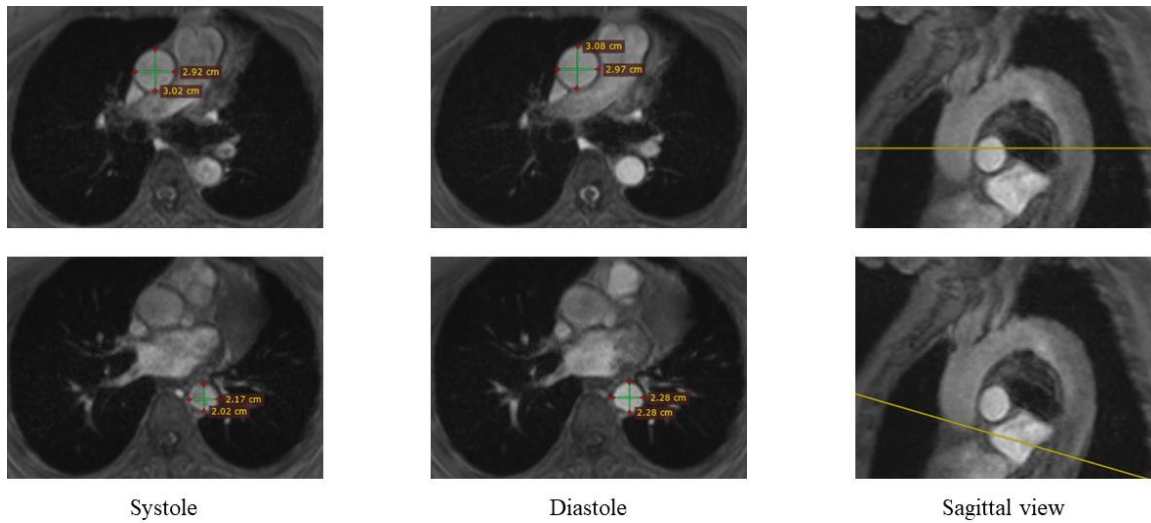
Figure 4.1. Typical cine images acquired at the mid-ascending aorta (top row) and mid-descending aorta (bottom row).
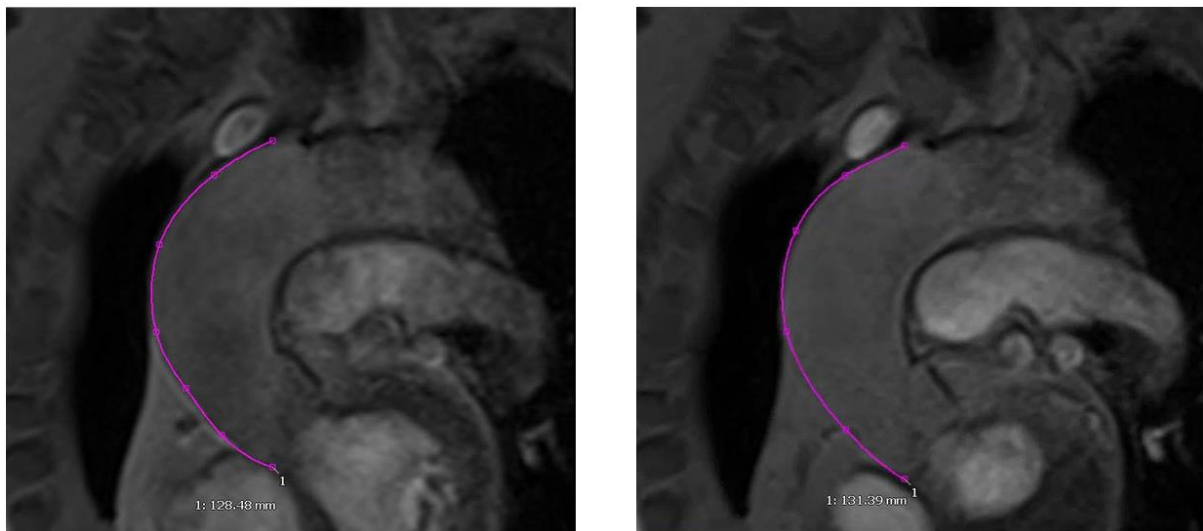
Figure 4.2. Typical cine images obtained at the level of the aortic valve to the innominate artery for longitudinal strain measurements.

4D phase-contrast (PC) MRI: 4D-Flow PC-MRI of the aorta was acquired by established protocols (free-breathing, respiratory-gated, 3D velocity-encoding, TE: 2.25 ms, TR: 36.64 ms, slice thickness: 2.5 mm, ETL: 1, 12º flip angle) over the entire thoracic aorta. Following manual selection of the points at the center of the aorta from the aortic valve, through the aortic arch, and down the descending thoracic aorta, the aortic centerline and initial segmentation of the aortic wall

were performed using built-in algorithms within CAAS 4D Flow (Pie Medical Imaging) software. Following manual refinement of the segmentation, global and regional (i.e., division of aortic wall into four equal segments as shown in Figure 4.3) wall shear stress (WSS) were quantified, along with its corresponding peak magnitude at the mid-ascending and mid-descending aorta.
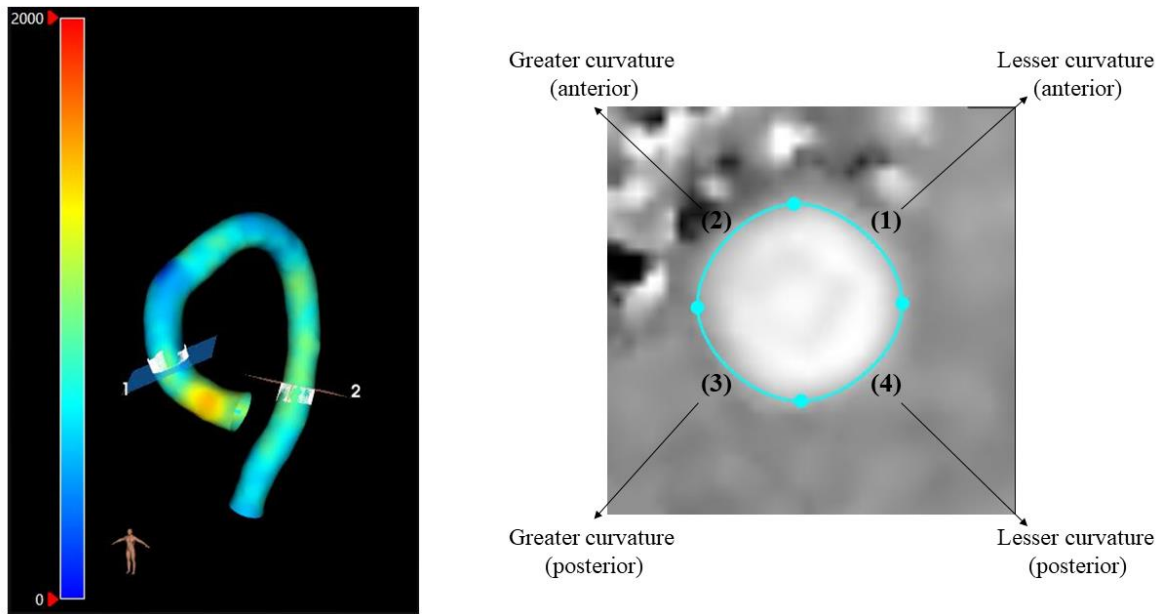
Figure4.3. Wall shear stress distribution along the aorta including at mid-ascending aorta (plane 1) and mid-descending aorta (plane 2) from 4D-flow analysis (left). Regional segmentation and the corresponding anatomical landmarks are shown in the right.

All strain and WSS values at 3-months and 6-months were then compared to the pre-RT baseline values. For absolute comparisons, the values at each follow-up were subtracted from the baseline measurements (equation 2). For relative comparison, changes of each metric were relatively compared to baseline values as shown in equation 3.

112

$$Absolute\ changes = (b - a)\ (2)$$

$$Relative\ changes = \left(\frac{b - a}{a}\right) * 100\ (3)$$

b: *follow up measurements, a*: *baseline measurements*

Statistics: Absolute and relative changes of circumferential strain at the mid-ascending and mid-descending aorta, and the changes in longitudinal strain in the ascending aorta, were compared at 3-months and 6-months post-RT to baseline using a paired t-test. The same statistical test was used to measure the global and regional changes of WSS at the mid-ascending and mid-descending aorta over 3-months and 6-months follow-up. Dose-dependency of strain and WSS values were measured using Pearson's correlation. Also, the correlation of global aortic metrics (at ascending aorta where LV is attached to the aorta) and global cardiac metrics were assessed at 3- and 6-months follow up using Pearson's correlation test.

In addition, the correlation between the RT dose at ascending aorta and changes in regional circumferential/radial/longitudinal strain values of the septal segments of the LV (segments 2, 3, 8, and 9 of the AHA model) over 3-months and 6-months post-RT treatment were determined using Pearson's correlation to evaluate whether the radiation dose to the ascending aorta can impact the mechanical changes at locations where the LV and the greater curvature of ascending aorta are attached.

It should also be noted that for the datasets in which the assumption of normality were not met, Wilcoxon Singed-Rank test and Spearman correlation test were run instead of paired t-test and Pearson's correlation test, respectively. All statistical tests were run based on significance level of $p \leq 0.05$ using JMP software.

4.3. Results

The data were analyzed based on the above approach. A list of sample sizes for each metric at 3-months and 6-months is provided in Table 4.1.

Table 4.1. Summary of sample sizes for each metric at 3-months and 6-months follow-up.

	Global		Regional	
	3-months	6-months	3-months	6-months
Circumferential Strain at mid-ascending aorta	6	6	-	-
Circumferential Strain at mid-descending aorta	6	6	-	-
Longitudinal Strain at ascending aorta	4	4	-	-
Wall shear stress at mid-ascending aorta	4	4	16	16
Wall shear stress at mid-descending aorta	4	4	16	16

Global circumferential strain at the mid-ascending and mid-descending aorta and the longitudinal strain of the ascending aorta, did not show any significant differences over 3- and 6-months follow-up compared to baseline (P>0.29). Also, global WSS at the mid-ascending and mid-descending aorta did not significantly change at 3-months and 6-months compared to baseline (P>0.0625). Table 4.2 is a summary of global measurements changes at 3-months and 6-months follow-up compared to baseline. Table 4.3 provides the P-values from statistical analysis for evaluation of absolute and relative changes at 3-months and 6-months follow up compared to baseline. Figure 4.4 is a representation of global strain values at baseline, 3-months and 6-months follow-up. Figure 4.5 shows the global WSS changes (absolute and relative) at 3-months and 6-months post-RT compared to baseline.

Table 4.2. Summary of absolute and relative global metrics changes between 3-months follow-up and baseline and 6-months follow-up and baseline. t1, t2, and t3 are indicators of baseline, 3-months and 6-months measurements, respectively.

Global Metrics	t2-t1 (absolute)		t2-t1 % (relative)		t3-t1 (absolute)		t3-t1 % (relative)	
	Mean	SD	Mean	SD	Mean	SD	Mean	SD
Circumferential strain at mid-ascending aorta	-0.01	0.0	-38.7	24.20	0.00	0.03	6.96	56.80
Circumferential strain at mid-descending aorta	-0.02	0.05	-0.14	52.72	-0.03	0.07	-2.85	52.61
Longitudinal strain at ascending aorta	0.02	0.08	16.78	67.39	-0.05	0.06	-26.50	41.14
Global WSS at mid-ascending aorta	64.6 mPa	42.5 mPa	13.9	7.5	31.5 mPa	70.5 mPa	7.8	11.9
Global WSS at mid-descending aorta	62.3 mPa	93.7 mPa	14.6	21.5	9.6 mPa	72.4 mPa	4.5	12.8

Table 4.3. Summary of p-values from the statistical analysis for evaluation of absolute and relative global aortic metrics changes at 3-months (t2) and 6-months (t3) compared to baseline (t1).

Global Metrics	t2-t1 (absolute)	t2-t1 (relative)	t3-t1 (absolute)	t3-t1 (relative)
Circumferential strain at ascending aorta	0.56	0.49	0.77	0.79
Circumferential strain at descending aorta	0.82	0.69	0.43	0.9
Longitudinal strain at ascending aorta	0.43	0.69	0.29	0.34
Global WSS at ascending aorta	0.0625	0.0625	0.625	0.375
Global WSS at descending aorta	0.1875	0.1875	0.5	0.55
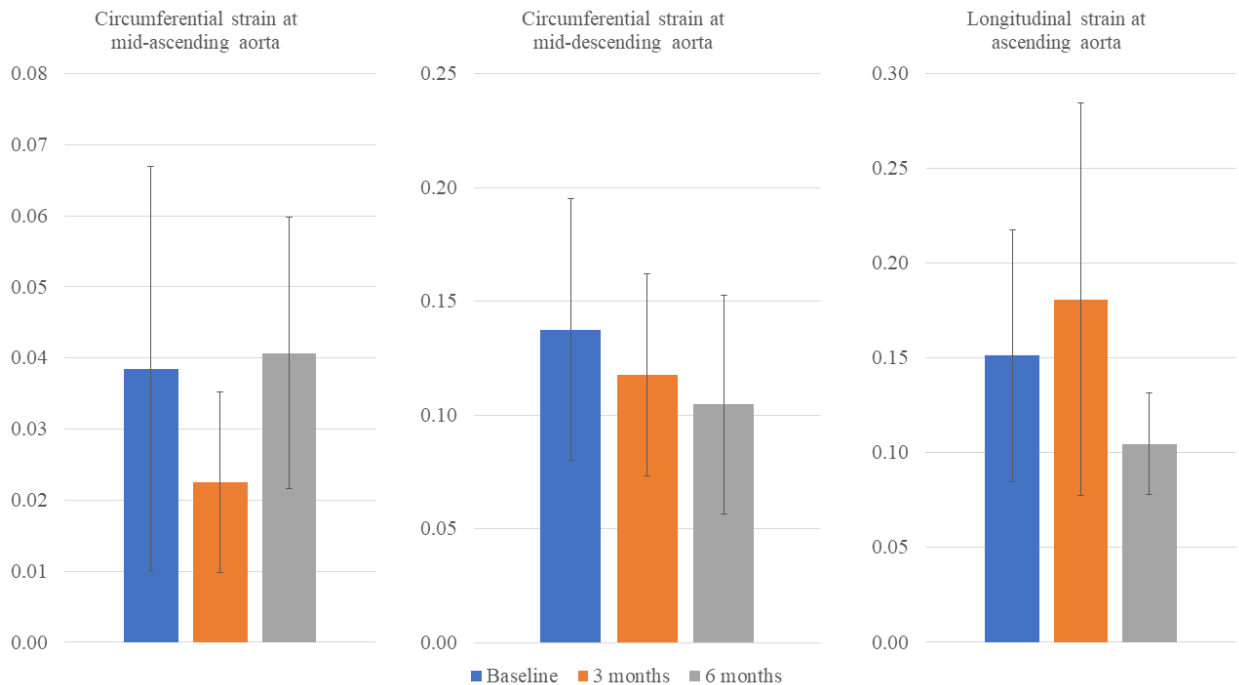
Figure 4.4. Global circumferential strain values (±SD) at mid ascending aorta, mid-descending aorta, and longitudinal strain values (±SD) at ascending aorta at baseline, 3-months post-RT, and 6-months post-RT.
.
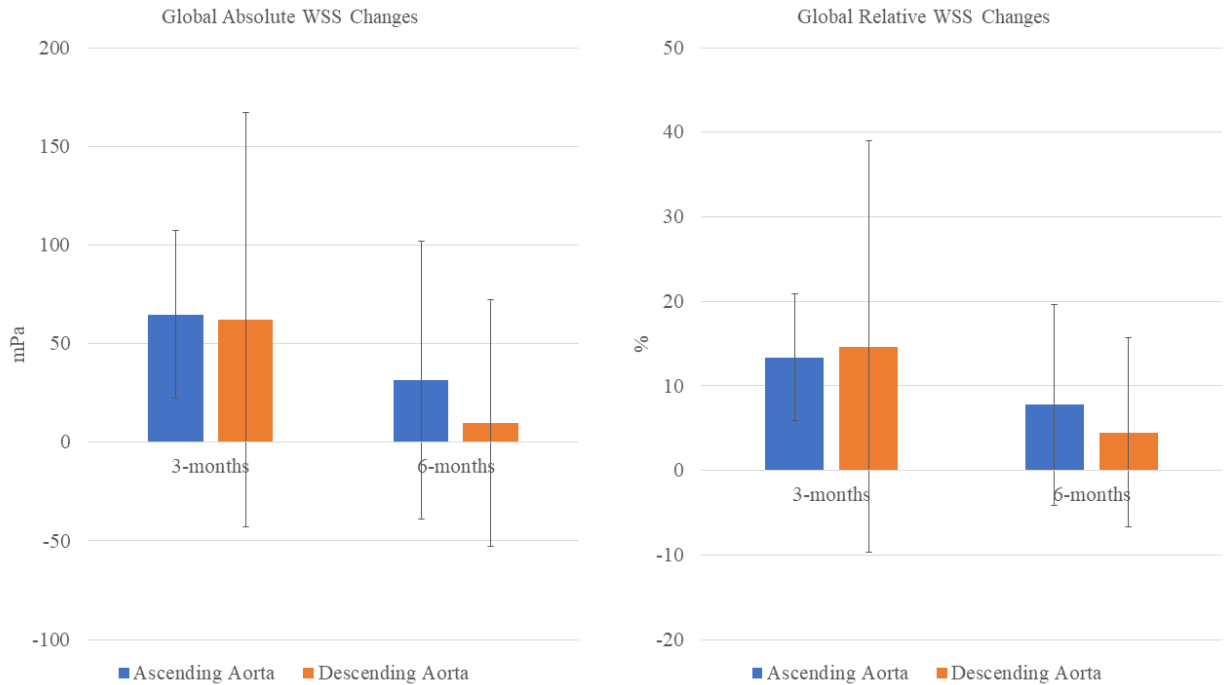
Figure 4.5. Absolute and relative global wall shear stress (WSS) value changes (±SD) at mid descending aorta and mid-descending aorta at 3-months and 6-months post-RT.

Similar to global measurements, regional measurements of WSS also did not show significant differences at 3-months and 6-months follow up compared to baseline (P>0.066). Though, an almost significant increase of WSS was noted for sector 2 (i.e., inferior of the greater curvature) of the ascending aorta at 6-months compared to baseline (122.4±73 mPa, P=0.066). Figure 4.6 shows the absolute and relative regional WSS changes over segments 1-4 at 3-months and 6-months follow up. Table 4.4 is a summary of p-values for evaluation of segmental WSS changes at mid-ascending and mid-descending aorta following RT.
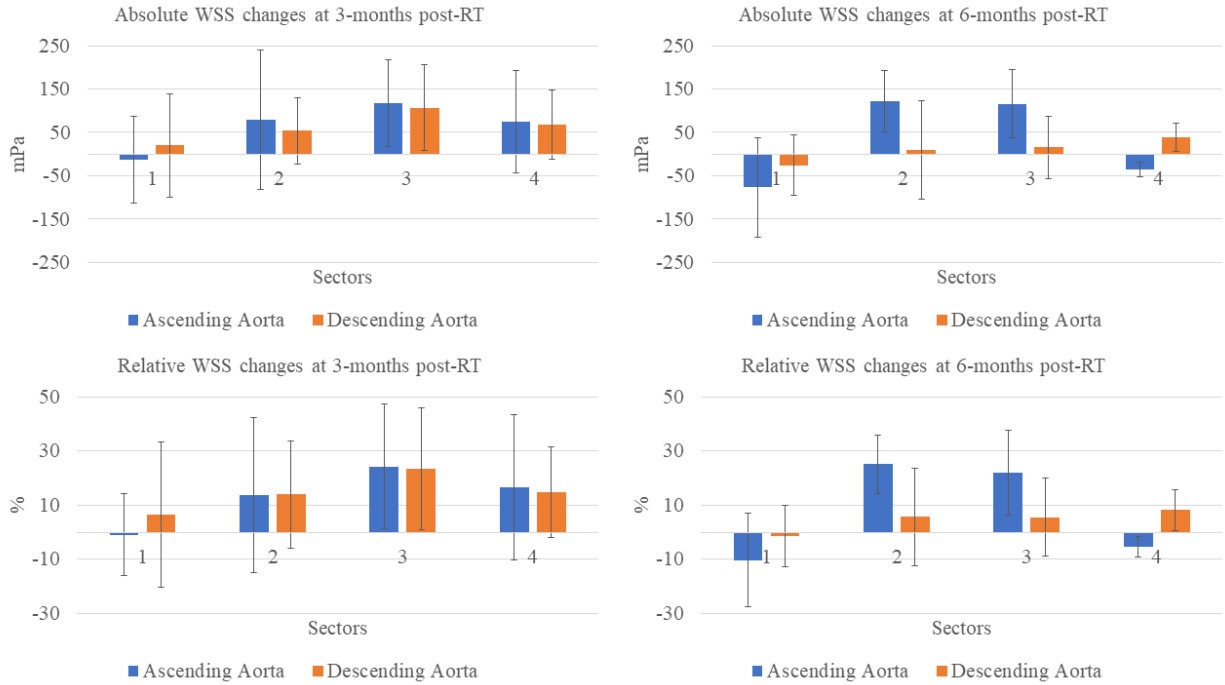
Figure 4.6. Absolute and relative regional wall shear stress (WSS) value changes (±SD) at the ascending aorta and mid-descending aorta at 3-months and 6-months post-RT.

Table 4.4. Summary of p-values from statistical analysis for evaluation of regional wall shear stress (WSS) absolute/relative changes at 3-months (t2) and 6-months (t3) compared to baseline (t1).

Aortic wall segments	t2-t1 (absolute)		t2-t1 (relative)		t3-t1 (absolute)		t3-t1 (relative)	
	Ascending aorta	Descending aorta	Ascending aorta	Descending aorta	Ascending aorta	Descending aorta	Ascending aorta	Descending aorta
Sector 1	0.561	0.4375	0.5	0.35	0.779	0.672	0.7581	0.5621
Sector 2	0.3125	0.1875	0.4375	0.1545	0.066	0.4563	0.081	0.3507
Sector 3	0.125	0.0799	0.125	0.0845	0.087	0.3979	0.094	0.5191
Sector 4	0.3125	0.1173	0.3125	0.1137	0.945	0.1188	0.875	0.1323

No correlation was found between ascending aortic dose and circumferential or longitudinal strain or global WSS changes at ascending aorta (P>0.0986), and between descending aortic dose and

circumferential or global WSS changes at descending aorta at 3-months and 6-months following

RT (P>0.2906). Table 4.5 is a summary of p-values obtained from correlation measurements.

Table 4.5. Summary of p-values from correlation tests done between global aortic metrics absolute/relative changes and the corresponding delivered RT dose. t1, t2, and t3 are indicators of baseline, 3-months and 6-months measurements, respectively.

Metrics	t2-t1 (absolute)	t2-t1 (relative)	t3-t1 (absolute)	t3-t1 (relative)
Circumferential Strain at ascending aorta	0.6717	0.7876	0.5372	0.6656
Circumferential Strain at descending aorta	0.5071	0.2906	0.697	0.5227
Longitudinal strain at ascending aorta	0.4475	0.7154	0.0986	0.2665
WSS at Ascending aorta	0.53	0.82	0.447	0.447
WSS at Descending aorta	0.7699	0.66	0.965	0.957

Moreover, no correlation was found between cardiac metrics and aortic metrics (at ascending aorta) changes at 3-months, between cardiac metrics and aortic metrics (at ascending aorta) changes at 6-months, between cardiac metrics at 3-months and aortic metrics (at ascending aorta) at 6-months and vice versa (P>0.068). Though, a near significant (P=0.068) correlation was found between the longitudinal aortic strain increase at ascending aorta at 3-months (26.7±9.2%) and global LV longitudinal strain decrease (-13±6.4%) at 6-months follow-up compared to baseline. A list of p-values associated with these results is shown in Table 4.6-4.9.

Table 4.6 Summary of p-values from correlation measurements between global cardiac metrics and aortic metrics at ascending aorta at 3-months follow up.

Aortic metrics at ascending aorta	Cardiac metrics					
	T1 signal	T2 signal	Radial strain	Circumferential strain	Longitudinal strain	LGE
WSS	0.8261	0.5236	0.8636	0.9525	0.3035	-
Circumferential strain	0.4805	0.8395	0.3667	0.3856	0.268	0.3
Longitudinal strain	0.6812	0.3533	0.594	0.6046	0.882	-

Table 4.7. Summary of p-values from correlation measurements between global cardiac metrics and aortic metrics at ascending aorta at 6-months follow up.

Aortic metrics at ascending aorta	Cardiac metrics					
	T1 signal	T2 signal	Radial strain	Circumferential strain	Longitudinal strain	LGE
WSS	0.4072	0.1425	0.1772	0.946	0.6295	-
Circumferential strain	0.8646	0.6302	0.7597	0.8387	0.7202	0.2911
Longitudinal strain	0.4599	0.621	0.8495	0.992	0.6598	0.07

Table 4.8. Summary of p-values from correlation measurements between global cardiac metrics at 3-months and aortic metrics at ascending aorta at 6-months follow up.

Aortic metrics at ascending aorta	Cardiac metrics					
	T1 signal	T2 signal	Radial strain	Circumferential strain	Longitudinal strain	LGE
WSS	0.665	0.487	0.74	0.6056	0.28	0.91
Circumferential strain	0.8659	0.1407	0.415	0.3618	0.6726	0.605
Longitudinal strain	0.124	0.6643	0.4882	0.4435	0.3787	-

Table 4.9. Summary of p-values from correlation measurements between global cardiac metrics at 6-months and aortic metrics at ascending aorta at 3-months

Aortic metrics at ascending aorta	Cardiac metrics					
	T1 signal	T2 signal	Radial strain	Circumferential strain	Longitudinal strain	LGE
WSS	0.6655	0.4869	0.7146	0.9349	0.2805	0.57
Circumferential strain	0.6929	0.1239	0.7728	0.927	0.2979	0.748
Longitudinal strain	0.9749	0.8349	0.2734	0.1992	0.068	0.78

Finally, correlation between strain changes at segments 2, 3, 8, and 9 of the AHA model (i.e., the septal wall of the LV where greater curvature of ascending aorta is attached to the LV myocardium) and the radiation dose to the ascending aorta demonstrated strong negative correlation between the relative changes of radial or circumferential strain in segment #2 at 6-months follow-up and the maximum radiation dose to the ascending aorta (radial strain and dose: P=0.0169, circumferential strain and dose: P=0.0206). No correlation was found between radiation dose and the changes in radial or circumferential strain in segments 2, 3, 8, or 9 at 3-months follow up (P>0.15) or the changes in regional longitudinal strain in segments 2, 3, 8, or 9 at 3-months or 6-months follow-up (P>0.0684). Figure 4.7 shows the correlation between the radial/circumferential strain changes at segment 2 of AHA model and the radiation dose to the ascending aorta.
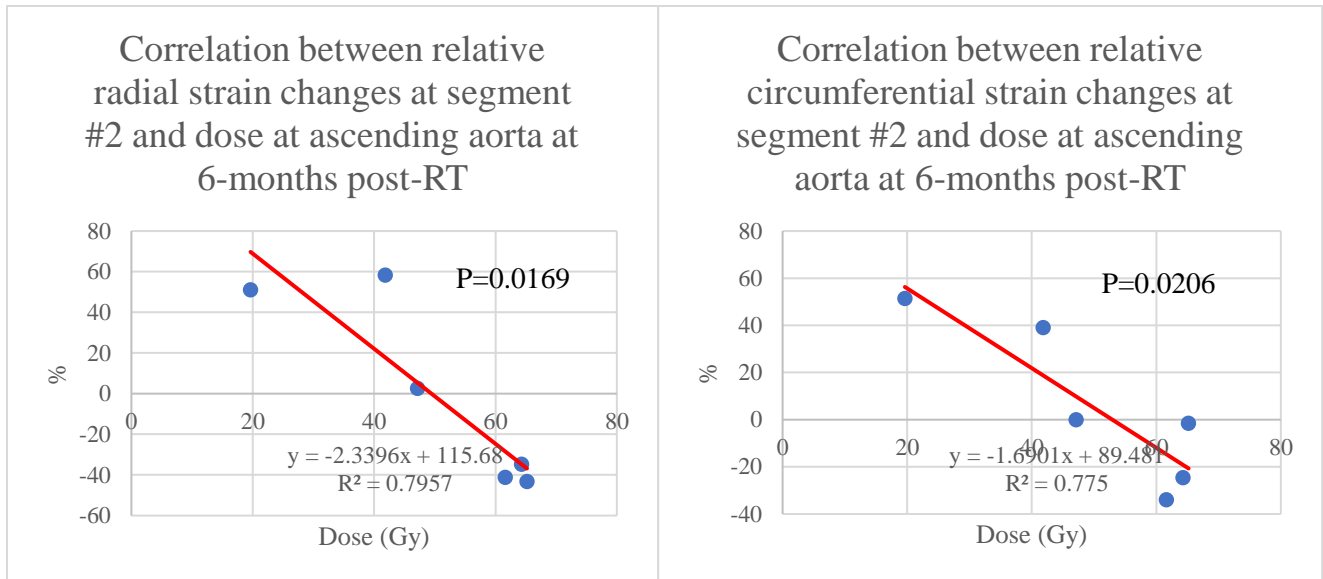
Figure 4.7. Correlation between relative radial and circumferential strain changes at segment 2 of AHA model and dose to ascending aorta at 6-months follow up.

4.4. Discussion

Mean circumferential/longitudinal strain and WSS as global metrics did not show any significant changes at 3- and 6-months follow-up for the population of patients as a whole. This could be due to limitations of global metrics in evaluation of possible isolated regional damages to the aorta. To elaborate, the focal aortic damages may not be widespread enough to show up on limited global assessments of the aortic metrics both because it may not affect the entire region scanned and that only a focal area of the ascending/descending aorta were evaluated. Regional evaluation of WSS also did not show any significant changes at 3-months and 6-months except for one sector (#2, located at inferior of the greater curvature) of the mid-ascending aorta where the WSS increase was near significance (P=0.068) at 6-months which could be an early sign of aortic remodeling

over this region. Longer follow-ups with a larger cohort of patients are required to fully examine this matter.

Also, the correlation between global cardiac metrics changes and global aortic metrics changes at the ascending aorta did not show any relations at the same follow-up (i.e., both at 3-months or 6-months) and different follow-up (i.e., cardiac metrics changes at 3-months vs aortic metrics changes at 6-months and vice versa) except for a nearly significant correlation between the longitudinal strain increase of ascending aorta at 3-months with the LV longitudinal strain drop at 6-months post-RT. A larger cohort of patients are required to explore if the early aortic longitudinal strain increase is an early sign for the cardiac contractibility dysfunction at 3-months later.

Finally, no correlation was found between the global aortic metrics and the corresponding imparted RT dose. This suggests that RT dose may not directly impact the global aortic changes. MR sequences with higher resolution are required to segment the aortic wall thickness and explore the possible correlation between focal RT dose and regional MRI-based aortic measurements. Despite lack of direct correlation between the dose and aortic metrics, a dose-dependency correlation was found between the aortic dose at ascending aorta and radial/circumferential strain changes at 6-months at segment 2 (i.e., basal anterior segment of the LV myocardium) of the AHA model. This implies that even though no dose-dependency was found between the radiation dose to the heart and radial, circumferential, or longitudinal strain values of the LV myocardium, RT-induced aortic damages to the ascending aorta may indirectly impact the kinematics of the myocardium at regions where the aorta and LV are in mechanical continuity. In other words, radiation may not always directly damage the biological and/or functional characteristics of the site where RT was delivered rather, in some cases, it may indirectly affect the functional and/or radiobiological features of the sites which are further away from the focal radiation to maintain the global function of the

124

cardiovascular system. Recognition of this potential indirect effect on cardiac function is not to downplay the direct effects of radiation on local myocardial properties but to highlight the interdependency of cardiovascular function as a complete system.

There were a few limitations associated with this study including a small sample size, missing data in multiple patients (due to patient's absence for the follow-up scan, addition of some of the metrics to the protocol at a later time and noise in some of the acquired images), missing multiple axial slices of the aorta at ascending/descending aorta, variability in slice location/selection over different follow-up points, and inter/intra-observer variability in manual measurement of aortic wall diameter.

4.5. Conclusion

Global circumferential/longitudinal strain and regional/global WSS measurements at various locations of the aorta did not demonstrate early aortic toxicity due to RT at 3-month and 6-months follow-up in this pilot study of lung cancer patients as a whole.

No correlation was found between the global cardiac metrics changes and aortic metrics changes at the same or different follow ups. Also, no correlation was found between the aortic RT dose and aortic metrics at 3-months or 6-months post-RT. However, a negative correlation was noted between the RT dose to the ascending aorta and changes in radial and circumferential strain in the septal wall of the LV which implies that the aortic radiation may have an indirect impact on myocardial function, specifically in regions of the heart in mechanical continuity to the aorta. Future studies should carefully consider changes to these locations where the heart and aorta interact to identify early signs of CVT.

5 Summary

Accurate image registration plays an important role in the true assessment of RT-induced CVT and the evaluation of the correlation of MRI-based metrics with RT dose. In addition, image registration can be used to quantify the dose magnitude variation over the respiratory and cardiac motion. In fact, it was shown that in lung cancer patients with tumors located at the upper lobe of the lung, the LV mean RT dose is significantly higher in expiration compared to inspiration breathing phase. In expiration breath-hold, significantly higher LV mean RT dose was also estimated at diastole compared to systole. No significant differences were found in RT maximum dose between respiratory phases or cardiac phases since the highest iso-dose lines always passed through LV regardless of the cardiopulmonary motion effect. Evaluation of dose at LVM showed higher mean dose deposition compared to LV due to smaller volume of LVM. More importantly, segmental evaluation of LVM (i.e., AHA model) demonstrated 2~3 times higher mean RT dose at regions closer to the tumor compared to the global mean dose estimated from the corresponding non-cardiac-gated but respiratory-gated 4D-CT images. This emphasizes the importance of regional dose evaluation particularly for RT-induced CVT assessments. Also, the dose variations during the respiratory and cardiac motion suggest that in lung cancer patients with tumors located in the upper lobe of the lung, the dose delivered to the heart could be reduced by delivering the radiation during inspiration and if possible at the systolic cardiac phase. This novel workflow opens the door for future assessment of cardiopulmonary dose-variation in lung cancer patients with tumors at the lower lobe of the lung and other patient populations (e.g., esophageal cancer, breast cancer) with larger cohorts. Also, higher resolution images with respiratory- and cardiac-gated information over all the phases will provide more comprehensive results for a more confident conclusion and future recommendations.

To assess the RT-induced CVT, multiple MRI-based metrics were used to assess the cardiac function following RT. Serial global and regional assessment of cardiac function at 3-months and 6-months following RT completion showed that global metrics (e.g., LVEF) were unable to detect early myocardial damages. The only global metrics that showed significant differences were T2 signal and LGE suggesting that global biological damages may precede mechanical changes. Unlike global metrics, regional metrics including mechanical measurements (e.g., strain) showed significant changes at one or both follow-ups. Notably, significantly higher T1 signal, radial strain, and LGE changes were noted in highly-irradiated regions. For the radiobiological metrics, a significant increase of signal was noted for regions receiving >50 Gy of radiation compared to lower dose regions (e.g., 0-10 Gy) at 6-months follow-up except, for T1 signal where the dose-dependency changes were found at both 3-months and 6-months follow up suggesting that myocardial fibrosis is a probable early effect of the cardiac radiation. In addition, linear correlations were found between the RT dose and T1 signal, T2 signal, and enhanced volume from LGE MRI at both 3-months and 6-months post-RT with stronger correlations at 6-months. Mechanical changes (i.e., strain) did not show any dose-dependency and/or correlation with RT dose following RT treatment suggesting that contractibility of the myocardium is not dose-dependent at least over 6-months follow-up. Finally, correlation between MRI-based metrics showed that there is a positive correlation between T1 signal changes and T2 signal changes at 6-months following RT suggesting that progression of fibrosis may increase myocardial edema at local regions of the myocardium at 6-months post-RT. This study shows the importance of regional assessment of myocardium following RT with dose-dependency responses found in biological metrics. Future studies with a larger cohort of patients and longer follow-ups are required to fully examine the evolution of RT-induced myocardial toxicity using regional MRI-based metrics.

Exposure of the aorta to ionizing radiation may cause vascular toxicity which requires the same evaluations as other parts of the cardiovascular system given the importance of aortic function in maintaining optimal cardiovascular function. In this project, serial global assessment of the aorta over mid-ascending aorta and mid-descending aorta showed that global circumferential strain and global WSS do not significantly change at 3-months and 6-months follow up. Similarly, longitudinal strain over the ascending aorta did not changes at 3-months and 6-months post-RT completion. Regional WSS assessments also did not show any significant changes; though, the inferior of the greater curvature at mid-ascending aorta showed a nearly significant increase of WSS at 6 months follow up suggesting that aortic wall remodeling may occur at focal regions of the aorta following RT treatment. No dose-dependency was noted between global aortic metrics and the corresponding RT dose. However, the RT dose to the ascending aorta was correlated with the regional radial and circumferential strain changes of Segment 2 of the AHA model (i.e., basal anteroseptal) at 6-months follow-up suggesting that ionizing radiation could have an indirect effect on sites further from the focal radiation itself. This is also an indicator of aortic-LV coupling, in that the damages to one region may induce changes in the other one. This was supported by closely significant correlation between the longitudinal strain increase at ascending aorta at 3-months and the longitudinal strain drop of the LV at 6-months post-RT suggesting that not only aortic and cardiac damages are correlated but one may precede and/or predict the worsening of the other one. No other correlations were found between aortic metrics and cardiac metrics at same or different follow-ups. Future studies with a larger sample size, higher resolution MRI sequences for regional aortic assessments, global measurements over multiple cross-sections of aorta, and longer follow-ups are required to investigate more aspects of the RT-induced aortic toxicity in addition to its correlation with cardiotoxicity.

References

[1]   G. Curigliano *et al.*, "Cardiovascular toxicity induced by chemotherapy, targeted agents and radiotherapy: ESMO clinical practice guidelines," *Ann. Oncol.*, vol. 23, no. SUPPL. 7, pp. vii155–vii166, 2012, doi: 10.1093/annonc/mds293.

[2]   WHO, "Cancer." https://www.who.int/health-topics/cancer.

[3]   WHO, "Cardiovascular Disease," [Online]. Available: https://www.who.int/health-topics/cardiovascular-diseases.

[4]   Z. CHEN and D. AI, "Cardiotoxicity associated with targeted cancer therapies," *Mol. Clin. Oncol.*, vol. 4, no. 5, pp. 675–681, 2016, doi: 10.3892/mco.2016.800.

[5]   C. Jaworski, M. J. A. Mariani, and G. Wheeler, "Cardiac complications of thoracic irradiation," *J. Am. Coll. Cardiol.*, 2013, doi: 10.1016/j.jacc.2013.01.090.

[6]   X. Ming, Y. Feng, C. Yang, W. Wang, P. Wang, and J. Deng, "Radiation-induced heart disease in lung cancer radiotherapy: A dosimetric update," *Med. (United States)*, vol. 95, no. 41, 2016, doi: 10.1097/MD.0000000000005051.

[7]   C. G. Lenneman and D. B. Sawyer, "Cardio-oncology: An update on cardiotoxicity of cancer-related treatment," *Circ. Res.*, vol. 118, no. 6, pp. 1008–1020, 2016, doi: 10.1161/CIRCRESAHA.115.303633.

[8]   J. Bertholet *et al.*, "Real-time intrafraction motion monitoring in external beam radiotherapy," *Phys. Med. Biol.*, vol. 64, no. 15, pp. 1–33, 2019, doi: 10.1088/1361-6560/ab2ba8.

[9]   L. Xing *et al.*, "Overview of image-guided radiation therapy," *Med. Dosim.*, vol. 31, no. 2, pp. 91–112, 2006, doi: 10.1016/j.meddos.2005.12.004.

[10]   M. Awadalla, M. Z. O. Hassan, R. M. Alvi, T. G. Neilan, M. G. Hospital, and G. Hospital, "Advanced imaging modalities to detect cardiotoxicity," *Curr. Probl. Cancer*, vol. 42, no. 4, pp. 386–396, 2019, doi: 10.1016/j.currproblcancer.2018.05.005.Advanced.

[11]   P. Thavendiranathan, F. Poulin, K. D. Lim, J. C. Plana, A. Woo, and T. H. Marwick, "Use of myocardial strain imaging by echocardiography for the early detection of cardiotoxicity in patients during and after cancer chemotherapy: A systematic review," *J. Am. Coll. Cardiol.*, vol. 63, no. 25 PART A, pp. 2751–2768, 2014, doi: 10.1016/j.jacc.2014.01.073.

[12]   T. C. Tan and M. Scherrer-Crosbie, "Cardiac complications of chemotherapy: Role of imaging," *Curr. Treat. Options Cardiovasc. Med.*, vol. 16, no. 4, pp. 1–19, 2014, doi: 10.1007/s11936-014-0296-3.

[13]   P. Lancellotti *et al.*, "Expert consensus for multi-modality imaging evaluation of cardiovascular complications of radiotherapy in adults : a report from the European Association of Cardiovascular Imaging and the American Society of Echocardiography," *Eur. Hear. Journal-Cardiovascular Imaging J. Am. Soc. Echocardiogr.*, vol. 14, pp. 721–740, 2013, doi: 10.1093/ehjci/jet123.

[14] S. Vasu and W. G. Hundley, "Understanding cardiovascular injury after treatment for cancer: An overview of current uses and future directions of cardiovascular magnetic resonance," *J. Cardiovasc. Magn. Reson.*, vol. 15, no. 1, pp. 1–18, 2013, doi: 10.1186/1532-429X-15-66.

[15] W. G. Hundley *et al.*, "ACCF/ACR/AHA/NASCI/SCMR 2010 expert consensus document on cardiovascular magnetic resonance: A report of the american college of cardiology foundation task force on expert consensus documents," *Circulation*, vol. 121, no. 22, pp. 2462–2508, 2010, doi: 10.1161/CIR.0b013e3181d44a8f.

[16] Y. Rong *et al.*, "Rigid and Deformable Image Registration for Radiation Therapy: A Self-Study Evaluation Guide for NRG Oncology Clinical Trial Participation," *Pract. Radiat. Oncol.*, vol. 11, no. 4, pp. 282–298, 2021, doi: 10.1016/j.prro.2021.02.007.

[17] K. K. Brock, S. Mutic, T. R. McNutt, H. Li, and M. L. Kessler, "Use of image registration and fusion algorithms and techniques in radiotherapy: Report of the AAPM Radiation Therapy Committee Task Group No. 132: Report," *Med. Phys.*, vol. 44, no. 7, pp. e43–e76, 2017, doi: 10.1002/mp.12256.

[18] H. Wang *et al.*, "Radiation-induced heart disease : a review of classification , mechanism and prevention," *Int. J. Biol. Sci.*, vol. 15, 2019, doi: 10.7150/ijbs.35460.

[19] T. Wei and Y. Cheng, "The cardiac toxicity of radiotherapy–a review of characteristics, mechanisms, diagnosis, and prevention," *Int. J. Radiat. Biol.*, vol. 97, no. 10, pp. 1333–1340, 2021, doi: 10.1080/09553002.2021.1956007.

[20] E. Belzile-Dugas and M. J. Eisenberg, "Radiation-induced cardiovascular disease: Review of an underrecognized pathology," *J. Am. Heart Assoc.*, vol. 10, no. 18, pp. 1–10, 2021, doi: 10.1161/JAHA.121.021686.

[21] G. D. Lewis and A. Farach, "Cardiovascular Toxicities of Radiation Therapy," *Methodist Debakey Cardiovasc. J.*, vol. 15, no. 4, pp. 274–281, 2019, doi: 10.14797/mdcj-15-4-274.

[22] M. J. Adams, P. H. Hardenbergh, L. S. Constine, and S. E. Lipshultz, "Radiation-associated cardiovascular disease," *Oncology/Hematology*, vol. 45, pp. 55–75, 2003.

[23] J. J. Hufnagle, S. N. Andersen, and E. V. Maani, *Radiation Therapy Induced Cardiac Toxicity*. Treasure Island (FL): StatPearls Publishing, 2021.

[24] S. M. Mrotzek, T. Rassaf, and M. Totzeck, "Cardiovascular damage associated with chest irradiation," *Front. Cardiovasc. Med.*, vol. 7, no. March, pp. 1–7, 2020, doi: 10.3389/fcvm.2020.00041.

[25] E. T. H. Yeh *et al.*, "Cardiovascular complications of cancer therapy: diagnosis, pathogenesis, and management.," *Circulation*, vol. 109, no. 25, pp. 3122–3131, 2004, doi: 10.1161/01.CIR.0000133187.74800.B9.

[26] G. T. Armstrong *et al.*, "Comprehensive echocardiographic detection of treatment-related cardiac dysfunction in adult survivors of childhood cancer: Results from the St. Jude Lifetime Cohort Study," *J. Am. Coll. Cardiol.*, vol. 65, no. 23, pp. 2511–2522, 2015, doi: 10.1016/j.jacc.2015.04.013.

[27] D. J. Cutter *et al.*, "Risk for valvular heart disease after treatment for hodgkin lymphoma," *J. Natl. Cancer Inst.*, vol. 107, no. 4, pp. 1–9, 2015, doi: 10.1093/jnci/djv008.

[28] R. T. Dess *et al.*, "Cardiac events after radiation therapy: Combined analysis of prospective multicenter trials for locally advanced non-small-cell lung cancer," *J. Clin. Oncol.*, vol. 35, no. 13, pp. 1395–1402, 2017, doi: 10.1200/JCO.2016.71.6142.

[29] P. McGale *et al.*, "Incidence of heart disease in 35,000 women treated with radiotherapy for breast cancer in Denmark and Sweden," *Radiother. Oncol.*, vol. 100, no. 2, pp. 167–175, 2011, doi: 10.1016/j.radonc.2011.06.016.

[30] B. M. P. Aleman *et al.*, "Late cardiotoxicity after treatment for Hodgkin lymphoma," *Blood*, vol. 109, no. 5, pp. 1878–1886, 2007, doi: 10.1182/blood-2006-07-034405.

[31] S. C. Darby *et al.*, "Risk of Ischemic Heart Disease in Women after Radiotherapy for Breast Cancer," *N. Engl. J. Med.*, vol. 368, no. 11, pp. 987–998, 2013, doi: 10.1056/nejmoa1209825.

[32] Y. Khalid, M. Fradley, N. Dasu, K. Dasu, A. Shah, and A. Levine, "Gender disparity in cardiovascular mortality following radiation therapy for Hodgkin's lymphoma: A systematic review," *Cardio-Oncology*, vol. 6, no. 1, pp. 4–11, 2020, doi: 10.1186/s40959-020-00067-7.

[33] R. E. Ohman, E. H. Yang, and M. L. Abel, "Inequity in Cardio-Oncology: Identifying Disparities in Cardiotoxicity and Links to Cardiac and Cancer Outcomes," *J. Am. Heart Assoc.*, vol. 10, no. 24, p. e023852, 2021, doi: 10.1161/JAHA.121.023852.

[34] D. A. Mulrooney *et al.*, "Cardiac outcomes in a cohort of adult survivors of childhood and adolescent cancer: Retrospective analysis of the childhood cancer survivor study cohort," *BMJ*, vol. 339, no. 7736, p. 34, 2009, doi: 10.1136/bmj.b4606.

[35] S. H. Giordano, Y.-F. Kuo, J. L. Freeman, T. A. Buchholz, G. N. Hortobagyi, and J. S. Goodwin, "Risk of Cardiac Death After Adjuvant Radiotherapy for Breast Cancer," *J Natl Cancer Inst*, vol. 97, no. 6, pp. 419–424., 2005, doi: 10.1093/jnci/dji067.

[36] A. Kosaraju, A. Goyal, Y. Grigorova, and A. N. Makaryus, "Left Ventricular Ejection Fraction," PMID: 2908., In: StatPearls [Internet]. Treasure Island (FL): StatPearls Publishing, 2021.

[37] M. G. Khouri *et al.*, "Contemporary Reviews in Cardiovascular Medicine Cancer Therapy – Induced Cardiac Toxicity in Early Addressing the Unresolved Issues," *Circulation*, vol. 126, no. 23, pp. 2749–2763, 2012, doi: 10.1161/CIRCULATIONAHA.112.100560.

[38] T. K. M. Wang, D. H. Kwon, B. P. Griffin, S. D. Flamm, and Z. B. Popović, "Defining the Reference Range for Left Ventricular Strain in Healthy Patients by Cardiac MRI Measurement Techniques: Systematic Review and Meta-Analysis," *Am. J. Roentgenol.*, vol. 217, pp. 569–583, 2021, doi: doi.org/10.2214/AJR.20.24264.

[39] D. Kim, W. D. Gilson, C. M. Kramer, and F. H. Epstein, "Myocardial Tissue Tracking with Two-dimensional Cine Displacement-encoded MR Imaging: Development and Initial Evaluation," *Radiology*, vol. 230, no. 3, pp. 862–871, 2004, doi: 10.1148/radiol.2303021213.

[40] B. S. Spottiswoode *et al.*, "Tracking myocardial motion from cine DENSE images using spatiotemporal phase unwrapping and temporal fitting," *IEEE Trans. Med. Imaging*, vol. 26, no. 1, pp. 15–30, 2007, doi: 10.1109/TMI.2006.884215.

[41] J. J. Cao, N. Ngai, L. Duncanson, J. Cheng, K. Gliganic, and Q. Chen, "A comparison of both DENSE and feature tracking techniques with tagging for the cardiovascular magnetic resonance assessment of myocardial strain," *J. Cardiovasc. Magn. Reson.*, vol. 20, no. 1, pp. 1–9, 2018, doi: 10.1186/s12968-018-0448-9.

[42] J. H. Jordan, S. Vasu, T. M. Morgan, R. B. D. Jr, G. C. Meléndez, and C. A. Hamilton, "Anthracycline-Associated T1 Mapping Characteristics Are Elevated Independent of the Presence of Cardiovascular Comorbidities in Cancer Survivors," *Circ Cardiovasc Imaging*, vol. 9, no. 8, pp. 45–67, 2016, doi: 10.1093/med/9780199324491.003.0003.

[43] P. K. Kim *et al.*, "Myocardial T1 and T2 mapping: Techniques and clinical applications," *Korean J. Radiol.*, vol. 18, no. 1, pp. 113–131, 2017, doi: 10.3348/kjr.2017.18.1.113.

[44] C. de Groot *et al.*, "Radiation-Induced Myocardial Fibrosis in Long-Term Esophageal Cancer Survivors," *Int. J. Radiat. Oncol. Biol. Phys.*, vol. 110, no. 4, pp. 1013–1021, 2021, doi: 10.1016/j.ijrobp.2021.02.007.

[45] V. M. Ferreira *et al.*, "T1 Mapping for the diagnosis of acute myocarditis using CMR: Comparison to T2-Weighted and late gadolinium enhanced imaging," *JACC Cardiovasc. Imaging*, vol. 6, no. 10, pp. 1048–1058, 2013, doi: 10.1016/j.jcmg.2013.03.008.

[46] M. Altaha *et al.*, "Can Quantitative CMR Tissue Characterization Adequately Identify Cardiotoxicity During Chemotherapy?," *JACC Cardiovasc. Imaging*, vol. 13, no. 4, 2020, doi: 10.1016/j.jcmg.2019.10.016.

[47] M. Markl, A. Frydrychowicz, S. Kozerke, M. Hope, and O. Wieben, "4D flow MRI," *J. Magn. Reson. Imaging*, vol. 36, no. 5, pp. 1015–1036, 2012, doi: 10.1002/jmri.23632.

[48] Z. Stankovic, B. D. Allen, J. Garcia, K. B. Jarvis, and M. Markl, "4D PC flow," *Cardiovascular*, vol. 4, no. 2, pp. 173–192, 2014, doi: 10.3978/j.issn.2223-3652.2014.01.02.

[49] F. M. Callaghan and S. M. Grieve, "Translational Physiology: Normal patterns of thoracic aortic wall shear stress measured using four-dimensional flow MRI in a large population," *Am. J. Physiol. - Hear. Circ. Physiol.*, vol. 315, no. 5, pp. H1174–H1181, 2018, doi: 10.1152/ajpheart.00017.2018.

[50] J. N. Osinnski, D. N. Ku, S. Mukundan, F. Loth, and R. I. Pettigrew, "Determination of wall shear stress in the aorta with the use of MR phase velocity mapping," *J. Magn. Reson. Imaging*, vol. 5, no. 6, pp. 640–647, 1995, doi: 10.1002/jmri.1880050605.

[51] A. Ricco *et al.*, "Cardiac MRI utilizing late gadolinium enhancement (LGE) and T1 mapping in the detection of radiation induced heart disease," *Cardio-Oncology*, vol. 6, no. 1, pp. 1–9, 2020, doi: 10.1186/s40959-020-00061-z.

[52] R. Umezawa *et al.*, "Dose-Dependent Radiation-Induced Myocardial Damage in Esophageal Cancer Treated With Chemoradiotherapy: A Prospective Cardiac Magnetic Resonance Imaging Study," *Adv. Radiat. Oncol.*, vol. 5, no. 6, pp. 1170–1178, 2020, doi:

10.1016/j.adro.2020.07.012.

[53] P. B. Johnson, K. R. Padgett, K. L. Chen, and N. Dogan, "Evaluation of the tool 'Reg Refine' for user-guided deformable image registration," *J. Appl. Clin. Med. Phys.*, vol. 17, no. 3, pp. 158–170, 2016, doi: 10.1120/jacmp.v17i3.6025.

[54] J. Piper, A. Nelson, and J. Harper, "Deformable Image Registration in MIM Maestro ® Evaluation and Description," *MIM Softw. White Pap.*, pp. 1–5, 2013.

[55] A. Omidi, E. Weiss, J. S. Wilson, and M. Rosu-Bubulac, "Quantitative assessment of intra- and inter-modality deformable image registration of the heart, left ventricle, and thoracic aorta on longitudinal 4D-CT and MR images," *J. Appl. Clin. Med. Phys.*, no. July, pp. 1–10, 2021, doi: 10.1002/acm2.13500.

[56] Y. Tong *et al.*, "Quantification of variation in dose-volume parameters for the heart, pericardium and left ventricular myocardium during thoracic tumor radiotherapy," *J. Radiat. Res.*, vol. 59, no. 4, pp. 462–468, 2018, doi: 10.1093/jrr/rry026.

[57] R. Yan *et al.*, "Dosimetric impact from cardiac motion to heart substructures in thoracic cancer patients treated with a magnetic resonance guided radiotherapy system," *Phys. Imaging Radiat. Oncol.*, vol. 17, no. December 2020, pp. 8–12, 2021, doi: 10.1016/j.phro.2020.11.005.

[58] H. Stranzl and B. Zurl, "Postoperative irradiation of left-sided breast cancer patients and cardiac toxicity: Does deep inspiration breath-hold (DIBH) technique protect the heart?," *Strahlentherapie und Onkol.*, vol. 184, no. 7, pp. 354–358, 2008, doi: 10.1007/s00066-008-1852-0.

[59] R. Avram *et al.*, "Real-world heart rate norms in the Health eHeart study," *npj Digit. Med.*, vol. 2, no. 1, 2019, doi: 10.1038/s41746-019-0134-9.

[60] P. C. Loughlin, F. Sebat, and J. G. Kellett, "Respiratory Rate: The Forgotten Vital Sign—Make It Count!," *Jt. Comm. J. Qual. Patient Saf.*, vol. 44, no. 8, pp. 494–499, 2018, doi: 10.1016/j.jcjq.2018.04.014.

[61] H. Bahig *et al.*, "In a Heartbeat: An Assessment of Dynamic Dose Variation to Cardiac Structures Using Dual Source Computed Tomography," *Int. J. Radiat. Oncol. Biol. Phys.*, vol. 102, no. 4, pp. 950–959, 2018, doi: 10.1016/j.ijrobp.2018.01.049.

[62] K. M. Menezes, H. Wang, M. Hada, and P. B. Saganti, "Radiation Matters of the Heart: A Mini Review," *Front. Cardiovasc. Med.*, vol. 5, no. July, pp. 1–10, 2018, doi: 10.3389/fcvm.2018.00083.

[63] M. Feng *et al.*, "Development and validation of a heart atlas to study cardiac exposure to radiation following treatment for breast cancer," *Int. J. Radiat. Oncol. Biol. Phys.*, vol. 79, no. 1, pp. 10–18, 2011, doi: 10.1016/j.ijrobp.2009.10.058.

[64] J. Schulz-Menger *et al.*, "Standardized image interpretation and post processing in cardiovascular magnetic resonance: Society for Cardiovascular Magnetic Resonance (SCMR) Board of Trustees Task Force on Standardized Post Processing," *J. Cardiovasc. Magn. Reson.*, vol. 15, no. 1, p. 1, 2013, doi: 10.1186/1532-429X-15-35.

[65] S. Grover, D. P. Leong, and J. B. Selvanayagam, "Evaluation of left ventricular function using cardiac magnetic resonance imaging," *J. Nucl. Cardiol.*, vol. 18, no. 2, pp. 351–365, 2011, doi: 10.1007/s12350-010-9334-z.

[66] C. Bergom *et al.*, "A Pilot Study of Cardiac MRI in Breast Cancer Survivors After Cardiotoxic Chemotherapy and Three-Dimensional Conformal Radiotherapy," *Front. Oncol.*, vol. 10, no. October, pp. 1–10, 2020, doi: 10.3389/fonc.2020.506739.

[67] S. Tang *et al.*, "Myocardial Segmental Strain Changes Detected with Cardiac MRI following Tangential Breast Radiation," vol. 59, pp. 38–76, 2018.

[68] N. Van Der Velde *et al.*, "Cardiovascular magnetic resonance for early detection of late cardiotoxicity in asymptomatic survivors of hodgkin and non-hodgkin lymphoma," *Eur. Hear. J. - Cardiovasc. Imaging*, vol. 22, no. Supplement_2, pp. 187–188, 2021, doi: 10.1093/ehjci/jeab090.130.

[69] Paaladinesh Thavendiranathan and K. Negishi, "Detection of subclinical heart failure," in *ASE's Comprehensive Strain Imaging*, 2022.

[70] D. R. Messroghli, A. Radjenovic, S. Kozerke, D. M. Higgins, M. U. Sivananthan, and J. P. Ridgway, "Modified look-locker inversion recovery (MOLLI) for high-resolution T 1 mapping of the heart," *Magn. Reson. Med.*, vol. 52, no. 1, pp. 141–146, 2004, doi: 10.1002/mrm.20110.

[71] X. Zhong *et al.*, "Imaging Three-Dimensional Myocardial Mechanics Using Navigator-gated Volumetric Spiral Cine DENSE MRI," *Magn Reson Med*, vol. 64, no. 4, pp. 1089–1097, 2011, doi: 10.1002/mrm.22503.Imaging.

[72] L. E. Hudsmith *et al.*, "Determination of Cardiac Volumes and Mass With FLASH and SSFP Cine Sequences at 1 . 5 vs . 3 Tesla : A Validation Study," vol. 318, pp. 312–318, 2006, doi: 10.1002/jmri.20638.

[73] A. Qasem and A. Avolio, "Determination of aortic pulse wave velocity from waveform decomposition of the central aortic pressure pulse," *Hypertension*, vol. 51, no. 2, pp. 188–195, 2008, doi: 10.1161/HYPERTENSIONAHA.107.092676.

[74] E. Bollache *et al.*, "Aortic-valve mediated wall shear stress is heterogeneous and predicts regional aortic elastic fiber thinning in bicuspid aortic valve-associated aortopathy," *J Thorac Cardiovasc Surg*, vol. 156, no. 6, pp. 2112–2120, 2019, doi: 10.1016/j.jtcvs.2018.05.095.Aortic-valve.

6 Supplement
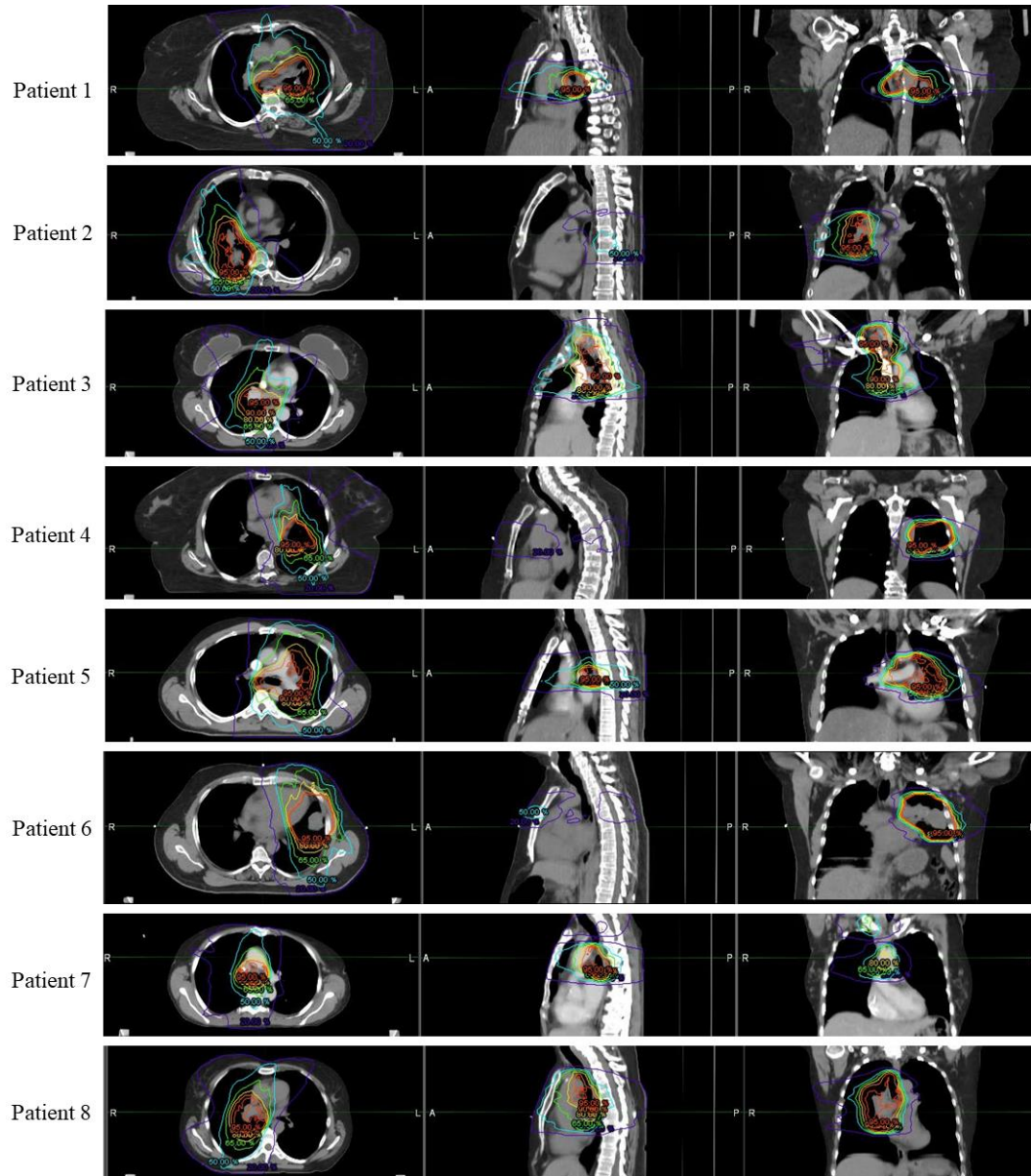
Figure6.1. Dosimetry map for each patient.

Table 6.1. Summary of global measurements at baseline (t1), 3-months follow up (t2), and 6-months follow up (t3) in addition to absolute and relative changes between 3-months follow up and baseline (t2-t1) and (t2-t1 (relative)) and 6-months follow up and baseline (t3-t1) and (t3-t1 (relative)).

Global Metrics	t1		t2		t3		t2-t1		t2-t1 (relative)		t3-t1		t3-t1 (relative)	
	Value	SD	Value	SD	Value	SD	Value	SD	Value	SD	Value	SD	Value	SD
LVEF (%)	57.5	6.8	57.1	5.4	58.6	6.6	0.4	4.3	1.4	8.1	-0.3	2.5	-0.4	4.1
T1 (ms)	1268.1	49.6	1275.0	32.9	1297.2	78.1	14.3	35.8	1.2	2.9	7.8	82.3	0.7	6.3
T2 (ms)	43	2.3	44	2.4	44	3.2	1.2	1.2	2.8	2.8	1.3	4.7	3.5	10.6
ECV	0.3	0.0	0.4	0.2	0.3	0.0	0.1	0.2	31.7	57.5	0.0	0.1	1.5	18.4
Radial Strain	30.2	9.3	29.8	6.7	29.7	7.7	0.5	5.3	6.4	20.8	-1.4	4.3	-1.0	12.7
Circumferential Strain	-17.6	3.6	-17.5	2.7	-17.8	3.6	-0.4	2.4	4.6	15.9	0.0	2.0	1.2	11.0
Longitudinal Strain	-15.0	3.4	-15.0	2.2	-14.0	3.54	-0.2	2.5	4.0	16.6	1.7	2.1	-10.0	14.5
Enhanced volume (%)	5.7	3.7	8.6	3.7	10.0	2.7	2.3	3.1	31.7	48.4	5.4	3.7	5668.4	9686.1

Table 6.2. Regional T1 signal values (±SD) based on AHA model at each time point (i.e., baseline (t1), 3-months post-RT (t2), and 6-months post-RT completion (t3)) along with absolute and relative changes between 3-months follow up and baseline (t2-t1) and (t2-t1 (relative)) and 6-months follow up and baseline (t3-t1) and (t3-t1 (relative)).

AHA segment	t1 (ms)		t2 (ms)		t3 (ms)		t2-t1 (ms)		t2-t1 (relative)		t3-t1 (ms)		t3-t1 (relative)	
	Value	SD	Value	SD	Value	SD	Value	SD	Value	SD	Value	SD	Value	SD
1	1229.1	45.6	1271.8	39.2	1295.4	98.5	50.4	68.3	4.3	5.9	45.0	120.0	3.8	9.8
2	1290.1	62.2	1312.4	49.3	1336.5	82.1	26.7	30.6	2.2	2.5	16.6	75.3	1.3	5.6
3	1286.3	47.2	1285.5	37.3	1289.0	42.2	8.5	27.0	0.7	2.2	-12.0	50.6	-0.8	3.8
4	1280.6	62.2	1290.2	40.8	1285.8	60.1	19.0	48.5	1.6	4.1	-7.4	51.7	-0.5	3.9
5	1250.7	44.2	1241.5	64.9	1268.5	68.9	-6.6	32.5	-0.6	2.6	6.5	44.2	0.5	3.4
6	1220.5	55.8	1272.6	66.8	1272.9	74.3	60.4	74.1	5.1	6.4	25.1	71.4	2.0	5.7
7	1233.2	58.2	1252.7	36.2	1280.8	100.9	23.1	65.7	2.1	5.5	23.1	124.2	2.1	10.2
8	1288.0	42.2	1305.7	50.5	1310.0	70.6	20.9	31.3	1.6	2.4	2.4	59.0	0.2	4.4
9	1290.7	37.2	1284.8	31.3	1276.9	49.7	-1.0	21.5	-0.1	1.7	-28.9	53.5	-2.2	4.1
10	1256.2	70.6	1266.1	28.4	1263.0	56.5	20.7	53.4	1.9	4.7	-10.0	64.8	-0.7	4.9
11	1248.9	91.2	1242.2	50.9	1257.2	70.8	5.6	46.1	0.7	4.1	-20.0	77.3	-1.4	6.0
12	1229.6	64.9	1247.6	34.9	1274.9	94.2	31.5	68.7	2.8	5.8	20.4	125.4	1.9	10.3
13	1277.8	72.7	1268.8	70.0	1339.5	121.5	-9.1	67.9	-0.5	5.3	25.2	92.5	1.8	6.9
14	1332.8	46.8	1360.9	119.2	1305.8	73.7	36.2	107.4	2.7	8.0	-36.4	84.0	-2.6	6.1
15	1293.6	58.6	1285.6	52.2	1271.0	57.6	0.3	67.5	0.2	5.1	-25.5	86.2	-1.7	6.5
16	1282.4	106.1	1273.3	51.3	1299.4	79.6	4.4	118.1	1.0	9.0	-33.4	109.7	-2.2	8.0

Table 6.3. Regional ECV values (±SD) based on AHA model at each time point (i.e., baseline (t1), 3-months post-RT (t2), and 6-months post-RT completion (t3)) along with absolute and relative changes between 3-months follow up and baseline (t2-t1) and (t2-t1 (relative)) and 6-months follow up and baseline (t3-t1) and (t3-t1 (relative)).

AHA segment	t1		t2		t3		t2-t1		t2-t1 (relative)		t3-t1		t3-t1 (relative)	
	Value	SD	Value	SD	Value	SD	Value	SD	Value	SD	Value	SD	Value	SD
1	0.31	0.03	0.39	0.13	0.35	0.08	0.07	0.16	28.4	53.2	0.04	0.09	13.0	27.8
2	0.35	0.04	0.43	0.16	0.37	0.06	0.07	0.20	26.1	59.4	0.01	0.09	6.0	26.0
3	0.32	0.02	0.44	0.18	0.31	0.04	0.11	0.19	34.8	60.1	-0.01	0.05	-2.5	15.8
4	0.34	0.03	0.44	0.14	0.32	0.04	0.09	0.18	30.7	53.9	-0.02	0.07	-5.0	18.5
5	0.35	0.03	0.42	0.15	0.32	0.04	0.07	0.18	23.8	52.0	-0.03	0.05	-8.1	14.5
6	0.32	0.03	0.43	0.17	0.34	0.07	0.12	0.21	46.3	71.3	0.02	0.07	7.4	20.3
7	0.32	0.01	0.42	0.16	0.34	0.05	0.09	0.17	31.6	55.4	0.02	0.06	5.9	18.4
8	0.34	0.02	0.45	0.18	0.34	0.04	0.10	0.20	32.1	60.8	0.00	0.06	1.6	18.2
9	0.33	0.01	0.43	0.17	0.32	0.05	0.09	0.18	30.0	56.1	-0.01	0.06	-1.4	18.5
10	0.33	0.02	0.42	0.15	0.30	0.03	0.08	0.17	24.3	49.8	-0.03	0.06	-7.1	16.7
11	0.33	0.02	0.45	0.20	0.30	0.01	0.11	0.21	33.8	61.8	-0.03	0.03	-8.8	9.8
12	0.30	0.01	0.42	0.15	0.32	0.03	0.11	0.16	38.1	53.7	0.02	0.04	6.5	11.8
13	0.34	0.02	0.46	0.18	0.33	0.04	0.10	0.18	28.4	50.7	-0.01	0.05	-3.0	13.6
14	0.34	0.01	0.45	0.19	0.33	0.04	0.10	0.20	30.3	56.6	-0.01	0.06	-3.0	16.0
15	0.34	0.06	0.46	0.17	0.31	0.06	0.08	0.22	30.0	62.1	-0.03	0.11	-4.4	30.4
16	0.33	0.04	0.47	0.19	0.32	0.04	0.11	0.21	36.4	61.9	-0.01	0.07	0.2	21.6

Table 6.4. Regional T2 signal values (±SD) based on AHA model at each time point (i.e., baseline (t1), 3-months post-RT (t2), and 6-months post-RT completion) (t3) along with absolute and relative changes between 3-months follow up and baseline (t2-t1) and (t2-t1 (relative)) and 6-months follow up and baseline (t3-t1) and (t3-t1 (relative)).

AHA segment	t1		t2		t3		t2-t1		t2-t1 (relative)		t3-t1		t3-t1 (relative)	
	Value	SD	Value	SD	Value	SD	Value	SD	Value	SD	Value	SD	Value	SD
1	41.5	2.1	42.9	1.3	46.1	5.3	1.7	2.0	4.4	5.0	4.7	6.1	11.8	14.8
2	42.8	2.3	43.1	2.0	44.1	2.7	0.6	1.8	1.4	4.4	1.0	3.7	2.7	8.8
3	42.1	1.8	42.7	2.3	42.6	2.5	1.0	1.6	2.5	3.8	0.4	3.5	1.3	8.1
4	42.1	2.7	43.8	2.7	43.3	2.8	2.0	1.5	4.9	3.7	1.6	4.3	4.4	10.5
5	42.4	2.6	43.5	3.4	43.8	2.9	1.6	2.0	3.8	4.7	1.7	4.8	4.8	11.7
6	41.2	2.3	42.9	2.0	43.8	4.9	2.0	2.4	5.0	6.0	3.1	5.9	8.2	14.6
7	42.5	2.4	43.8	2.3	44.2	4.6	1.8	1.5	4.2	3.6	1.7	5.6	4.4	13.0
8	43.3	3.0	43.3	2.2	44.2	2.6	0.5	1.6	1.4	3.7	0.7	4.1	2.1	9.2
9	42.6	2.4	42.7	2.0	43.2	2.3	0.6	0.9	1.5	2.1	0.7	3.8	2.1	8.8
10	42.5	2.3	43.2	2.0	43.0	2.6	0.8	2.0	2.0	4.7	1.0	3.0	2.5	7.5
11	43.3	2.5	44.0	3.3	44.7	3.7	1.0	2.2	2.2	4.9	1.8	4.9	4.8	11.5
12	42.1	2.9	43.8	2.1	43.9	5.6	2.5	2.9	6.3	7.7	2.4	7.6	6.7	18.1
13	46.9	3.1	45.8	3.5	45.7	4.4	-0.9	2.6	-1.9	5.3	-0.9	5.0	-1.6	10.7
14	44.8	4.6	45.4	4.0	43.5	2.3	1.3	1.5	3.1	3.3	-1.5	6.1	-2.0	12.6
15	45.3	6.0	44.1	3.4	43.8	3.3	-0.8	3.7	-0.9	7.4	0.4	4.8	1.6	10.6
16	45.4	2.6	47.4	7.4	47.2	5.6	2.6	8.0	6.2	17.8	2.1	7.4	5.4	16.3

Table 6.5. Regional radial strain values (±SD) based on AHA model at each time point (i.e., baseline (t1), 3-months post-RT (t2), and 6-months post-RT completion) (t3) along with absolute and relative changes between 3-months follow up and baseline (t2-t1) and (t2-t1 (relative)) and 6-months follow up and baseline (t3-t1) and (t3-t1 (relative)).

AHA segment	t1		t2		t3		t2-t1		t2-t1 (relative)		t3-t1		t3-t1 (relative)	
	Value	SD	Value	SD	Value	SD	Value	SD	Value	SD	Value	SD	Value	SD
1	32.7	14.8	28.6	7.9	25.8	8.5	-3.3	17.5	14.9	60.2	-11.2	7.9	-25.5	17.6
2	20.8	10.4	13.5	5.4	18.3	6.5	-4.5	4.9	-23.0	20.8	-3.7	9.3	-1.2	42.4
3	21.0	8.9	19.3	9.3	20.2	7.2	-1.9	3.9	-8.5	13.1	-1.4	8.2	6.6	37.6
4	30.3	10.5	24.9	7.7	32.6	23.3	-5.2	7.2	-12.5	23.8	2.1	18.5	1.2	54.8
5	33.3	15.1	36.0	7.3	37.3	16.6	3.1	12.6	46.3	87.2	5.3	14.5	36.7	55.4
6	39.1	18.1	44.0	10.2	47.5	17.7	4.9	21.3	33.7	58.1	8.4	21.4	37.5	55.6
7	36.7	11.8	37.3	18.2	35.7	28.3	0.6	9.9	1.0	24.2	-3.1	23.3	-8.7	50.0
8	34.5	11.7	39.0	19.0	39.3	15.4	5.0	12.1	14.8	33.1	2.6	11.9	12.0	37.0
9	30.5	10.6	29.8	9.9	25.3	2.6	1.2	6.4	9.6	29.7	-7.2	10.5	-9.5	37.1
10	23.9	9.5	20.5	6.0	20.7	4.7	-1.7	7.0	4.5	40.1	-4.0	10.1	3.6	61.0
11	30.9	11.5	32.4	7.9	29.8	8.7	2.5	11.4	29.3	66.9	-0.4	8.2	8.2	30.2
12	28.7	13.9	26.4	9.4	19.7	7.4	-1.8	14.1	3.7	41.2	-13.7	21.7	-32.8	32.1
13	46.9	15.0	55.6	20.6	41.4	11.5	9.9	14.1	26.0	30.4	-7.9	11.9	-9.1	33.4
14	48.7	14.4	54.2	19.7	43.2	9.9	8.2	11.2	19.0	24.8	-8.0	12.5	-8.7	32.1
15	50.0	21.2	53.9	15.2	35.6	10.0	5.9	15.8	20.9	30.9	-16.1	28.7	-17.5	34.4
16	49.1	21.0	48.4	16.9	30.7	13.3	3.7	16.1	18.7	53.2	-20.7	27.6	-27.6	38.5

Table 6.6. Regional circumferential strain values (±SD) based on AHA model at each time point (i.e., baseline (t1), 3-months post-RT (t2), and 6-months post-RT completion) (t3) along with absolute and relative changes between 3-months follow up and baseline (t2-t1) and (t2-t1 (relative)) and 6-months follow up and baseline (t3-t1) and (t3-t1 (relative)).

AHA segment	t1		t2		t3		t2-t1		t2-t1 (relative)		t3-t1		t3-t1 (relative)	
	Value	SD	Value	SD	Value	SD	Value	SD	Value	SD	Value	SD	Value	SD
1	-18.1	5.3	-17.2	3.0	-16.9	4.9	0.5	6.4	7.2	36.4	2.8	3.0	-13.4	13.8
2	-13.4	4.7	-7.5	6.6	-13.4	4.4	3.9	4.4	-41.4	62.6	0.2	3.7	5.1	31.0
3	-13.8	4.3	-5.3	13.3	-13.2	2.8	7.7	10.0	-71.0	96.5	0.6	3.7	5.2	31.8
4	-17.8	4.2	-15.7	3.9	-15.9	5.9	2.1	3.1	-9.6	18.0	1.9	3.6	-11.5	24.0
5	-17.0	9.6	-20.0	2.8	-19.9	5.6	-3.7	8.2	-45.0	129.6	-4.0	7.5	-40.6	113.3
6	-20.5	4.6	-22.3	3.5	-23.1	4.7	-2.1	5.6	15.9	30.4	-2.9	5.2	18.5	26.8
7	-20.3	4.1	-20.3	5.4	-17.2	5.2	0.3	2.6	-1.0	14.2	3.6	4.7	-15.3	23.6
8	-19.4	3.7	-20.5	5.5	-20.8	4.1	-1.2	3.4	7.2	18.8	-0.6	3.4	5.2	20.4
9	-18.0	4.2	-18.1	3.6	-17.2	2.0	-0.5	2.9	6.1	20.9	1.5	4.0	-2.4	24.4
10	-15.1	4.4	-13.9	3.0	-14.9	2.5	0.5	3.7	3.4	29.0	0.5	4.1	6.3	40.2
11	-17.9	4.6	-18.6	3.3	-19.1	3.6	-1.4	5.1	18.4	44.2	-1.5	1.5	12.4	16.3
12	-17.0	4.6	-13.4	9.3	-15.0	5.2	2.3	7.9	-16.7	64.2	2.5	1.0	-15.5	9.1
13	-22.6	4.2	-24.6	3.8	-22.6	4.5	-2.7	3.4	14.4	17.1	0.4	3.2	0.0	17.2
14	-23.1	3.8	-24.8	3.9	-22.5	2.8	-2.0	2.2	9.7	11.9	1.1	3.5	-2.5	17.1
15	-23.4	4.6	-25.0	3.9	-22.3	3.7	-2.0	3.3	10.7	14.7	1.4	2.9	-4.3	12.7
16	-23.1	5.1	-22.5	4.9	-21.3	5.2	-1.1	4.8	7.8	27.0	2.3	3.9	-8.8	17.5

Table 6.7. Regional longitudinal strain values (±SD) based on AHA model at each time point (i.e., baseline (t1), 3-months post-RT (t2), and 6-months post-RT completion) (t3) along with absolute and relative changes between 3-months follow up and baseline (t2-t1) and (t2-t1 (relative)) and 6-months follow up and baseline (t3-t1) and (t3-t1 (relative)).

AHA segment	t1		t2		t3		t2-t1		t2-t1 (relative)		t3-t1		t3-t1 (relative)	
	Value	SD	Value	SD	Value	SD	Value	SD	Value	SD	Value	SD	Value	SD
1	-13.9	9.0	-17.2	3.5	-16.1	3.8	-3.9	12.4	-63.2	205.2	1.8	6.4	-0.3	47.5
2	-14.3	9.1	-9.5	11.3	-11.1	8.6	3.8	16.3	-57.2	93.5	3.0	11.0	-88.6	105.9
3	-14.6	4.2	-14.1	2.7	-4.4	13.5	-1.2	8.8	-6.5	22.9	10.4	11.5	-85.7	111.7
4	-19.5	4.6	-20.1	3.8	-18.5	5.4	-1.6	5.5	13.9	36.5	1.3	4.5	-3.6	28.0
5	-20.9	4.0	-20.6	3.6	-19.5	6.1	0.8	2.5	-2.8	12.2	1.2	3.6	-6.6	19.7
6	-20.8	3.6	-22.5	6.0	-17.6	7.4	1.0	16.3	-16.5	76.5	5.9	11.9	-19.9	65.6
7	-15.6	6.1	-18.4	5.0	-17.2	8.3	-3.2	4.8	34.0	40.3	-0.8	6.3	11.7	48.9
8	-16.1	3.2	-20.0	3.4	-15.6	5.7	-4.5	3.2	31.7	22.0	1.4	6.2	-5.3	32.8
9	-12.0	10.8	-12.9	4.1	-9.5	4.0	-2.4	13.4	-62.4	73.3	3.4	6.9	-50.5	22.8
10	-5.1	9.2	-6.9	6.7	-9.6	3.7	-2.1	3.9	10.8	53.1	-4.8	12.6	-18.2	84.1
11	-10.9	8.1	-10.1	9.9	-10.3	4.0	3.0	9.5	-11.3	116.1	0.4	9.4	-52.3	149.2
12	-20.5	6.4	-20.8	3.9	7.7	13.0	-4.1	14.8	-10.0	57.3	19.2	17.8	-92.7	90.9
13	-17.1	3.6	-17.2	3.6	-16.8	5.0	0.1	2.2	0.8	13.3	0.8	3.7	-4.7	21.4
14	-18.3	3.8	-17.1	4.6	-19.8	3.3	0.6	4.8	1.0	34.9	-0.3	3.2	2.3	16.5
15	-13.1	4.1	-11.3	4.2	-12.3	3.0	0.8	3.2	-6.9	24.2	0.8	5.5	7.5	46.6
16	-8.0	9.0	-2.3	20.3	-8.6	14.9	3.8	14.7	15.3	201.4	-1.8	13.3	-128.2	259.4

Table 6.8. Regional radial strain values (±SD) (from DENSE MRI) based on AHA model at each time point (i.e., baseline (t1), 3-months post-RT (t2), and 6-months post-RT completion) (t3) along with absolute and relative changes between 3-months follow up and baseline (t2-t1) and (t2-t1 (relative)) and 6-months follow up and baseline (t3-t1) and (t3-t1 (relative)).

AHA segment	t1		t2		t3		t2-t1		t2-t1 (relative)		t3-t1		t3-t1 (relative)	
	Value	SD	Value	SD	Value	SD	Value	SD	Value	SD	Value	SD	Value	SD
1	0.16	0.09	0.13	0.11	0.18	0.11	-0.05	0.06	-37.01	29.5	0.02	0.03	6.80	6.80
2	0.14	0.07	0.14	0.13	0.17	0.11	0.01	0.06	-33.9	87.83	0.01	0.05	-6.15	-6.2
3	0.10	0.12	0.22	0.13	0.26	0.03	0.16	0.16	37.74	291.2	0.19	0.18	-20.5	-20.5
4	0.09	0.05	0.19	0.16	0.30	0.1	0.12	0.16	201.2	225.0	0.19	0.1	232.7	232.7
5	0.15	0.10	0.19	0.16	0.36	0.2	0.03	0.2	-118.5	262.01	0.20	0.13	110.8	110.8
6	0.20	0.09	0.21	0.17	0.38	0.26	0.00	0.10	-19.50	89.4	0.13	0.2	28.8	28.7
7	0.10	0.12	0.05	0.12	0.15	0.13	-0.06	0.07	69.1	146.5	-0.02	0.12	-20.6	-20
8	0.11	0.08	0.06	0.07	0.15	0.15	-0.05	0.05	76.82	188.9	0.01	0.10	-25.87	-25.9
9	0.04	0.10	0.15	0.10	0.08	0.15	0.10	0.07	-115.6	157.6	0.07	0.11	30.33	30.3
10	-0.03	0.10	0.07	0.10	0.14	0.09	0.11	0.10	-282.02	370.5	0.14	0.16	-209.3	-209.3
11	0.04	0.07	0.17	0.15	0.18	0.1	0.12	0.2	-141.5	532.3	0.13	0.10	-215.4	-215.4
12	0.09	0.08	0.13	0.11	0.13	0.17	0.03	0.07	12.90	107.8	0.02	0.14	229.1	229.1
13	-0.04	0.04	-0.07	0.06	-0.06	0.08	-0.01	0.06	19.4	75.9	-0.02	0.1	-88.6	-88.6
14	0.02	0.09	0.02	0.08	-0.11	0.04	0.01	0.05	-27.0	128.3	-0.10	0.1	16.79	16.8
15	0.08	0.06	0.01	0.07	-0.04	0.12	-0.07	0.1	-133.8	106.6	-0.14	0.10	-184.30	-184.3
16	0.00	0.06	0.01	0.10	-0.03	0.1	0.03	0.1	-37.01	29.6	-0.06	0.09	-45.26	-45.3

143

Table 6.9. Regional circumferential strain values (±SD) (from DENSE MRI) based on AHA model at each time point (i.e., baseline (t1), 3-months post-RT (t2), and 6-months post-RT completion) (t3) along with absolute and relative changes between 3-months follow up and baseline (t2-t1) and (t2-t1 (relative)) and 6-months follow up and baseline (t3-t1) and (t3-t1 (relative)).

AHA segment	t1		t2		t3		t2-t1		t2-t1 (relative)		t3-t1		t3-t1 (relative)	
	Value	SD	Value	SD	Value	SD	Value	SD	Value	SD	Value	SD	Value	SD
1	-0.14	4.40	-0.17	0.04	-0.16	0.05	-0.02	0.03	17.75	0.04	-0.02	0.01	15.41	5.46
2	-0.14	3.20	-0.16	0.03	-0.16	0.04	-0.02	0.02	14.06	0.03	-0.01	0.01	11.22	8.65
3	-0.17	2.53	-0.16	0.02	-0.19	0.02	0.02	0.04	-8.88	0.02	0.00	0.06	8.55	37.20
4	-0.20	1.57	-0.21	0.04	-0.23	0.01	-0.01	0.03	11.49	0.04	0.00	0.04	1.08	20.22
5	-0.20	-1.13	-0.21	0.02	-0.21	0.02	0.00	0.01	-1.42	0.02	-0.01	0.03	6.80	16.62
6	-0.15	-3.40	-0.22	0.03	-0.19	0.03	-0.04	0.02	31.56	0.03	-0.04	0.03	43.53	46.25
7	-0.16	2.57	-0.18	0.03	-0.15	0.05	-0.01	0.02	5.60	0.03	0.01	0.02	-5.87	12.87
8	-0.14	-0.40	-0.13	0.03	-0.14	0.05	0.00	0.04	8.73	0.03	0.02	0.03	-16.98	19.20
9	-0.15	4.07	-0.14	0.06	-0.17	0.05	0.02	0.03	-13.54	0.06	-0.02	0.04	10.94	29.19
10	-0.21	3.30	-0.22	0.05	-0.24	0.03	-0.01	0.02	4.04	0.05	-0.03	0.03	15.13	16.19
11	-0.19	-1.07	-0.23	0.04	-0.20	0.04	-0.03	0.02	18.05	0.04	-0.02	0.03	10.16	17.65
12	-0.20	2.70	-0.21	0.03	-0.17	0.07	-0.03	0.04	14.94	0.03	0.04	0.09	-14.84	38.02
13	-0.16	0.57	-0.17	0.04	-0.13	0.02	0.00	0.03	-2.81	0.04	0.03	0.04	-17.17	20.39
14	-0.18	2.67	-0.14	0.00	-0.18	0.01	0.04	0.07	-12.43	0.00	0.02	0.07	1.78	31.06
15	-0.23	2.33	-0.25	0.03	-0.23	0.01	-0.02	0.03	7.23	0.03	-0.01	0.01	2.91	2.24
16	-0.21	3.87	-0.21	0.02	-0.18	0.01	0.00	0.04	1.45	0.02	0.03	0.03	-11.18	14.31

Table 6.10. Regional enhanced area values (±SD) based on AHA model at each time point (i.e., baseline (t1), 3-months post-RT (t2), and 6-months post-RT completion) (t3) along with absolute changes between 3-months follow up and baseline (t2-t1) and 6-months follow up and baseline (t3-t1).

AHA segment	t1		t2		t3		t2-t1		t3-t1	
	Value	SD	Value	SD	Value	SD	Value	SD	Value	SD
1	4.0	5.9	13.8	11.1	12.5	7.5	9.1	5.8	11.3	8.0
2	23.3	13.3	37.8	17.4	29.7	9.3	13.6	14.2	10.9	9.4
3	2.1	1.9	21.5	7.1	11.1	2.7	18.9	8.9	8.8	4.3
4	11.5	9.4	31.6	15.2	20.3	20.0	17.2	19.9	10.3	23.2
5	10.9	12.4	28.6	21.0	27.3	22.2	15.1	26.4	18.1	21.5
6	0.5	1.0	9.2	9.4	15.3	13.0	8.6	10.0	14.6	13.5
7	2.9	3.4	4.8	4.8	7.0	7.1	1.2	5.1	4.4	6.9
8	9.7	6.9	11.4	8.1	12.8	8.2	2.6	1.6	5.8	6.0
9	10.8	7.3	4.2	2.7	3.4	4.3	-8.2	5.2	-5.2	8.8
10	5.2	7.3	6.1	5.7	1.9	1.7	-0.4	11.0	-4.6	7.1
11	2.6	3.2	6.8	7.7	3.9	4.4	3.6	9.1	0.6	6.2
12	0.0	0.0	7.6	8.0	5.6	6.4	7.6	8.0	5.6	6.4
13	1.3	1.9	1.6	2.5	0.0	0.0	-0.1	3.2	-1.7	2.0
14	4.7	5.3	0.9	1.5	0.2	0.4	-1.5	1.6	-5.6	5.2
15	0.1	0.2	0.0	0.0	3.2	3.7	0.0	0.0	3.1	3.5
16	1.3	1.8	3.2	3.4	1.7	2.3	1.5	2.0	1.2	1.6